CORA Cork Open Research Archive
Cartlann Taighde Oscailte Chorcaí

Title	Investigation of the high-frequency effects in Mn-Zn ferrites for EMI filter applications
Authors	Kącki, Marcin
Publication date	2022-08-22
Original Citation	Kącki, M. 2022. Investigation of the high-frequency effects in Mn-Zn ferrites for EMI filter applications. PhD Thesis, University College Cork.
Type of publication	Doctoral thesis
Rights	© 2022, Marcin Kącki. - https://creativecommons.org/licenses/by-nc-nd/4.0/
Download date	2026-11-04 21:29:16
Item downloaded from	https://hdl.handle.net/10468/13592

UCC
University College Cork, Ireland
Coláiste na hOllscoile Corcaigh

Ollscoil na hÉireann, Corcaigh

National University of Ireland, Cork



Investigation of the High-Frequency Effects in Mn-Zn Ferrites for EMI Filter Applications

Thesis presented by

Marcin Kącki, M.Sc.

for the degree of

Doctor of Philosophy

Head of School: Prof. Jorge Oliveira

Supervised by Dr. John G. Hayes,

Dr. Marek S. Ryłko and Prof. Charles R. Sullivan

University College Cork

Department of Electrical and Electronic Engineering

2022

DECLARATION

This is to certify that the work I am submitting is my own and has not been submitted for another degree, either at University College Cork or elsewhere. All external references and sources are clearly acknowledged and identified within the contents. I have read and understood the regulations of University College Cork concerning plagiarism and intellectual property.

ABSTRACT

This thesis focuses on the analysis, identification, and experimental investigation of the high-frequency effects encountered within the magnetic core when used in high-frequency, high-power electromagnetic interference (EMI) filters. These applications require cost-optimized, high-performance, and high-power-density magnetic components. As the manufacturers' material specifications usually do not provide sufficient information to optimize the design, this thesis develops new methods to determine the high-frequency properties of Mn-Zn ferrites up to 20 MHz. Complex permeability and permittivity, as well as specific power loss, are typically provided as one value by the manufacturer, regardless of the core shape and size. Therefore, various magnetic materials are characterized for their complex permeability and permittivity. These two parameters are of differentiated physical origins, and so two independent measurement fixtures are developed and built. The impacts of physical size, temperature and force on complex permeability and permittivity are also considered.

The detailed analysis of magnetic flux is introduced based on a 1-D analytical model, a novel shell-based transmission-line model, and finally, based on the FEM and Maxwell 3D eddy-current field solver. These models are used to calculate the complex permeability characteristics for various core sizes made of two materials: 3E10 and 3F36. A complete experimental validation is presented for the calculated values. The analytical methods show a very good correlation with the experimental measurements. The novel shell-based transmission-line model has the best accuracy, and the calculation can be implemented into simulation of a higher-order system or into any other magnetic component design algorithm.

Flux verification methods are developed which use precisely-bored cores to accurately predict flux distribution. The results of the flux propagation, starting from the simple three-hole model up to the advanced four-section model confirm that the magnetic flux distribution is affected by frequency-dependent dynamic effects. Flux distributions was experimentally measured for T50 and T80 cores made of 3E10 and 3F36 material. Results are consistent with the FEM simulations and help in the development of a more accurate analytical model.

A novel laminated-core common mode choke (CMC) is developed and presented in this thesis. The presented CMC core structure divides the conduction path into sub-regions which allowing for the reduction of the high-frequency effects. Laminated cores, made of several Mn-Zn ferrite materials, were tested and special attention is paid to the effect of magnetic material selection, core size and lamination thickness on the core high-frequency performance. Common mode insertion loss characteristic for the novel CMC shows that laminated ferrite structure give rise to significant attenuation improvement.

ACKNOWLEDGMENTS

I wish to express my deep gratitude to all the individuals who have taken their time to help me and have contributed to my work. This thesis would not have been possible without their tremendous support and guidance, for which I am forever thankful.

At the beginning, I would like to thank my superior academic supervisors, Dr. John Hayes and Prof. Charles Sullivan, for their considerable support, guidance, and friendship throughout my academic career. It was a great honour to get to know John and Charles better during all those years spent together. Moreover, I wish to thank Prof. Jean-Luc Schanen, Dr. Kevin McCarthy and Prof. Alan Dobson for reading, evaluating, and examining my thesis.

I wish to give my special thanks to my industry supervisor - Dr. Marek Ryłko for his help, advice, and unyielding friendship. Marek's support has been incredible and very much appreciated, thank you. He created the possibility for me to start the thesis and took part in each and every step, showing great engagement and enthusiasm. The technical and financial support given by SMA Magnetics is also greatly appreciated.

I would also like to say 'thank you' to all the staff of the Research and Development Department at SMA Magnetics. Among other notable names that undoubtedly deserve to be mentioned are: Wiesław Kowalik, Tomasz Mitoński, Dawid Proszak and Miłosz Szarek. Your great support and passionate commitment helped resolve even the most complex problems and undertake tasks that seemed impossible.

I also wish to thank Edward Herbert not only for his assistance but also for giving me a great deal of motivation, and guidance. I will never forget our lengthy discussions as part of the research project carried out with Power Source Manufactures Association. The technical and financial support of PSMA is also greatly appreciated.

I am indebted to all the staff of the School of Engineering for their assistance and support. I particularly wish to thank Danielle Heffernan and Mary O'Leary.

It goes without saying that the support of my family and friends has been ever so important to the success of my work. I would like to thank Natalia, Adam, Justyna and Szymon. It is difficult to mention all the individuals who contributed to my work so please forgive me for not listing all of you.

My sincere gratitude also goes to my parents and my parents-in-law.

And, of course, to Aneta and Filip, for their love, support, patience and for accompanying me on that long yet unforgettable journey. Thank you

LIST OF PUBLICATIONS

Journal papers

1. M. Kacki, M.S. Rylko, J.G. Hayes, C.R. Sullivan, "Measurements Methods for High-frequency Characterizations of Permeability, Permittivity, and Core loss of Mn-Zn Ferrite Cores," *IEEE Transactions on Power Electronics* (Early Access), July 2022.
2. M. Kacki, M.S. Rylko, J.G. Hayes, C.R. Sullivan, "Analysis and Experimental Investigation of High-frequency Magnetic Flux Distribution in Mn-Zn Ferrite Cores," *IEEE Transactions on Power Electronics* (Early Access), August 2022.

Conference papers

1. M. Kacki, M.S. Rylko, J.G. Hayes, C.R. Sullivan, "Magnetic Material Selection for EMI Filters," *IEEE Energy Conversion Congress and Exposition (ECCE),* Cincinnati, OH, 2017.
2. M. Kacki, M.S. Rylko, E. Herbert, J.G. Hayes, C.R. Sullivan, "A Study of Flux Distribution and Impedance in Solid and Laminar Ferrite Cores," *IEEE Applied Power Electronic Conference and Exposition (APEC)*, Anaheim, CA, 2019.
3. M. Kacki, M.S Rylko, J.G. Hayes, C.R. Sullivan, "A Practical Method to Define High Frequency Electrical Properties of MnZn Ferrites," *IEEE Applied Power Electronics Conference and Exposition (APEC)*, New Orleans, LA, 2020.

Patents

1. M. Kacki, M.S. Rylko, "Core assembly having magnetic properties for an electrical device, and throttle comprising such a core assembly," patent application WO20200015962A1.

Technical reports

1. M. Kacki, M.S. Rylko, E. Herbert, "PSMA-SMA Special Project – Phase I, Investigation on Magnetic Flux Propagation in Ferrite Cores", *The Power Source Manufacturers Association Technical Report*, 2018.
2. M. Kacki, M.S. Rylko, E. Herbert, "PSMA-SMA Special Project – Phase II, Investigation on Magnetic Flux Propagation in Ferrite Cores", *The Power Source Manufacturers Association Technical Report*, 2020

TABLE OF CONTENTS

1 Introduction 1

1.1 Overview 2

1.2 Thesis objectives 4

1.3 Thesis Structure 5

1.4 General background 7

1.4.1 Analysis of high-frequency pulse transitions on EMI generation 7

1.4.2 Magnetic materials for EMI filters 10

1.4.3 The magnetic design for inductors and filters 17

1.5 High-frequency effects in the magnetic core 19

1.5.1 Application of Maxwells equations 19

1.5.2 Dimensional resonance and skin depth 21

1.6 Conclusions 26

2 High Frequency Characteristics of Mn-Zn Ferrites 27

2.1 Complex permeability characteristic 28

2.1.1 Complex permeability physical sample size effect 29

2.1.2 Complex permeability temperature effect 36

2.1.3 Complex permeability force effect 40

2.2 Complex permittivity characteristic 43

2.2.1 Complex permittivity test setup 44

2.2.2 Complex permittivity physical sample size effect 46

2.2.3 Data extrapolation at higher frequencies 50

2.2.4 Complex permittivity temperature effect 54

2.2.5 Complex permittivity force effect 55

2.3 Power losses 57

2.3.1 Loss tangent 57

2.3.2 Performance factor 58

2.3.3 Power loss under the rectangular excitation 60

2.4 Conclusions 63

3 Modelling of Magnetic Field Distribution in Mn-Zn Ferrite Cores 65
3.1 Introduction 66
3.2 1-D analytical field distribution model 66
3.2.1 Theory 66
3.2.2 Results 67
3.2.3 Experimental validation 72
3.2.4 Conclusions 75
3.3 Core transmission line model 76
3.3.1 Theory 76
3.3.2 Results 79
3.3.3 Experimental validation 81
3.3.4 Conclusions 83
3.4 Magnetic core FEM modeling 84
3.4.1 Experimental validation 85
3.5 Practical aspects of experimental and analytical approaches 87
3.5.1 Calculation error 89
3.5.2 Calculation time 91
3.6 Conclusions 91
4 Novel Experimental Validation of Flux Distribution in a Ferrite Core 92
4.1 Introduction 93
4.2 Verification of T50 flux distribution – “two shells” core drilling scheme 93
4.2.1 Core preparation 93
4.2.2 Experimental validation 96
4.3 Verification of the flux distribution – “four shells” core drilling scheme 100
4.3.1 Core preparation 100
4.3.2 Experimental validation 102
4.4 Conclusions 105
5 A Novel Laminated Ferrite Core 106
5.1 Finite-Element Analysis 107

5.2 New lamination thickness effect on core performance 109
5.3 Modularity of laminated cores 112
5.4 The effect of magnetic material selection on the lamination 114
5.5 Core size effect on the lamination 116
5.6 Verification of the flux distribution in laminated ferrite core 118
5.7 Single phase EMC filter based on the laminated ferrite core 121
5.8 Conclusions 126
6 Conclusions and Future Work 127
6.1 Chapter Summaries 128
6.1.1 Chapter 1 128
6.1.2 Chapter 2 129
6.1.3 Chapter 3 130
6.1.4 Chapter 4 132
6.1.5 Chapter 5 133
6.2 Future work 134
6.2.1 Complex permeability and permittivity modelling 134
6.2.2 Magnetic core power loss analysis 134
6.2.3 TLM model validation and improvement 134
6.2.4 Study on flux propagation under rectangular waveform 135
References 136
Appendix A – Complex Permeability Characteristic 142
Appendix B – Complex Permittivity Characteristic 143
Appendix C – Core Loss Tester Board 144
Appendix D – EMI Filter PCB Board 146

LIST OF FIGURES

Figure 1. Common mode choke for PV inverter. 3
Figure 2. Trapezoidal waveform parameters. 8
Figure 3. EMI emission spectrum comparison: Si vs. SiC vs. GaN. 9
Figure 4. EMI materials relative permeability vs. saturation flux density. 13
Figure 5. Ferrite electrical properties for all Mn-Zn ferrite family based on the ferrite manufacturer specifications [20]. 14
Figure 6. FEA results of the flux distribution in the T90 core, simulation 1 - ideal: f = 500 kHz, μ_r, = 10 000, ε_r = 1, σ = 0.1 S/m. 16
Figure 7. FEA results of the flux distribution in the T90 core, simulation 2 - permittivity included: f = 500 kHz, μ_r, = 10 000, ε_r = 50 000, σ = 0.1 S/m. 16
Figure 8. FEA results of the flux distribution in the T90 core, simulation 3 – conductivity included: f = 500 kHz, μ_r, = 10 000, ε_r = 10 000, σ = 5 S/m. 16
Figure 9. Common Mode Choke impedance vs. frequency. 18
Figure 10. Visualization of electromagnetic wave propagation in lossy material. 19
Figure 11. Standing wave visualization based on the FEA, forward and backward waves are in phase. 21
Figure 12. Standing wave visualization based on the FEA, forward and backward waves are shifted by 90° 22
Figure 13. Standing wave visualization based on the FEA, forward and backward waves are shifted by 180° 22
Figure 14. Skin effect in electrical conductor carrying current and magnetic core carrying flux 23
Figure 15. Skin depth in ferrite vs. frequency based on experimental data. 24
Figure 16. Electromagnetic half-wavelength in ferrite vs. frequency based on experimental data. 24
Figure 17. Electromagnetic wavelength and skin depth in ferrite 3E10 and 3F36. 25
Figure 18. Equivalence of series inductive circuit. 28
Figure 19. Electromagnetic wavelength and skin depth in 3C95 ferrite. 30
Figure 20. 3C95 ferrite real permeability vs. frequency. 31
Figure 21. 3C95 ferrite imaginary permeability vs. frequency. 32
Figure 22. T6 and T2 cores to test complex permeability characteristic. 32
Figure 23. 3C95 ferrite complex permeability vs. frequency. 33
Figure 24. Short-ended coaxial line to measure the permeability characteristic. 34
Figure 25. 3F36 ferrite complex permeability vs. frequency. 34
Figure 26. 3E65 ferrite complex permeability vs. frequency 35

Figure 27. 3E10 ferrite complex permeability vs. frequency..... 35
Figure 28. 3C95 ferrite real permeability vs. frequency and temperature. 36
Figure 29. 3C95 ferrite imaginary permeability vs. frequency and temperature. 37
Figure 30. 3F36 ferrite complex permeability vs. frequency and temperature. 38
Figure 31. 3E65 ferrite complex permeability vs. frequency and temperature. 38
Figure 32. 3E10 ferrite complex permeability vs. frequency and temperature. 39
Figure 33. Measurement setup for testing impact of mechanical stress on magnetic permeability. 40
Figure 34. MnZn ferrite permeability change vs. mechanical pressure based on the experimental data..... 41
Figure 35. 3F36 ferrite complex permeability vs. mechanical pressure. 41
Figure 36. 3E65 ferrite complex permeability vs. mechanical pressure. 42
Figure 37. 3E10 ferrite complex permeability vs. mechanical pressure. 42
Figure 38. Equivalence of parallel capacitive circuit [30]. 43
Figure 39. Summary of measurements techniques for material dielectric properties. 44
Figure 40. Measurement fixture to define ferrite permittivity characteristic. 45
Figure 41. Electrodes and tested ferrite samples..... 45
Figure 42. Calculated half wavelength in 3C95 ferrite. 48
Figure 43. 3C95 ferrite real permittivity vs. frequency. 49
Figure 44. 3C95 ferrite real permittivity vs. frequency. 49
Figure 45. Equivalent electrical circuit of a MnZn ferrite based on constant phase element [39]. 51
Figure 46. 3C95 ferrite real permittivity vs. frequency based on the CPE. 52
Figure 47. 3C95 ferrite imaginary permittivity vs. frequency based on the CPE model. 52
Figure 48. Mn-Zn ferrite real permittivity vs. frequency based on the experimental data. ... 53
Figure 49. Mn-Zn ferrite imaginary permittivity vs. frequency based on the experimental data. 53
Figure 50. 3C95 ferrite complex permittivity vs. frequency and temperature. 54
Figure 51. 3F36 ferrite complex permittivity vs. frequency and temperature. 54
Figure 52. 3E10 ferrite complex permittivity vs. frequency and temperature. 55
Figure 53. 3C95 ferrite complex permittivity vs. frequency and tension. 56
Figure 54. 3F36 ferrite complex permittivity vs. frequency and tension. 56
Figure 55. 3E10 ferrite complex permittivity vs. frequency and tension. 57
Figure 56. The magnetic loss tangent vs. frequency for 3C95 material based on experimental data. 58
Figure 57. Core power loss measurement setup with sinusoidal excitation. 59
Figure 58. The performance factor vs. frequency for 3C95 material. 59

Figure 59. Schematic and photo of the core loss test setup. 61
Figure 60. Waveforms used by the Matlab program to calculate core losses at each operating point [49]. 62
Figure 61. Herbert curve, power loss density vs. frequency for 3C95 material..... 63
Figure 62. Ferrite infinite plate for analytical calculation of the flux distribution in the core. 67
Figure 63. Calculated real field component within 15 mm ferrite plate of 3F36 material..... 68
Figure 64. Calculated imaginary field component within 15 mm ferrite plate of 3F36 material. 68
Figure 65. Calculated real field component within ferrite plate for various thicknesses of 3F36 material. 69
Figure 66. Calculated imaginary field component within ferrite plate for various thicknesses of 3F36 material. 69
Figure 67. Calculated real field component within 10 mm ferrite plate of 3E10 material. ... 70
Figure 68. Calculated imaginary field component within 10 mm ferrite plate of 3E10 material. 70
Figure 69. Calculated real field component within ferrite plate for various thicknesses of 3E10 material..... 71
Figure 70. Calculated imaginary field component within ferrite plate for various thicknesses of 3E10 material. 71
Figure 71. 1-D model calculated and measured normalized real permeability vs. frequency for 3F36 ferrite cores. 73
Figure 72. 1-D model calculated and measured normalized imaginary permeability vs. frequency for 3F36 ferrite cores. 73
Figure 73. 1-D model calculated and measured normalized real permeability vs. frequency for 3E10 ferrite cores. 74
Figure 74. 1-D model calculated and measured normalized imaginary permeability vs. frequency for 3E10 ferrite cores. 74
Figure 75. Magnetic core conceptually divided into five concentric shells. 76
Figure 76. Schematic of the core transmission line model. 77
Figure 77. Calculated normalized permeability vs. frequency for T50 3F36 ferrite core for variable shell number. 78
Figure 78. Average relative error vs. number of shells for 3F36 T50 ferrite core. 78
Figure 79. Calculated normalized real permeability for a T50 core of 3F36 material..... 79
Figure 80. Calculated normalized imaginary permeability for a T50 core of 3F36 material. 79
Figure 81. Calculated normalized real permeability for a T50 core of 3E10 material..... 80
Figure 82. Calculated normalized imaginary permeability for a T50 core of 3E10 material. 81

Figure 83. TLM calculated and measured normalized real permeability vs. frequency for 3F36 ferrite cores. 82
Figure 84. TLM calculated and measured normalized imaginary permeability vs. frequency for 3F36 ferrite cores. 82
Figure 85. TLM calculated and measured normalized real permeability vs. frequency for 3E10 ferrite cores. 83
Figure 86. TLM calculated and measured normalized imaginary permeability vs. frequency for 3E10 ferrite cores. 83
Figure 87. FEA results of RMS magnetic flux distribution in the T50, 3F36 ferrite core at 1.7 MHz. 84
Figure 88. FEA results of RMS magnetic flux distribution in the T50, 3E10 ferrite core at 0.3 MHz. 84
Figure 89. FEM simulated and measured normalized real permeability vs. frequency for 3F36 ferrite cores. 85
Figure 90. FEM simulated and measured normalized imaginary permeability vs. frequency for 3F36 ferrite cores. 86
Figure 91. FEM simulated and measured normalized real permeability vs. frequency for 3E10 ferrite cores. 86
Figure 92. FEM simulated and measured normalized imaginary permeability vs. frequency for 3E10 ferrite cores. 87
Figure 93. Calculated and measured normalized real permeability vs. frequency for 3F36 T50 ferrite core. 88
Figure 94. Calculated and measured normalized real permeability vs. frequency for 3F36 T50 ferrite core including tolerance analysis. 89
Figure 95. T50 drilled core dimensions. 94
Figure 96. T50 core drilling scheme with section arrangements . 94
Figure 97. Measurements setup for magnetic flux distribution test. 95
Figure 98. Winding configuration to measure voltage V_1 and V_2 . 95
Figure 99. Magnetic flux density ratio in section A and B for 3E10 T50 core. 97
Figure 100. Phase in section A and B for 3E10 T50 core. 97
Figure 101. Measured voltages for T50 3E10 core at (a) 100 kHz and (b) 500 kHz. 98
Figure 102. Measured voltages for T50 3E10 core at (a) 1 MHz and (b) 1.5 MHz. 98
Figure 103. Magnetic flux density ratio in section A and B for 3F36 T50 core. 99
Figure 104. Phase in section A and B for 3F36 T50 core. 99
Figure 105. Measured voltages for T50 3F36 core at (a) 100 kHz and (b) 500 kHz. 100
Figure 106. Measured voltages for T50 3F36 core at (a) 1 MHz and (b) 1.5 MHz. 100
Figure 107. Tested core with drilled three sets of holes. 101

Figure 108. Tested core with sense winding. 102
Figure 109. Section arrangement in tested cores based on the 4 shells drilling shame..... 102
Figure 110. Magnetic flux density ratio in the each section for the 3F36 T50 core at 1 MHz. 103
Figure 111. Magnetic flux density ratio in the each section for the 3E10 T50 core. 103
Figure 112. Magnetic flux density ratio in the each section for the 3E10 T80 core. 104
Figure 113. Magnetic flux density ratio in the each section for the 3F36 T50 core. 104
Figure 114. Magnetic flux density ratio in the each section for the 3F36 T80 core. 105
Figure 115. Ferrite eddy current reduction by lamination. 107
Figure 116. FEA results of the flux distribution in the solid and laminated ferrite ring core. 108
Figure 117. FEA modeling of the field distribution in solid and laminated ferrite ring cores. 108
Figure 118. T50 cores to test lamination thickness impact on core performance. 109
Figure 119. 3F36 ferrite real permeability vs. frequency for various lamination thicknesses. 110
Figure 120. 3F36 ferrite imaginary permeability vs. frequency for various lamination thicknesses. 110
Figure 121. 3E10 ferrite real permeability vs. frequency for various lamination thicknesses. 111
Figure 122. 3E10 ferrite imaginary permeability vs. frequency for various lamination thicknesses. 111
Figure 123. Cores used to test the effect of core modularity. 112
Figure 124. 3F36 ferrite inductance vs. frequency for various number of laminations. 113
Figure 125. 3F36 ferrite impedance vs. frequency for various number of laminations. 113
Figure 126. 3E10 ferrite inductance vs. frequency for various number of laminations. 114
Figure 127. 3E10 ferrite impedance vs. frequency for various number of laminations. 114
Figure 128. Real permeability vs. frequency for various Mn-Zn materials – comparison of laminated and solid cores 115
Figure 129. Imaginary permeability vs. frequency for various Mn-Zn materials – comparison of laminated and solid cores. 115
Figure 130. Cores used to test the core size effect on lamination performance. 116
Figure 131. 3F36 ferrite real permeability vs. frequency for various core sizes. 117
Figure 132. 3F36 ferrite imaginary permeability vs. frequency for various core sizes. 117
Figure 133. 3E10 ferrite real permeability vs. frequency for various core sizes. 118
Figure 134. 3E10 ferrite imaginary permeability vs. frequency for various core sizes. 118
Figure 135. Magnetic flux density ratio in the each section for 3E10 T50 solid core. 119

Figure 136. Magnetic flux density ratio in the each section for 3E10 T50 laminated core. 119
Figure 137. Magnetic flux density ratio in the each section for 3F36 T50 solid core. 120
Figure 138. Magnetic flux density ratio in the each section for 3F36 T50 laminated core. 120
Figure 139. Common-mode choke built to test laminated ferrite cores. 121
Figure 140. Tested common-mode chokes inductance vs. frequency..... 123
Figure 141. Tested common-mode chokes impedance vs. frequency..... 123
Figure 142. Schematic of the two stage EMI filter. 124
Figure 143. Complete EMI filters for common-mode choke test. 125
Figure 144. EMI filters common-mode insertion loss vs. frequency. 125

LIST OF TABLES

TABLE 1. TRAPEZOIDAL SIGNAL PARAMETERS. 9
TABLE 2. MAGNETIC MATERIAL PROPERTIES. 12
TABLE 3. CORE PARAMETERS FOR COMPLEX PERMEABILITY MEASUREMENTS..... 29
TABLE 4. CORE PARAMETERS FOR COMPLEX PERMITTIVITY MEASUREMENTS..... 47
TABLE 5. 3C95 CPE EQUIVALENT PARAMETERS TO MODEL REAL AND IMAGINARY PERMITTIVITY..... 52
TABLE 6. CORE PARAMETERS USED FOR ANALYTICAL CALCULATION VERIFICATION..... 72
TABLE 7. MODEL ERRORS..... 90
TABLE 8. CPU TIME FOR CALCULATION T50, 3F36 FERRITE CORE REAL PERMEABILITY CHARACTERISTIC..... 91
TABLE 9. CORE PARAMETERS USED FOR FLUX DISTRIBUTION VERIFICATION – TWO SHELLS 93
TABLE 10. CORE PARAMETERS USED FOR FLUX VERIFICATION 101
TABLE 11. COMMON MODE CHOKE PARAMETERS. 122
TABLE 12. EMI FILTER COMPONENT SPECIFICATION. 124

1 INTRODUCTION

This chapter presents an overview of the main area of the study, discussed in this dissertation, and outlines the thesis structure. The research work is focused on the analysis, identification, and experimental verification of the high-frequency effects within the magnetic cores used in high-frequency, high-power electromagnetic interference (EMI) filters. A significant part of this work is devoted to defining the electrical properties of magnetic materials, since such information is generally missing from the manufacturer`s datasheets. This thesis investigates the flux distribution of magnetics used in EMI filters of photovoltaic inverters. The next chapter further considers the impact of the wide-bandgap semiconductors on the EMI spectrum, an additional challenge for the design of EMI filters. A reduction of EMI along with the design of magnetic components has become one of the major challenges in designing a new generation of power electronic converters e.g. for renewable energy systems. The general overview of the magnetic materials designated for EMI filters is presented with an emphasis on the critical magnetic material characteristics needed for accurate design and modeling. Towards the end of the chapter, the author presents an analysis of the high-frequency effects visible in the magnetic cores.

Section 1.1 presents the thesis overview. Section 1.2 and 1.3 present the thesis objectives and structure, respectively. Section 1.4 discusses the general background, while Section 1.5 discusses high-frequency effects. A brief conclusion is presented in Section 1.6.

1.1 Overview

The International Energy Agency reported that we are now consuming more than twice the amount of electricity we had done 40 years ago. Projections suggest that if we do not make any changes, we will be using about 50 percent more electric energy in 2050 [1]. Therefore, the negative impact on our global environment, climate and economy related to electricity generation, transmission and transformation must be minimized. Renewable energy systems, such as photovoltaic (PV), provide significant environmental benefits in comparison to conventional energy sources. PV systems are regarded as clean and sustainable sources of electric energy [2]. Despite this, PV inverter manufacturers constantly strive to improve the generation of electric energy and its transformation. The continuous drive for the improvement of electrical energy conversion focuses on the efficiency improvements and combines with higher switching frequencies to reduce size and anticipated cost. This leads to new solutions and is fostering an interest in the new wide-bandgap (WBG) silicon-carbide (SiC) and gallium-nitride (GaN) semiconductors with superior switching performance in comparison to the traditional silicon (Si) based power semiconductors [4]-[6]. The benefits of using such semiconductors, i.e. higher switching frequencies, higher rate of voltage (*dv/dt*), and current (*di/dt*) transients, and higher power densities create a continuous frontier for EMI filtering and magnetic component design [7]. Regulations and industry standards on electromagnetic compatibility (EMC) stipulate limitations on radiated and conducted EMI noise generated by each photovoltaic inverter connected to the grid. In order to meet these emission standards, depending on the frequency range many solutions are available, such as soft switching [8], snubber circuits [9], PCB layout guidelines [10]-[13], and, of course, dedicated EMI filters. Utilizing the aforementioned EMI filters is one of the basic and the most common approaches to reducing EMI noise levels. EMI filters with the attenuation characteristics matched to the EMI source suppress both common-mode (CM) and differential mode (DM) noise. Therefore, the implementation of good filter design in many cases determines the project success and minimizes post-processing solutions, including the addition of mitigating components as well as testing time and cost. The EMI filter is a combination of passive components (*R, L, C)*. The biggest and the most complex part of the EMI filter is the magnetic component, in this case the common-mode choke (CMC). An example of the CMC used in the EMI filter of a 60 kW photovoltaic inverter is shown in Figure 1 [14]. It provides the required common-mode, and often the differential-mode impedances over the frequency range from 150 kHz up to 30 MHz, and it can supply the total output power of 60 kW. This CMC is build based on a Mn-Zn ferrite toroidal core with an external diameter of 90 mm.

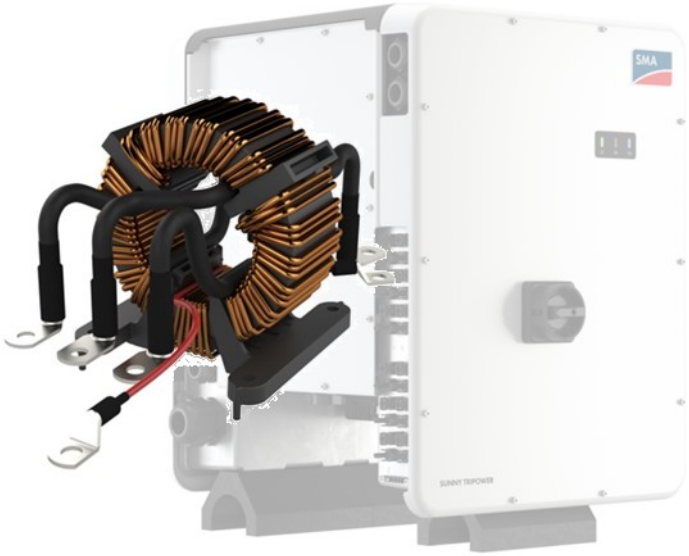


Figure 1. Common mode choke for PV inverter.

There has been a lot of work presented to reduce the size and improve the performance of the EMI filters [15]. However, a comprehensive model is required for CMC analysis and prediction. Higher switching frequencies and constantly growing power densities combined with increasing choke size causes the high frequency effects, usually considered to be insignificant, to start to dominate in the ferrite cores. Inductors, like the CMC, do not scale well with frequency and power, not only due to efficiency and power dissipation, but also due to high-frequency effects, such as the skin effect and the dimensional resonance. As an example, the toroidal core with an external diameter of 25 mm is large enough to exhibit non-uniform flux distribution due to skin and dimensional resonance effects [16]-[19]. For high permeability and permittivity materials, non-uniform flux distribution is apparent at 1 MHz. However, identification of these effects at the early design stage require detailed magnetic material characteristics. CMC design, with a magnetic core diameter of approx. 90 mm, based on the available material information without regard for the physical size of the core, may require many iterations and tests, and in the end may not prove feasible. Generally, specifications set forth by ferrite manufacturers provide average material characteristics which may be of limited use for detailed analysis [20]-[22]. The relatively poor quality of material data can jeopardize efficient design processes for the high-power and high-frequency magnetic components. Therefore, high-fidelity characteristics of magnetic materials are required. Magnetic material selection is of key importance for successful CMC design and to match the filter attenuation characteristic with the EMI source.

This dissertation introduces methods that are used to determine Mn-Zn ferrite properties at high frequency, and generate the required characteristics for an efficient design process of

magnetic components. New magnetic material characteristics are used to present a detailed analysis of the magnetic flux distribution in various Mn-Zn ferrite ring cores. Developed models include high-frequency effects visible within the core itself, such as skin effect and dimensional resonance. Predicted high-frequency flux distributions are validated experimentally by means of a novel method based on small holes bored precisely into the ferrite core. Finally, an innovative core structure, which overcomes unequal flux distribution, is proposed and experimentally validated.

The objective of this chapter is to provide a brief introduction to high-power and high-frequency EMI filters. It also highlights the main challenges in the design process, as well as the reasons for developing solutions for improvement. Section 1.1 presents an overview of the motivation for the work described in the thesis. Section 1.2 goes on to describe the four main objectives of the thesis. Section 1.3 gives a chapter-by-chapter summary of the thesis. Section 1.4 discusses the impact of the new wide-bandgap semiconductors on the EMI spectrum, and the limitations in the magnetic material specification available in the manufacturers` catalogs. Furthermore, it highlights how critical magnetic material definition may be for an efficient design process. Finally, Section 1.5 explains the fundamentals of skin depth and dimensional resonance in ferrite cores.

1.2 Thesis objectives

The thesis has the four objectives.

The first objective is to propose a method to determine the high-frequency properties of Mn-Zn ferrites. Magnetic component performance depends on the magnetic material. Therefore, the material selection is critical for an efficient design. Magnetic materials may be characterized by their complex permeability and permittivity. As these two parameters are of differentiated physical origin, two independent measurements are required. The proposed measurement methods must consider the size of the sample, ambient temperature, and the influence of the compression force on the complex permeability and permittivity measurements. However, high-frequency effects such as the skin and dimensional resonance cannot affect the parameters being measured. Moreover, the proposed method must be easy to use and implement as the obtained results are intended to be a foundation for further discussion concerning standardized testing procedures for magnetic materials.

The second objective is to present a comprehensive investigation of magnetic flux distributions in Mn-Zn ferrite cores. Once the performance of the material is known, it must be addressed with a specific model. The model must provide superior prediction for the high frequency effects, such as skin depth and dimensional resonance. The Finite Element Method

(FEM) is known as the most accurate method for magnetic flux calculation. However, it can be extremely time consuming while the software is not affordable by everyone. The developed models should be applied to all circuit simulators, or computing software, and also easily incorporated into a simulation of higher-order systems. The achieved results must be compared with experimentally-measured core complex permeability for various core materials and sizes.

The third objective is to develop a method for experimental validation of magnetic flux distribution in the ferrite core. The complex permeability characteristic does not provide detailed information on the flux distribution in a ferrite core. Until now, only FEM enables us to visualize the flux distribution in the core. The purpose of the new method is to verify the FEM flux pattern. The proposed method must be easy to implement because the flux propagation test is likely to be adopted as a standard test for magnetic core specification. Furthermore, the proposed method should not affect magnetic flux distribution.

The magnetic component is key for a successful EMI filter design. Thus, the final objective is to propose a core structure that can overcome unequal flux distribution and improve the overall EMI filter performance. Effectiveness of the new core structure must be compared with state-of-the-art cores at component level, through complex permeability characteristics, while at the system level through attenuation characteristics of the cores implemented into a single-phase EMI filter. The proposed core structure should also be possible to use in mass manufacturing.

1.3 Thesis Structure

This thesis is divided into 6 chapters. Chapter 1 is the introductory chapter and it gives a short summary of the motivations behind the research undertaken, as well as its objectives. The continuous drive for high-performance energy conversion and the application of WBG semiconductors, have triggered a great demand for high-performance EMI filters. Consequently, the magnetic component constitutes the key component of the EMI filter, while the high power and switching frequencies have set new limits to magnetic component design as well as magnetic material selection. An analysis of switching frequency and higher rate of voltage (*dv/dt*) transients on EMI harmonic spectrum is given, while the advantages related to the use of the WBG semiconductors are contrasted with challenges that comes with it. A review of the Mn-Zn ferrite material characteristics included in the ferrite manufacturers specification, together with their limitations, is also presented. Skin depth and dimensional resonance effect, within the magnetic core are then explained and compared with the same effect within the electrical conductor.

Chapter 2 introduces new methods of determining the high-frequency properties of Mn-Zn ferrites as the ferrite manufacturer specifications provide only average material characteristics which are of limited use for detailed analyses. Accurate identification of the magnetic material characteristics minimizes calculation error. The magnetic materials are characterized by complex permeability, permittivity and power losses. Each measurement type requires an independent fixture and investigation as the measurement accuracy may be seriously distorted by physical sample size, temperature, force etc. Introduced methods show improvements in the identification of magnetic properties and highlights the impact of high frequency effects such as skin depth and dimensional resonance on material characteristics.

Chapter 3 discusses models aimed at investigating the high-frequency effects such as skin depth and dimensional resonance for various core materials and sizes. Three calculation methods for a detailed analysis of the magnetic flux distribution are presented and then contrasted. The 1-D analytical model, based on Maxwell`s equations, is used for the purpose of the magnetic field calculation within an infinite ferrite plate, wherein the plate thickness corresponds to the lowest cross-sectional dimension of the tested cores. The novel, shell-based transmission-line model (TLM) is very intuitive and might be applied in any circuit simulator. What is more, it may also be easily incorporated into a simulation of a higher-order system. The last model is based on the FEM and Maxwell 3D eddy-current field solver. The accuracy of the models is determined by a comparison of calculated and experimentally-measured characteristics of complex permeability for various core sizes and materials.

Chapter 4 presents an innovative method for experimental validation of the magnetic flux distribution in ferrite cores. A number of experiments were carried out in order to develop a non-uniform flux distribution, quantify the effects, and experimentally validate the FEM analysis. In various core sizes and materials, three sets of holes were bored to measure magnetic flux distribution. One set of bores consists of two vertical bores and one horizontal bore of 0.75 mm diameter each. The data acquired during the performed tests shows the flux in the four concentric shells of the core. Two independent measurements were performed on each tested core. During the first experiment, the voltage of each core segment was determined to calculate flux density. This test setup is based on a signal generator and an amplifier which feeds the reference winding. This enables testing of cores frequencies up to 1.5 MHz. Therefore, the second experiment was proposed to determine impedance and phase shift measured on each ferrite segment. The test setup with an impedance analyzer allows for tests up to 20 MHz.

Chapter 5 introduces a novel core structure aimed at preventing non-uniform flux distribution and improving the overall EMI filter performance. It has been known for decades that eddy-current losses in iron-based cores are limited by lamination. Since traditional

laminations are made of conducting material, the ferrite is perceived as a high-impedance bulk body. Therefore, ferrite was not considered as a laminated core. However, the ferrite structure may develop conductive paths in certain conditions. Thus, a structure of laminated Mn-Zn ferrite ring core is proposed to optimize the flux distribution. Three laminated cores of different sizes were used to measure the magnetic flux distribution and the complex permeability characteristic. The results were compared with a solid core made of the same material. Magnetic material selection as well as core size impact on the lamination performance are also presented. Two single-phase, common-mode, chokes based on the solid and laminar ferrite cores have been built and compared experimentally.

Finally, the summary and conclusions drawn from the research, together with suggestions for future work, are presented in Chapter 6.

1.4 General background

WBG semiconductors push the frontier of power electronics beyond the frequencies achievable to date. Thus, higher-switching frequencies set new requirements for EMI filter design as well as magnetic material selection.

1.4.1 Analysis of high-frequency pulse transitions on EMI generation

WBG semiconductors provide superior performance compared to silicon: lower switching losses, and higher voltage breakdown, operating frequencies and temperatures. However, the switching of power semiconductor devices is also recognized as the main source of EMI in power electronics converters. Generation of EMI is strongly related to the switching frequency and the higher rate of voltage transients (*dv/dt*) and current transients (*di/dt*), which are advantages of new WBG semiconductors. Trapezoidal switching waveform and Fourier analysis are introduced to demonstrate the effect of switching frequency and fast voltage transients (*dv/dt*) on the EMI spectrum. The trapezoidal waveform with symmetric rise, τ_r, and fall times, τ_f, used for an analysis is shown in Figure 2.

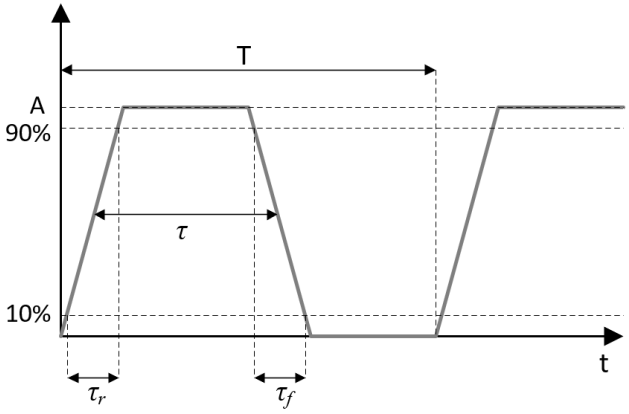


Figure 2. Trapezoidal waveform parameters.

The signal duty ratio D is given by τ/T, where $T = 1/f_0$ is the period of the switching waveform with a frequency f_0 while τ is the pulse width. The calculated EMI spectrum has an envelope which is described by a series of linear asymptotes featuring gradients: 0 dB/dec, -20 dB/dec, and -40 dB/dec with increasing frequency [23]. Corner frequencies f_{c1} and f_{c2} at which asymptotes intersect are determined by the waveform pulse width τ and rise time τ_r as follows:

$$f_{c1} = \frac{1}{\pi\tau} \tag{1.1}$$

$$f_{c2} = \frac{1}{\pi\tau_r} = \frac{1}{\pi\tau_f} \tag{1.2}$$

The emission spectrum of the three switching signals, representing the successive semiconductors generations, was calculated to expose their impact on EMI filter requirements. The parameters of the signals are presented in Table 1. The operating frequency of the semiconductors is taken as a most common for the respective type of semiconductors [5], [7].

In the case of this analysis, only the waveform with $D = 0.5$ is considered. Calculated spectral characteristics of the three switching signals are shown in Figure 3.

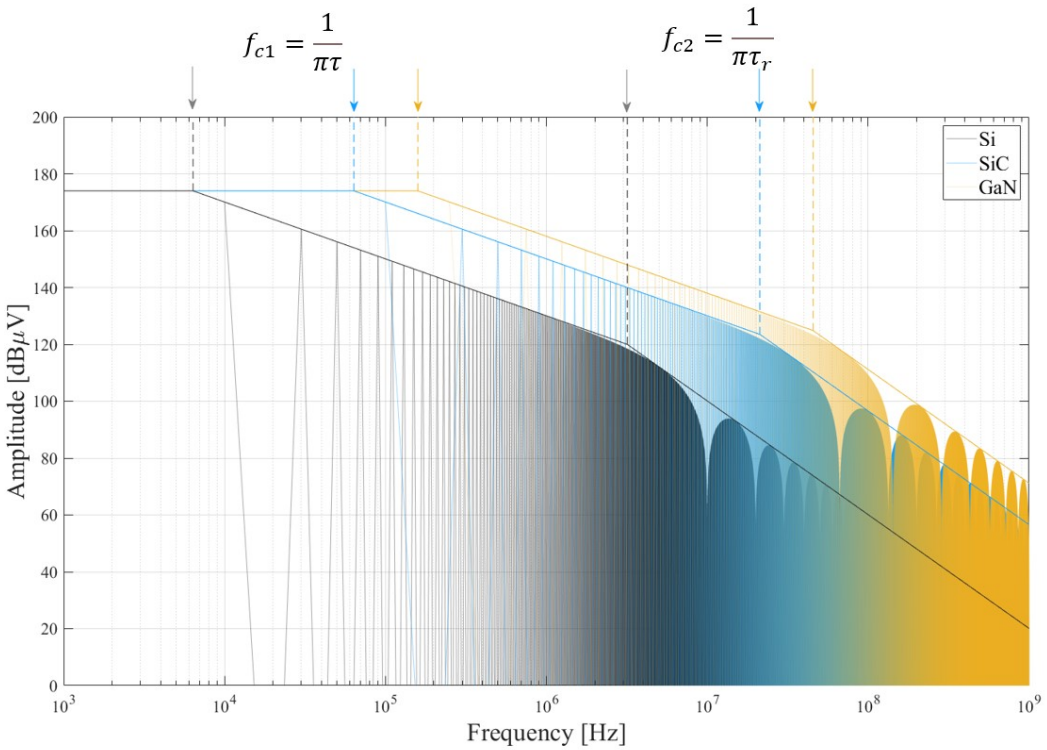


Figure 3. EMI emission spectrum comparison: Si vs. SiC vs. GaN.

The most important observation from this analysis is that the high-frequency content of the examined signals is significantly affected by the changing rise/fall time as well as the switching frequency. SiC semiconductors with rise/fall time 6.5 times lower and switching

TABLE 1. TRAPEZOIDAL SIGNAL PARAMETERS.

	Si	SiC	GaN
Amplitude	500 V	500 V	500 V
Switching frequency f_0	10 kHz	100 kHz	250 kHz
Rise/fall time $\tau_r = \tau_f$	100 ns	15 ns	8 ns
First corner frequency f_{c1}	6.36 kHz	63.66 kHz	159.15 kHz
Second corner frequency f_{c2}	3.18 MHz	21.22 MHz	45.47 MHz

frequency 10 times higher than classic Si-based devices cause an increase of EMI noise by 30 dB at 1 MHz. Using GaN's semiconductors with even lower rise/fall times and a switching frequency of around 250 kHz further increases the high-frequency spectral content. As illustrated in Figure 3, trapezoidal switching waveform and Fourier analysis shows that a switching frequency increase from 10 to 250 kHz has an effect only on the low-frequency spectrum envelope. High-frequency signal spectra are significantly more determined by rise/fall time than by fundamental frequency of the waveforms. WBG semiconductors cause a shift of the EMI envelope to higher frequencies. This shift to higher frequencies creates quite a challenge for the magnetic component design. Negligible until now, high frequency effects within magnetic cores, along with a higher influence of the filter parasitics and couplings must be addressed with specific models and more advanced designs to provide high-performance EMI filter designs.

1.4.2 Magnetic materials for EMI filters

Magnetic material selection is key for successful magnetic component design. Soft magnetic materials are commonly used for transformers, inductors, and EMI filters due to their favorable magnetic properties such as low magnetic coercivity. This thesis focuses on MnZn ferrites; however, other popular materials used for EMI filter applications are also briefly characterized [24]-[25].

The ideal material for the EMI filter should feature high saturation flux density and high resistivity (as eddy-current losses are inversely proportional to the electrical resistivity). The material should also feature a constant permeability characteristic over frequency and temperature, low permittivity, high mechanical robustness, and insensitivity to mechanical stress. The general specification of the material for EMI filters is presented in Table 2. The main parameters, often used as a point of comparison for soft magnetic materials, include relative permeability, μ_r, saturation flux density, B_{MAX}, as well as electrical conductivity, σ. The table is based on published manufacturer information, as well as experimental investigation carried out as part of the thesis. Soft magnetic materials can be differentiated into four different material groups: amorphous, nanocrystalline, ferrites and iron-nickel alloys.

Amorphous metals are iron-based alloys of cobalt, nickel, boron, silicon and manganese. Amorphous alloys are produced as thin ribbons that allow wound cores to be produced, mainly as toroidal cores; however, U-cores and blocks are available as well. The amorphous alloy structure, due to its rapid quenching, solidifies in an unorganized liquid structure that reassembles the structure of glass. Atoms are in disorder as no crystalline order may exist in that structure. The major advantages of amorphous materials are the low power losses, a linear hysteresis loops with low coercivity, and a saturation flux density of 0.7 – 1.8

T, which is almost completely retained at high frequency. Moreover, amorphous materials are characterized by low temperature dependence, or even a negative temperature coefficient. The Curie temperature of amorphous materials is in the range of 350 – 450 °C.

Nanocrystalline material is a two-phase structure consisting of an ultra-fine grain phase embedded in an amorphous minority phase [27]-[28]. The production process is similar to the amorphous material, however, additional annealing, together with a directed magnetic field, is applied to align magnetic domains. The annealing process increases the nanocrystalline material brittleness, and thus limits the feasible core shapes to ring cores. The cores are usually epoxy coated or placed within a plastic enclosure. Nanocrystalline soft magnetic materials exhibit a linear hysteresis loop with coercivities smaller than 2 A/m and a saturation flux density of 1.2 – 1.5 T.

TABLE 2. MAGNETIC MATERIAL PROPERTIES.

Manufacturer	Material	Type	Relative Permeability @10 kHz, 25°C	Saturation Flux Density (T) @10 kHz, 25°C	Curie temp (°C)	Density (g/cm^3)	Resistivity (Ω m)	Continuous operating temperature (°C)	Thermal conductivity (W/m K)
Vacuumschmelze	Vitrovac 6030F	Amorphous	3500	0.82	365	7.80	$1.3x10^{-6}$	120	10.5**
Vacuumschmelze	Vitrovac 6025	Amorphous	70000-100000	0.58	240	7.70	$1.4x10^{-6}$	120	10.5**
Metglas Inc.	2605S3A	Amorphous	35000	1.41	358	7.29	$1.38x10^{-6}$	150	10.0**
Hitachi Metals	Magnaperm 2714A	Amorphous	> 72000	0.57	225	7.59	$1.42x10^{-6}$	90	10.5**
Vacuumschmelze	Vitroperm 250F	Nanocrystalline	4000-6000	1.20	600	7.35	$1.15x10^{-6}$	180*	10.5**
Vacuumschmelze	Vitroperm 500F	Nanocrystalline	15000-150000	1.20	600	7.35	$1.15x10^{-6}$	180*	10.5**
Magnetec	Nanoperm	Nanocrystalline	5000-200000	1.20	600	7.35	$1.15x10^{-6}$	200*	10.5**
Hitachi Metals	Finemet-1M	Nanocrystalline	70000	1.23	570	7.40	$1.1x10^{-6}$	180*	10.5**
Hitachi Metals	Finemet-3L	Nanocrystalline	50000	1.23	570	7.30	$1.2x10^{-6}$	180*	10.5**
Ferroxcube	3S5	Ferrite	3800	0.54	255	4.80	10.00	180*	3.5-5
Ferroxcube	3E27	Ferrite	6000	0.43	150	4.85	0.50	140	3.5-5
Ferroxcube	3E10	Ferrite	10000	0.46	130	5.00	0.50	125	3.5-5
Ferroxcube	3E12	Ferrite	12000	0.47	130	5.00	0.50	125	3.5-5
DMEGC	R15K	Ferrite	15000	0.36	110	4.90	0.05	110	5.0
DMEGC	R10KZ	Ferrite	10000	0.38	120	4.90	0.15	115	5.0
DMEGC	R10K	Ferrite	10000	0.40	120	4.90	0.15	120	5.0
Ferroxcube	4B1	Ferrite	250	0.36	250	4.60	10^5	180	3.5-5
Ferroxcube	4S60	Ferrite	2000	0.26	100	5.00	10^5	100	3.5-5
MAGNETICS	Supermalloy	Iron-Nickel	70000-100000	0.82	460	8.70	$0.57x10^{-6}$	180*	TBD
MAGNETICS	Permalloy 80	Iron-Nickel	20000-50000	0.82	460	8.70	$0.57x10^{-6}$	180*	TBD
Vacuumschmelze	Vitrovac 6025	Amorphous	80000	1.25	450	TBD	$0.57x10^{-6}$	180*	10.0**

*Limited by the box material, ** Along the lamination

The initial permeability of the material is adjustable within the range of 15 000 to 150 000. The dependence of the initial permeability of the nanocrystalline soft magnetic materials on temperature is almost linear, while the change over in the temperature range, –40 °C to 120 °C, is about 6%. The Curie temperature of nanocrystalline materials is about 600 °C. High and temperature stable permeability makes nanocrystalline materials more expensive than other materials.

Ferrite is a bulk material sintered out of iron oxides (Fe_2O_3) combined with oxides or carbonates of manganese and zinc (MnZn) or nickel and zinc (NiZn). These materials are pressed and then sintered at temperatures of 1000 – 1500 °C, and as a result the ferrites are not only hard but also brittle. Due to the manufacturing process, ferrite cores are available in various shapes and sizes. Since the chemical composition and the microstructure strongly affect the properties of ferrites, the initial permeability, electrical conductivity, and the Curie temperature can be controlled by raw material quality together with sophisticated additives, or a strictly monitored production process. Magnetic properties of soft ferrites are sensitive to temperature. The saturation flux density at 100 ℃ can only be about half of the value at 20 ℃, depending on the type of soft ferrite. Ferrites are one of the most popular materials in power electronic applications due to relatively low costs and power losses [18].

A comparison of magnetic material saturation vs. permeability dedicated for EMI applications is presented in Figure 4.

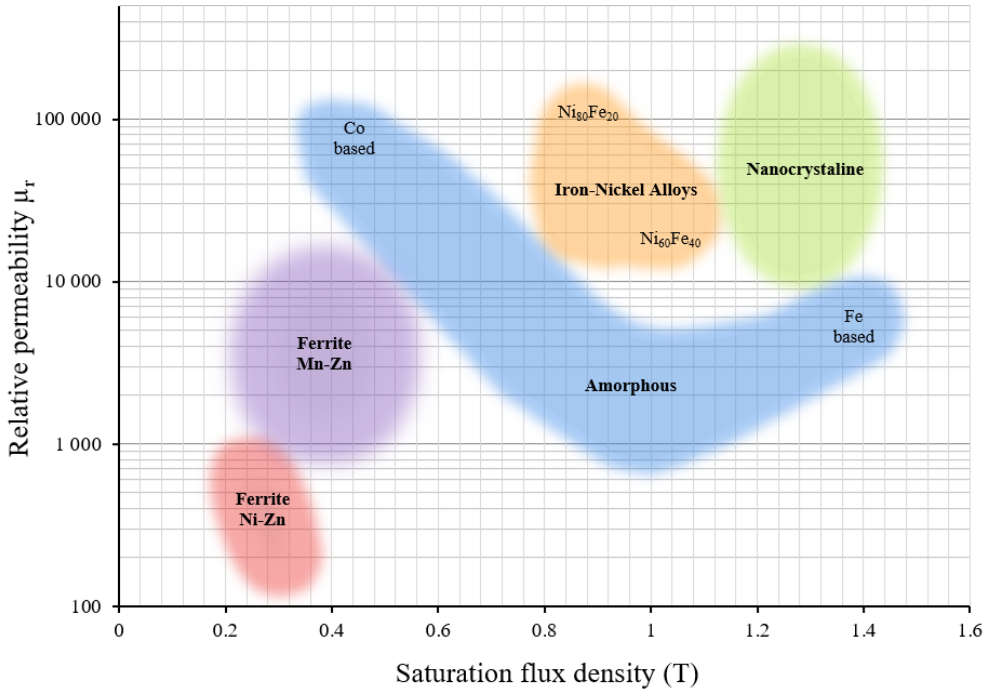


Figure 4. EMI materials relative permeability vs. saturation flux density.

Nanocrystalline and Fe-based amorphous materials have the highest saturation flux density, followed by iron-nickel alloys, Co-based amorphous and finally ferrites. Material with high relative permeability and high saturation flux density reduces the CMC size as it allows for lower turns, and thus directly reduces copper losses and capacitance, while improving EMI filter performance at high frequency.

Higher switching frequencies set new limits for magnetic component design and magnetic material selection. Due to the high-frequency capabilities nowadays, the MnZn ferrites are still of primary interest for the investigation of high-performance magnetic components. Ferrite manufacturers have responded to the increased demand for improvement of MnZn ferrites, and offer low-cost materials with lower losses, but higher permeability. However, the combination of the high permeability and the high permittivity of MnZn ferrite may affect the high-frequency performance due to eddy currents and dimensional resonance. By default, the ferrite manufacturers' specifications provide average material characteristics which may be of limited use for detailed analysis. The material definition in the manufacturers' specification is limited to ferrite parameters provided as a constant for the entire ferrite family range. A good example of this is the ferrite permittivity and conductivity. Sample plots of the real part of permittivity and conductivity over frequency for the entire Mn-Zn ferrite family are shown in Figure 5 [20].

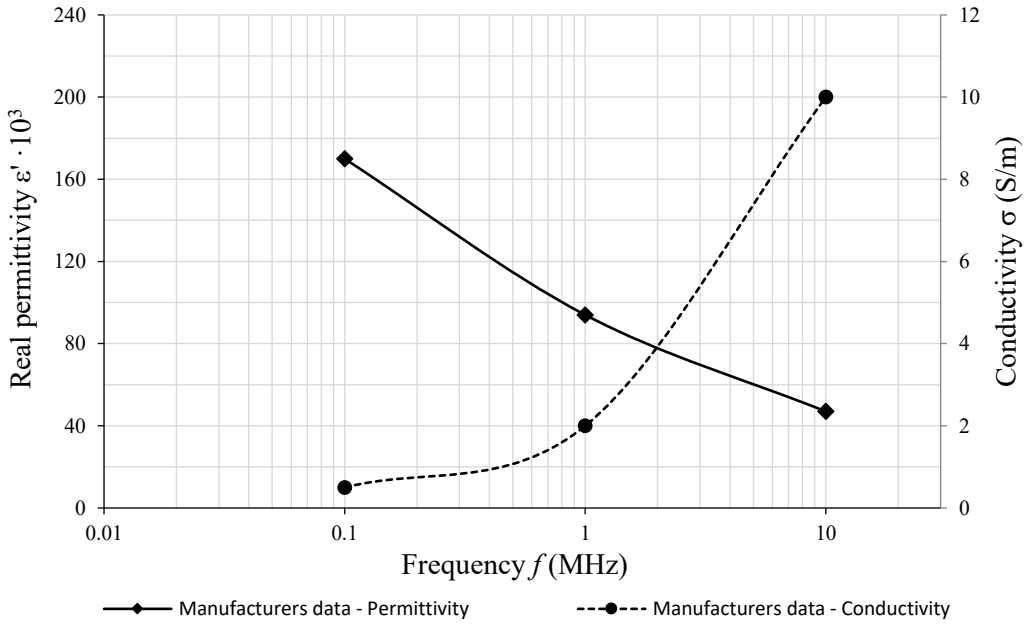


Figure 5. Ferrite electrical properties for all Mn-Zn ferrite family based on the ferrite manufacturer specifications [20].

The material datasheets provide common parameters for all Mn-Zn ferrites, excluding details of frequency dependence. This makes the core material selection during the design somewhat cumbersome due to excessive design iterations. As a result, state-of-the-art magnetic core modelling assumes ferrite permittivity and conductivity to be negligible for magnetic component design process. Therefore, high frequency effects in ferrites are also omitted in the calculations as skin depth and dimensional resonance strongly depend on magnetic material conductivity and permittivity. The high frequency effects may dominate core performance. Therefore, the effects of permeability, permittivity and conductivity on core performance are of particular interest. In order to quantify the effects of core permeability, permittivity and conductivity on the core performance, three simulations were performed.

FEA was used as the most feasible method for magnetic flux calculation as it reproduces the flux distribution. The calculations use a 3-D eddy-current field solver, while the simulation was performed at 500 kHz for three combinations of material parameters, are shown in Figure 6, Figure 7 and Figure 8, respectively.

The first simulation shows an ideal case of a lossless core. As anticipated, the flux distribution is dominated by reluctance, which results in the magnetic flux intensity being stronger at inner radius, and decreasing as the radius increases. This is the most common flux distribution pattern in a toroidal magnetic core which is not affected by high-frequency effects.

In the second simulation, the relative permittivity is set to 50,000. Inside the ferrite core, a large amplitude flux occurs under resonant conditions, and is concentrated in the inner part of the core cross section. The combination of the high permeability, the high permittivity and the relatively large cross-sectional dimension of the core give rise to standing electromagnetic waves within the ferrite. This effect is called the dimensional resonance.

The third simulation shows a combination of low material permittivity, but with a high conductivity of 5 S/m. The magnetic flux density distribution is similar to the known current distribution in a electrical conductor. Intuitively, the magnetic flux is concentrated in the outer circumference while at the same time the core center exhibits flux density weakening due to the skin effect. Ferrite cores are typically used for high-frequency magnetic components due to low conductivity. The low saturation flux density of ferrites means that a high-power core must be relatively large. The low conductivity of ferrites justifies the use of large core blocks of ferrite since eddy-currents losses are also low. If ferrite conductivity is higher, or conductivity strongly increases with frequency, contrary to what was provided in the specification, large cores used for high-power, high-frequency designs may require many iterations and design changes.

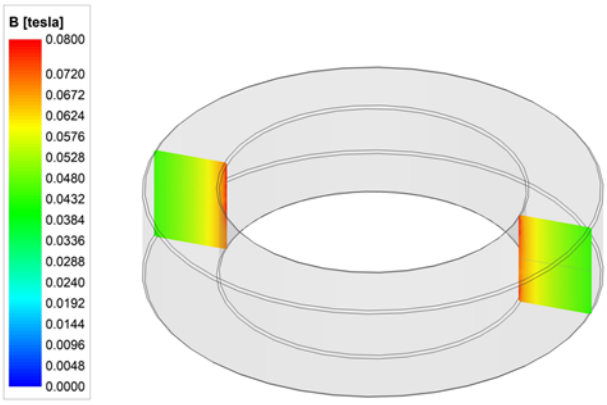


Figure 6. FEA results of the flux distribution in the T90 core, simulation 1 - ideal: f = 500 kHz, μ_r, = 10 000, ε_r = 1, σ = 0.1 S/m.

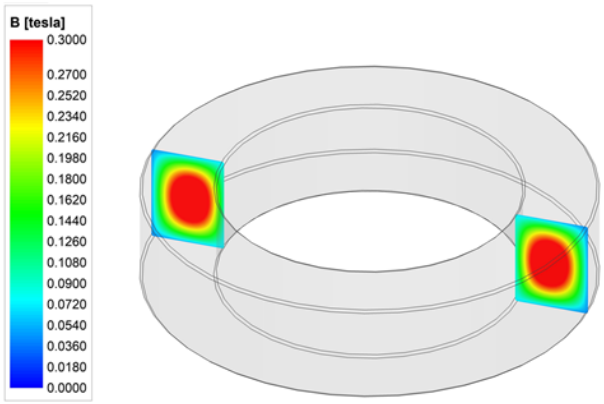


Figure 7. FEA results of the flux distribution in the T90 core, simulation 2 - permittivity included: f = 500 kHz, μ_r, = 10 000, ε_r = 50 000, σ = 0.1 S/m.

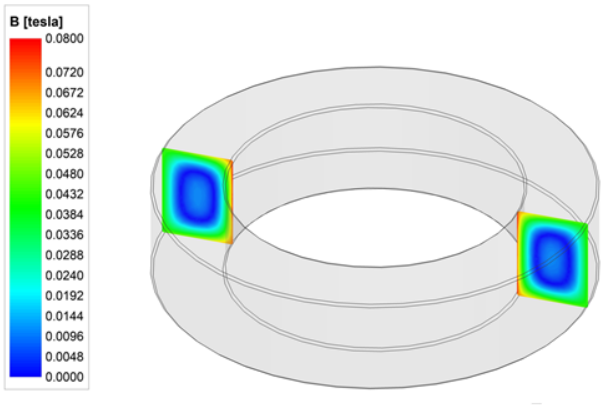


Figure 8. FEA results of the flux distribution in the T90 core, simulation 3 – conductivity included: f = 500 kHz, μ_r, = 10 000, ε_r = 10 000, σ = 5 S/m.

Introduction of ferrite permittivity and conductivity into the simulation exposes its significance on the core performance. Ferrite magnetic materials are subject to high frequency

effects which result in non-uniform frequency-dependent magnetic flux distributions. The material conductivity and permittivity must be taken into account during the component design processes due to the direct impact on the core's effective permeability, impedance and inductance. Only the identification of all magnetic material properties can allow for a precise estimation of the flux distribution in the ferrite core.

Ferrite properties are influenced by the many variables such as frequency, temperature, physical size, mechanical stress, and even batch-to-batch material variations. It is impossible for ferrite manufacturers to provide all the information required by users. Therefore, the datasheet on magnetic materials must be balanced in order to provide a reasonable level of information for most customers. The complex permeability and permittivity of materials are the key parameters for the EMC filter design process as they directly impact the power losses and inductance. The interpretation of the performance of magnetic materials in relation to frequency, physical size, temperature, and mechanical stress must be addressed with a specific model in order to provide high quality physical phenomena prediction.

1.4.3 The magnetic design for inductors and filters

The fundamental principles of the magnetic design are valid across the range of applications, and trade-offs exist between the number of turns and the core size whilst being constrained by a number of physical effects that oppose the ideal performance. The magnetic design must conform with the industry standards, and provide a predictable parameters range within the tolerance, at acceptable cost.

The magnetic design for the EMC filter, although similar to the power inductor design, deals with high frequency effects that are usually negligible for power inductors. A typical approach for the inductor design can be found in various publications [29]-[31]. Key requirements are the peak flux density and impedance, the efficiency, the dc resistance of the winding and the parallel resistance that is proportional to the ac power loss at a given frequency. In order to fulfil these requirements a simple design flowchart [29] can be applied that guides us through the material selection, the magnetic core sizing, the winding calculation, the power loss calculation, and the temperature rise estimation. The design flow is usually iterated until the design constraints are satisfied. The accuracy of the calculation flowchart depends on the model degrees of freedom and the quality of the input data.

The inductors for EMC filters must provide wide frequency attenuation to the disturbance produced by the switching cell of the converter. The wide-bandgap semiconductor spectrum is at a much higher level than standard silicon, as presented in Figure 3. Therefore, the most feasible model is based on a complex permeability that allows for modelling across the frequency range. The accuracy of the model parameters impact component performance.

The dynamic effects that are linked with operating frequency vs. size limit the performance of the component. Therefore, the frequency dependence of the material properties for a given size of the magnetic core define the component performance. The frequency related eddy current and dimensional resonance depend on the material properties and it is critical for the design algorithm to account for both phenomena. The correct identification of parameters enables accurate prediction of the high frequency dynamic phenomena in ferrites and thus reduces the iterations for the magnetic design by selecting the right material, size and winding setup. As presented in this thesis, the effects of the accurate material properties such as permeability and permittivity are fundamental to a high quality design process.

The consequences of modelling based on accurate material properties overcome the limits of the design process and help mitigate the adverse dynamic effects caused by using the inaccurate data usually provided in the magnetic core datasheets.

A plot of required impedance od the CMC is shown in Figure 9. This is from previous work of the author in [32]. The design flow is an important function of the filter. As discussed in [32] the design flowchart can be adopted to seek the optimum impedance trajectory. The CMC filter provides an impedance characteristic that varies with the frequency and changes its amplitude and angle to follow the desired frequency response. The detailed knowledge of the material properties is fundamental for material selection and prediction of the component characteristic and so is the focus of this thesis, rather than magnetic design.

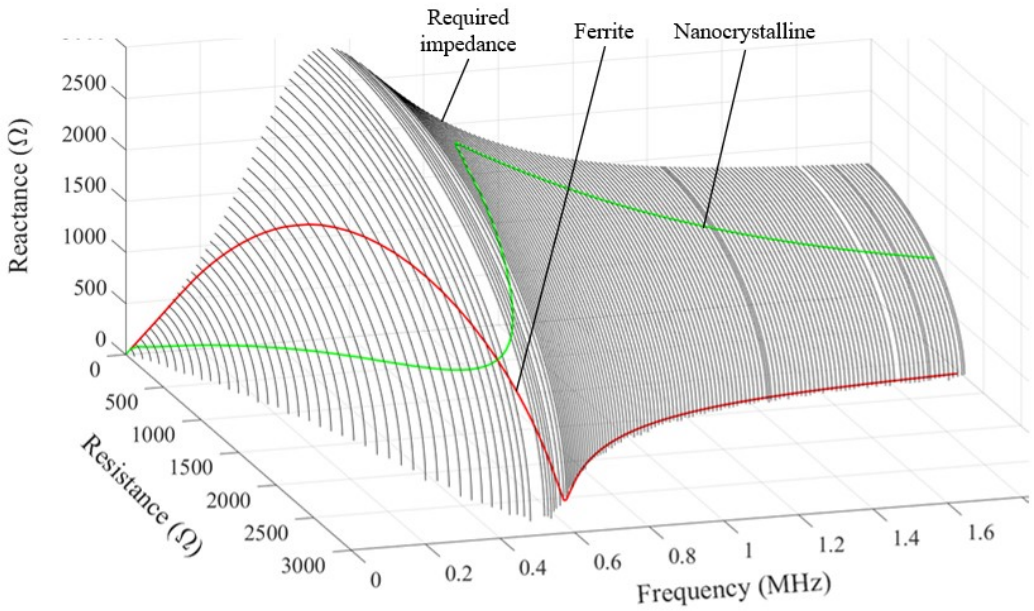


Figure 9. Common-mode choke impedance vs. frequency [32].

1.5 High-frequency effects in the magnetic core

This section briefly presents the theory which will be further used in Chapters 2 and 3.

1.5.1 Application of Maxwells equations

In the 19th century, a Scottish scientist, James Clerk Maxwell, developed a scientific theory to explain the notion of electromagnetic waves. He noted that both electrical and magnetic fields can couple together to form an electromagnetic wave. He summarized this relationship between electricity and magnetism into a theory known as "Maxwell's Equations". In the time-domain representation, and assuming that the electric field has one component while the propagation is in the z direction, the electromagnetic wave equation yields the following expression [33]:

$$\bar{E}(z,t) = E_0 e^{-\alpha z} \cos(\omega t - \beta z) \tag{1.3}$$

The visualization of the electromagnetic wave propagating through a lossy material is shown in Figure 10. However, the traditional electromagnetic wave visualization presents certain drawbacks. As show in Figure 10, the wave is confined to be on z axis, which is not true. The plane wave is extended in the x and y directions. The second simplification involves the magnitude of the magnetic and electric field. In reality, both electric and magnetic fields are related through material impedance. As an example, the impedance of a vacuum is around 376.7 Ω, and so the electric and magnetic fields are three orders of magnitude different from each other, which would not be possible to draw in the same scale.

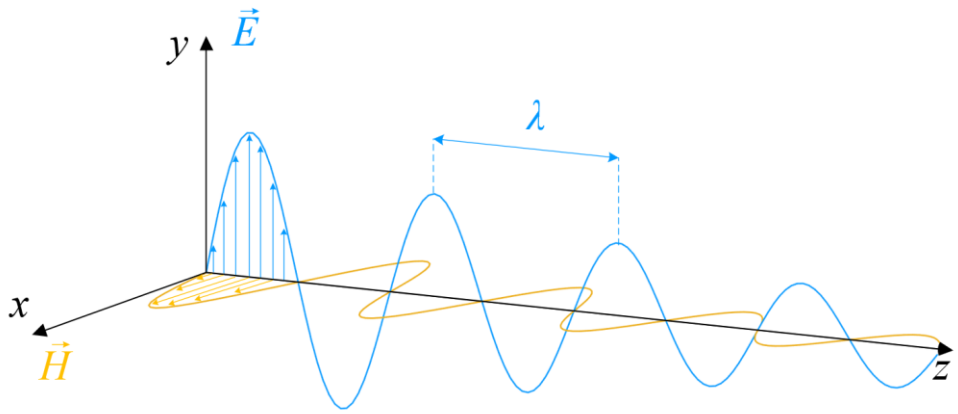


Figure 10. Visualization of electromagnetic wave propagation in lossy material.

The propagation velocity v of the electromagnetic wave in the material, as defined by permeability μ and permittivity ε, is given by:

$$v = \frac{1}{\sqrt{\mu\varepsilon}} \tag{1.4}$$

When an electromagnetic wave propagates in a vacuum permeability equals that of free space ($\mu = \mu_0$) and the permittivity equals that of free space ($\varepsilon = \varepsilon_0$), and the propagation velocity becomes what we commonly refer to as speed of light c_0:

$$c_0 = \frac{1}{\sqrt{\mu_0\varepsilon_0}} = 299\,792\,458\ \frac{m}{s} \tag{1.5}$$

Ferrite material can by characterized by complex permeability and permittivity. The imaginary parts of the permeability and permittivity describe the losses within the ferrite material, while the real parts of the permeability and permittivity present the capability to store reactive energy. As both parameters $\bar{\mu}$ and $\bar{\varepsilon}$ are complex, the wave propagation velocity, $\bar{v}$ is also complex:

$$\bar{v} = \frac{1}{\sqrt{\bar{\mu}\bar{\varepsilon}}} = \frac{1}{\sqrt{(\mu' - j\mu'')(\varepsilon' - j\varepsilon'')}} \tag{1.6}$$

Ferrites have high permittivity and permeability. Therefore, the electromagnetic waves that enter the ferrite propagate slower than in free space, or equivalently, the wavelength in the ferrite is shorter than in free space. The wave speed $\bar{v}$, the frequency f, and wavelength $\bar{\lambda}$ are related by:

$$\bar{\lambda} = \frac{\bar{v}}{f} = \frac{2\pi}{\omega\sqrt{(\mu' - j\mu'')(\varepsilon' - j\varepsilon'')}} \tag{1.7}$$

Frequency is the most fundamental attribute which describes the electromagnetic wave as it never varies in linear materials [29]. Wave number $\bar{k}$ combines wavelength, frequency and the material characteristic as follows:

$$\bar{k} = \frac{2\pi}{\bar{\lambda}} = \omega\sqrt{(\mu' - j\mu'')(\varepsilon' - j\varepsilon'')} = \beta - j\alpha \tag{1.8}$$

The imaginary part of the wave number α is an attenuation constant and defines the rate of extinction of the wave in a material. The real part of the wave number β is a phase constant which is a measure of the phase shift per unit length. The wavelength is related to the phase

constant. Therefore, an expression of the real part of the complex wave number provides an equation for the wavelength as an imaginary part for skin depth [29].

$$\alpha = -Im[\bar{k}] = \frac{1}{\delta} \Rightarrow \delta = \frac{1}{\alpha} \tag{1.9}$$

$$\beta = Re[\bar{k}] = \frac{2\pi}{\lambda} \Rightarrow \lambda = \frac{2\pi}{\beta} \tag{1.10}$$

1.5.2 Dimensional resonance and skin depth

In low-loss magnetic materials, the electromagnetic wave travels without significant energy loss. If the smallest cross-sectional dimension of the core (perpendicular to the magnetic and electric field) is equal to half a wavelength, then a standing wave will be formed across the cross section of the core. Under these specific conditions, the surface flux which is in phase with the surface magnetic field is cancelled out by antiphase flux at the core center. This phenomenon is called dimensional resonance and it is characterized by the permeability dropping to zero.

A standing wave is a combination of two waves moving in opposite directions, each having the same amplitude and frequency. The phenomenon is a result of interference while the energies of the waves are either added up or cancelled out. For opposite moving waves the interference produces an oscillating wave fixed in space. In order to visualize this effect, three simulations were performed. The FEA calculations use a 3-D eddy-current field solver. Moreover, the simulation is performed at 500 kHz for three combinations of two sine wave traveling in opposite directions, results are shown in Figure 11, Figure 12 and Figure 13, respectively.

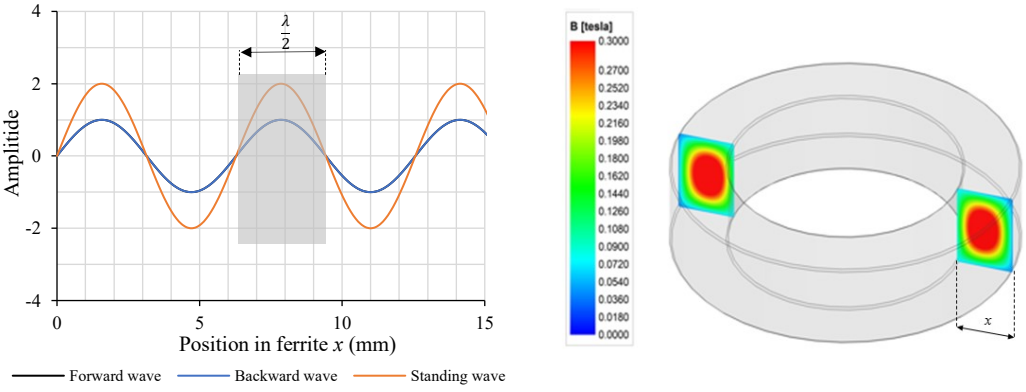


Figure 11. Standing wave visualization based on the FEA, forward and backward waves are in phase.

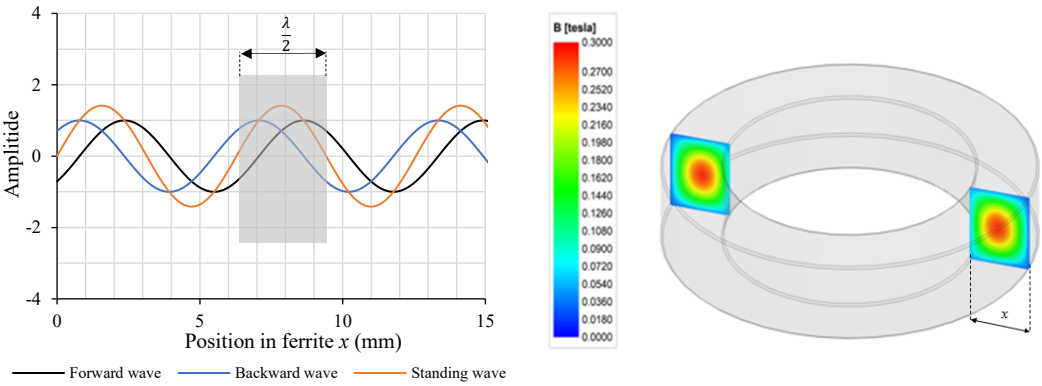


Figure 12. Standing wave visualization based on the FEA, forward and backward waves are shifted by 90°.

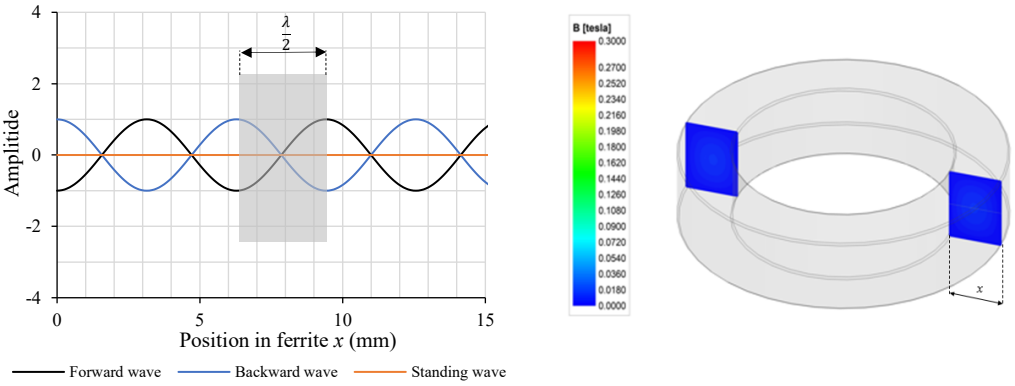


Figure 13. Standing wave visualization based on the FEA, forward and backward waves are shifted by 180°.

As shown in Figure 10 to Figure 12, the black wave is moving in the +x direction while the blue one is moving in the -x direction. The resulting wave is shown in orange. The grey envelope on the figures outlines the cross-sectional dimension of the core, with its smallest cross-sectional dimension equal to half a wavelength. The points where the standing wave is always equal to zero are defined as wave nodes. In relation to the core size where the smallest cross-sectional dimension of the core is equal to half a wavelength, these points are located at the core's outer circumference. Between each of the nodes, there is an antinode, a place where the wave oscillates with an amplitude equal to the sum of the amplitude of each of the waves. In this case, the antinode is situated at the core center. Different points in time show different core flux distribution for the exact excitation. The highest flux amplitude occurs in the core center when two waves are in phase and it is concentrated in the inner part of the core, in the antinode. Flux amplitude slowly decreases with increasing phase shift between the waves, and is equal to zero when waves are shifted 180°. Dimensional resonance directly affects core permeability and, as a result, it also has an influence on inductance and impedance.

Magnetic materials with higher losses will not support standing waves as the electromagnetic wave is attenuated very quickly. Instead, the depth of the electromagnetic wave penetration will be observed and will later be referred to as skin depth. The skin depth is inversely proportional to the wave attenuation constant. The skin depth is defined as the equivalent depth where the electromagnetic wave can penetrate the material by a factor of *1/e*. The same effect is visible in the winding which conducts high-frequency electric current. Skin effect for electric current and magnetic flux is illustrated in Figure 14.

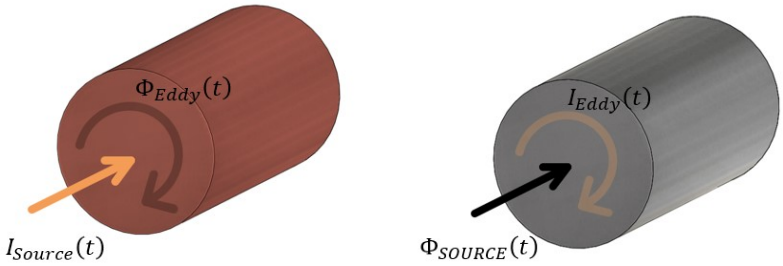


Figure 14. Skin effect in electrical conductor carrying current and magnetic core carrying flux.

The alternating magnetic flux induces a counter magnetic flux in the core made of conductive material whose dimensions are large enough to carry eddy currents. Eddy currents are closed loops of induced current circulating in planes perpendicular to the magnetic flux.

The depth at which the eddy currents and electromagnetic waves penetrate into a material is affected by frequency, conductivity and magnetic permeability of the material. The penetration depth decreases with increasing frequency, conductivity and magnetic permeability. Therefore, high frequency can be considered the level at which the parasitics would have an effect on the performance of the core.

Ferrite magnetic materials are subject to high-frequency effects such as dimensional resonance and skin effect within the core that result in a non-uniform, frequency-dependent magnetic flux distribution. The dimensional resonance and the skin effect are dependent on the size and shape of the core as well as the wave frequency. Dimensional resonance and skin depth in magnetic materials are defined by the electromagnetic wave and the properties of the core. Electromagnetic wave parameters, the attenuation constant, and the wave number define and quantify high frequency effects within the core. However, precise information on magnetic materials is mandatory for an in-depth analysis of high quality.

The calculated skin depths and wavelengths for the four different ferrite materials are shown in Figure 15 and Figure 16, respectively.

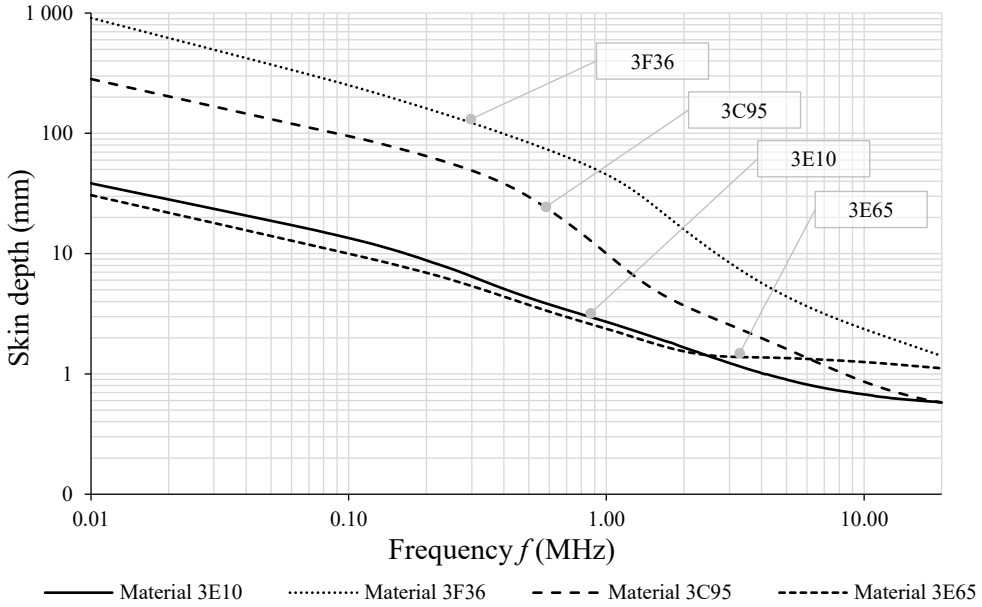


Figure 15. Skin depth in ferrite vs. frequency based on experimental data.

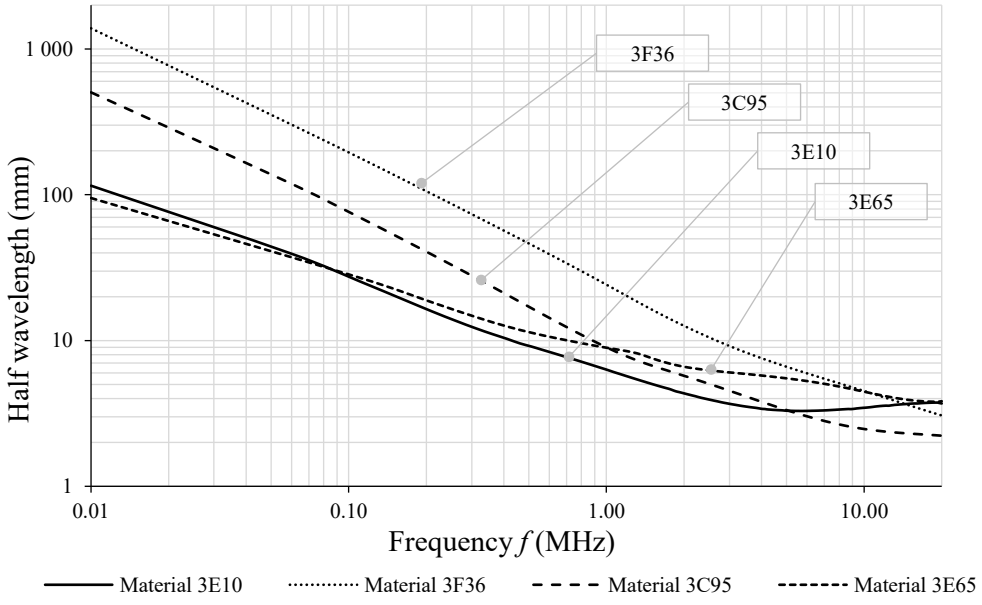


Figure 16. Electromagnetic half-wavelength in ferrite vs. frequency based on experimental data.

For all presented materials, the skin depth and wavelength are frequency dependent. The calculation is based on experimentally measured magnetic material parameters, from a later chapter. As can be seen in the presented figures, the calculated skin depth as well as the

wavelength are quite different in relation to the presented materials. What is more, both parameters drop as the frequency increases. For 3F36, the material skin depth and the half-wavelength are the highest. Material 3E10 shows the lowest value of the skin depth and the half-wavelength for the frequency range of 10 kHz up to 20 MHz.

In reality, ferrite skin depth and dimensional resonance occur together and interact producing an effective resultant flux distribution in the magnetic core. Presenting both parameters on the one graph, for each tested material, allows for high frequency effect identification within the magnetic core. The calculated wavelengths and skin depths for 3E10 and 3F36 material are shown in Figure 17. Additionally, the smallest T90 cross-sectional dimension of the core is indicated on the graph. The ring core T90 has an outer diameter of 90 mm, an inner diameter of 60 mm, and is 20 mm high. The smallest cross-sectional dimension of the core is 15 mm. For the T90 core, made of 3E10 material, the skin depth is smaller than half the wavelength for the entire frequency range. Magnetic cores made with 3E10 are dominated by skin depth caused by a combination of magnetic and electric losses. The electromagnetic wave is attenuated, and there is no dimensional resonance. For the T90 core, made of 3E10 material, skin depth effect within the core is visible at 80 kHz. For the T90 core, made of 3F36 material, wave propagation and attenuation must be considered together. At

1.7 MHz the smallest core cross-sectional dimension is equal to half a wavelength, while the core will be dominated by a dimensional resonance. As frequency increases, the skin effect becomes visible in the core at 2.66 MHz, while above this frequency the losses start to dominate.

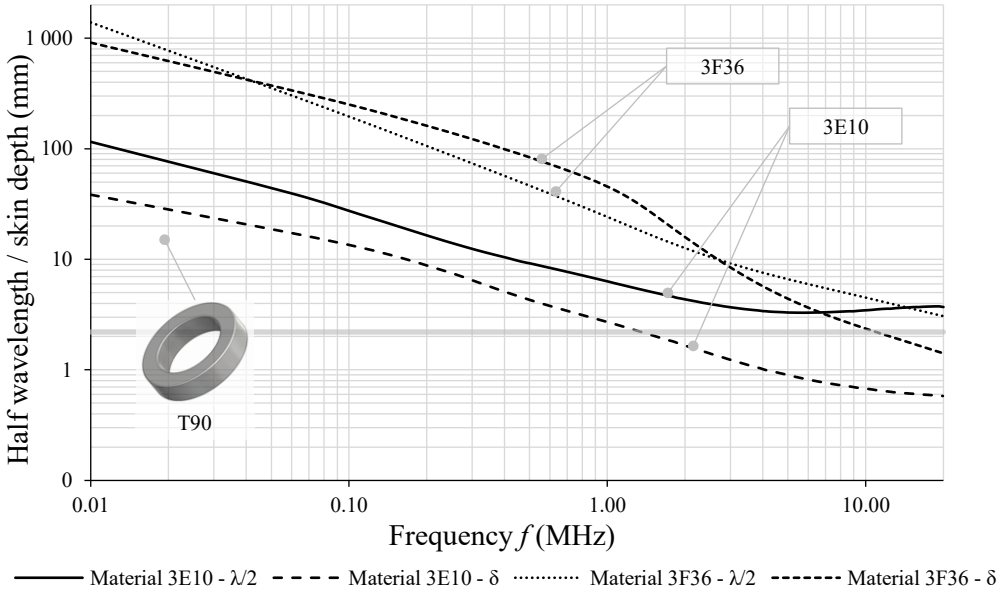


Figure 17. Electromagnetic wavelength and skin depth in ferrite 3E10 and 3F36.

1.6 Conclusions

The chapter presents the motivation for the work described in this thesis. Four main objectives of this thesis were presented and discussed in detail. The advantages arising from the use of the WBG semiconductors are contrasted with associated challenges. These include high switching frequencies, and higher rates of voltage transients (*dv/dt*). An analysis concerning the impact of those challenges on the EMI harmonic spectrum was briefly described. The WBG semiconductors cause a shift of the EMI envelope to higher frequencies and create a challenge for the magnetic component design. Successively limitations of the magnetic material specification, available in the datasheets provided by the manufacturers, were discussed. Furthermore, it was shown how critical the magnetic material definition may be for an efficient design process. Based on FEA simulations, it was shown that both the conductivity and permittivity of magnetic material must be taken into account during component design processes due to the direct impact of those parameters on the core's performance. Finally, a brief discussion was presented on the fundamentals of skin depth and dimensional resonance in ferrite cores.

2 HIGH FREQUENCY CHARACTERISTICS OF MN-ZN FERRITES

Abstract - The objective of this section is to develop experimental methods to determine the high-frequency properties of Mn-Zn ferrites. Magnetic material properties and, at the same time, material selection, constitute the basis for efficient design processes. As such, the first step is to accurately identify the high-frequency characteristics of MnZn ferrites. This chapter focuses on the implementation of new measurement methods as well as on the impact of the high-frequency effects, such as skin depth and dimensional resonance, on material characteristics.

Section 2.1 discusses the complex permeability frequency characteristics of Mn-Zn ferrites. Section 2.2 introduces a method used to determine the complex permittivity frequency characteristics of the core. Both characteristics, the complex permeability and permittivity, are examined for various core sizes and materials, including the influence of the temperature and the compression force. The core power loss analysis in shown in Section 2.3. A brief conclusion is presented in Section 2.4.

The results of this chapter have been published in the following papers and presentations:

- M. Kacki, M.S. Rylko, J.G. Hayes, C.R. Sullivan, "Magnetic Material Selection for EMI Filters," *IEEE Energy Conversion Congress and Exposition (ECCE),* Cincinnati, OH, 2017.
- M. Kacki, M.S. Rylko, E. Herbert, J.G. Hayes, C.R. Sullivan, "Magnetic Core Dimensional Effects – Flux Propagation in Ferrites," *Workshop on High Frequency Magnetics organized by PSMA and IEEE PELS*, Anaheim, CA, 2019.
- M. Kacki, M.S. Rylko, J.G. Hayes, C.R. Sullivan, "A Practical Method to Define High Frequency Electrical Properties of MnZn Ferrites," *IEEE Applied Power Electronics Conference and Exposition (APEC)*, New Orleans, LA, 2020.
- M. Kacki, M.S. Rylko, E. Herbert, "PSMA-SMA Special Project – Phase II, Investigation on Magnetic Flux Propagation in Ferrite Cores", *The Power Source Manufacturers Association Technical Report*, 2020.
- M. Kacki, M.S. Rylko, J.G. Hayes, C.R. Sullivan, "Measurements Methods for High-frequency Characterizations of Permeability, Permittivity, and Core loss of Mn-Zn Ferrite Cores," *IEEE Transactions on Power Electronics* (Early Access), July, 2022.

2.1 Complex permeability characteristic

The analysis of complex permeability frequency characteristics is the primary method used to assess ferrite material performance at a low magnetic flux amplitude. The complex permeability is expressed by its real (reactive) component μ' and imaginary (dissipative) component μ''. Material losses are conventionally modeled as the imaginary component of complex permeability. Some engineers prefer to use complex permeability to represent the losses of all types of magnetic cores [34]. In the thesis, the series equivalent circuit is assumed for all used complex symbols μ' and μ'' without the identification of the series, or parallel inductive circuit. Figure 18 shows the equivalent circuit for series representation of complex permeability as well as the vector diagram corresponding to the series circuit.

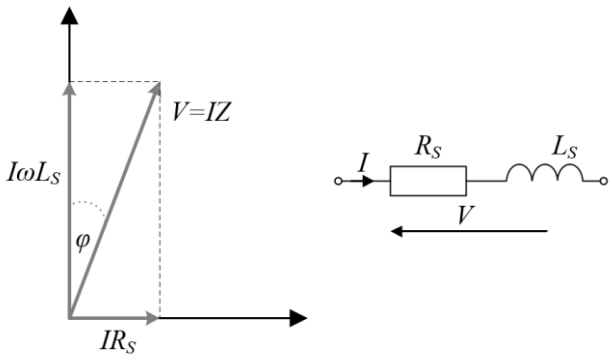


Figure 18. Equivalence of series inductive circuit.

The relation of the complex impedance is represented by the series model, based on complex permeability, in the following manner:

$$\bar{Z} = j\omega L_S + R_S = j\omega L_0 \,(\mu_s' - j\mu_s'') \tag{2.1}$$

$$L_S = L_0 \mu_s' \tag{2.2}$$

$$R_S = \omega L_0 \mu_s'' \tag{2.3}$$

$$tan\varphi = \frac{\mu_s''}{\mu_s'} \tag{2.4}$$

$$L_0 = \frac{\mu_0 N^2 A}{l} \tag{2.5}$$

where $\bar{Z}$ is the complex impedance, R_S and L_S are the series resistance and the series inductance, respectively, L_0 is the inductance of the core with unity permeability, ω is the angular frequency, j is the complex operator, μ' and μ'' are the real and imaginary

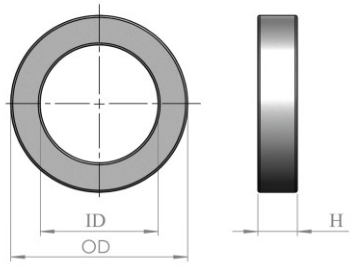
permeabilities in the series model, φ is loss angle (the phase angle between B and H), A is the core cross section, l is the magnetic path length in core and N is the turns number.

During the tests various core sizes are tested, therefore, a customised measurement fixture is required to measure complex permeability. The fixture features a cylindrical cup shape that forms a single turn equally distributed around the toroidal core specimen. The measurement method is based on a short-ended coaxial line and provides accurate results with a measurement range of up to 1 GHz [35],[36]. Measurements are performed by means of a Wayne Kerr 6550B analyzer [37].

2.1.1 Complex permeability physical sample size effect

The sample size selection plays an important role in magnetic material testing. The tested core sample may fall within the range of the electromagnetic wave's wavelength for the frequencies of interest; and thus, the developed dimensional resonance may dominate the measured core parameters [13]-[19]. As far as loss materials are concerned, the propagating electromagnetic wave is attenuated quickly and the measurements are dominated by the skin effect. In this section, the determination of the complex permeability is experimentally

TABLE 3. CORE PARAMETERS FOR COMPLEX PERMEABILITY MEASUREMENTS.

Core type	Core material	Dimensions OD x ID x H	Core cross section dimension	Core cross section	Core volume
Unit	-	mm	mm	mm²	cm³
T2	3C95	2 x 1 x 2	0.5 x 2	1.0	0.004
T6	3C95	6 x 4 x 2.8	1 x 2.5	2.8	0.043
T29	3C95	29 x 19 x 10	5 x 10	50	3.76
T50	3C95	50 x 30 x 19.5	10 x 19.5	195	24.50
T86	3C95	86 x 56 x 20	15 x 20	300	66.91
T152	3C95	152 x 104 x 24	24 x 24	576	231.62
					

investigated. In order to expose the core-size effect, an experiment was designed to validate a number of samples of various sizes as presented in Table 3.

Two custom cores were made, for the purpose of carrying out the experiments. The first core, of type T152, with an outer diameter of 152 mm, allows one to develop skin effect and dimensional resonance at a lower frequency. The second is core of type T2 and features an outer diameter of 2 mm. This is the smallest core which was manufactured for this study and was identified as free of any dimensional effects.

The calculated skin depths and half-wavelengths for the 3C95 material, as a function of frequency, are presented in Figure 19. The smallest cross-sectional dimensions for each tested core are indicated on the graph. The calculation is based on magnetic material parameters, experimentally measured, and presented at the end of the following section.

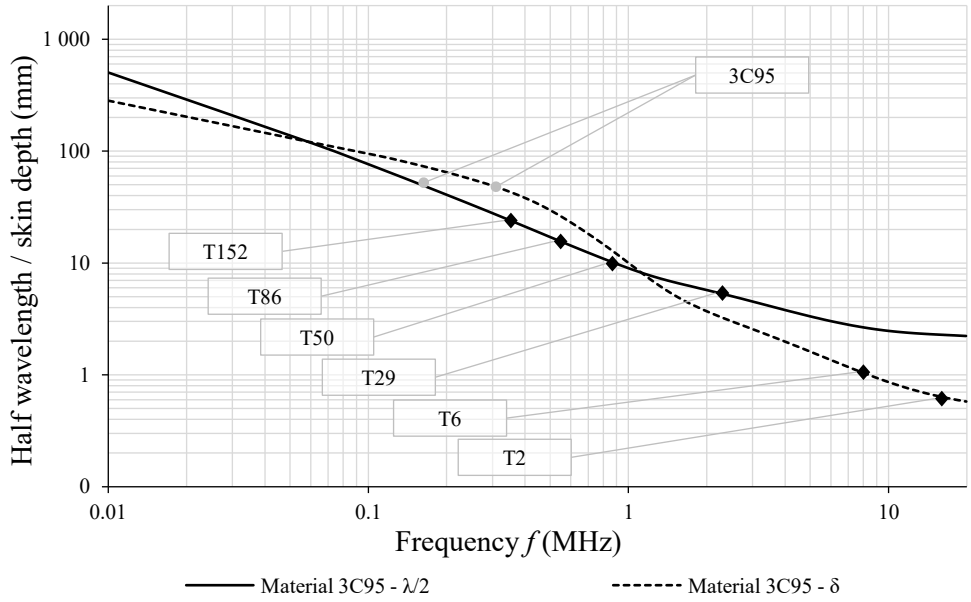


Figure 19. Electromagnetic wavelength and skin depth in 3C95 ferrite.

As shown in Figure 19, if the frequency during the measurement taking is higher than 336 kHz for the T152 core, 540 kHz for the T87 core, and 880 kHz for the T50, then the measured complex permeability shall be dominated by the dimensional resonance as the smallest cross-sectional dimension is equal to half a wavelength, while the skin depth proves insignificant. For the T29, the core dimensional resonance as well as skin effects may occur at the same time. The skin depth is lower than half a wavelength, however, the difference between both parameters remains small. Therefore, the T29 core attenuation may not be sufficient to supress the dimensional resonance. For the ring cores T6 and T2, there will be no dimensional resonance as these cores are too small, while at high frequency the core

parameters are dominated by skin depth caused by a combination of magnetic and electric losses.

As a next step, samples presented in Table 3 were tested. The measured real permeability as a function of frequency for various core sizes is shown in Figure 20, except for the T2 core whose measurement results are presented later in Figure 23. As can be seen, the largest core with an external diameter of approx. 152 mm is characterized by the highest permeability, at the lower frequency, followed by a sharp drop to zero at a frequency of approx. 500 kHz. The real permeability characteristic for the smallest core, with a diameter of 6 mm, slowly descends down to 0 at 20 MHz.

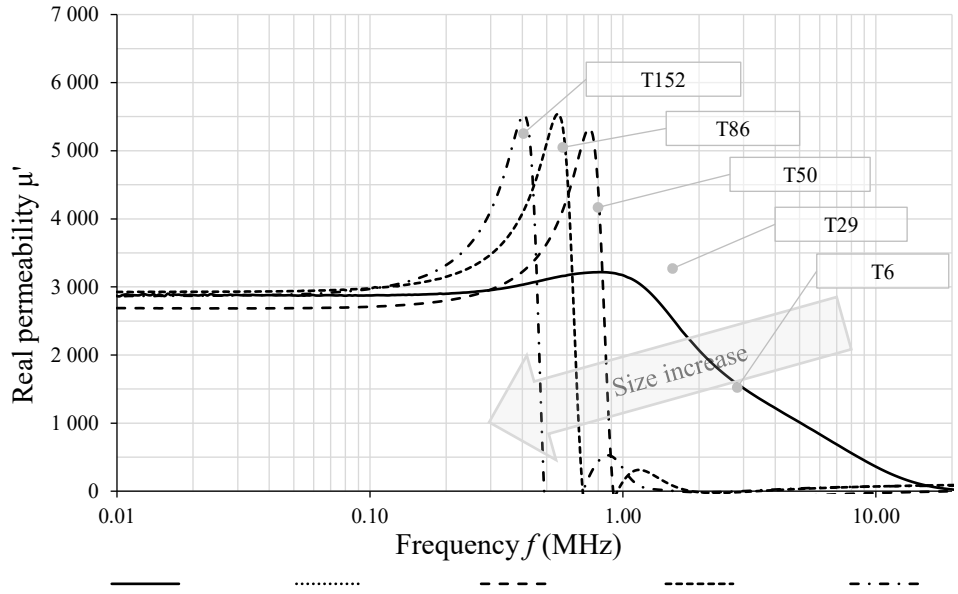


Figure 20. 3C95 ferrite real permeability vs. frequency.

The imaginary permeability as a function of frequency for the selected cores is shown in Figure 21.

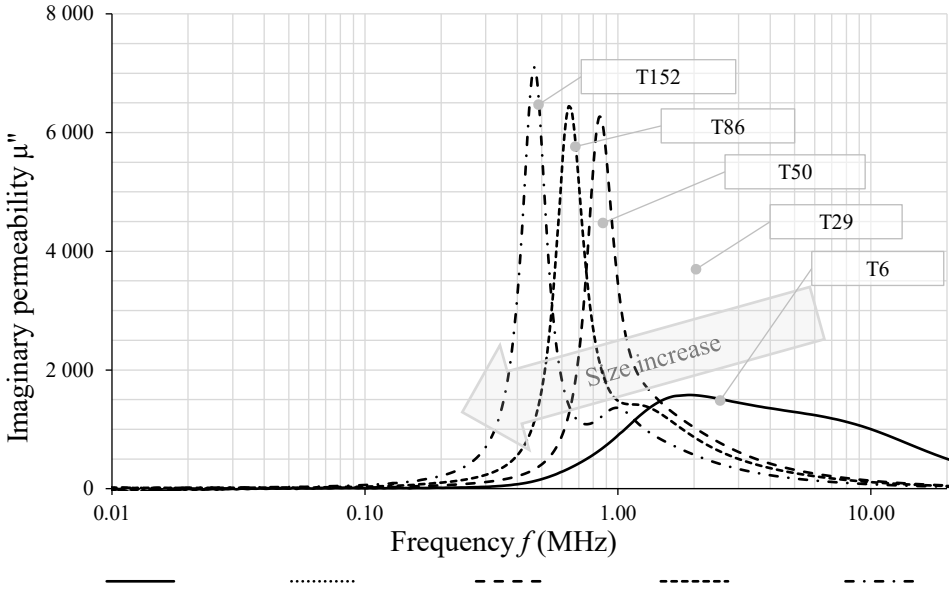


Figure 21. 3C95 ferrite imaginary permeability vs. frequency.

Similarly to real permeability shown in Figure 20, the largest core is affected by the earliest imaginary permeability peak of the highest magnitude at the frequency of approx. 500 kHz. The imaginary permeability characteristic for the T6 core decreases slowly and steadily from 1.8 MHz to 20 MHz, while at low frequencies of up to 1.8 MHz a gentle increase is visible.

The complex permeability characteristic for the two smallest cores is individually contrasted. T6 and T2 cores are presented in Figure 22, while the plots of real and imaginary permeability are shown in Figure 23.



Figure 22. T6 and T2 cores to test complex permeability characteristic.

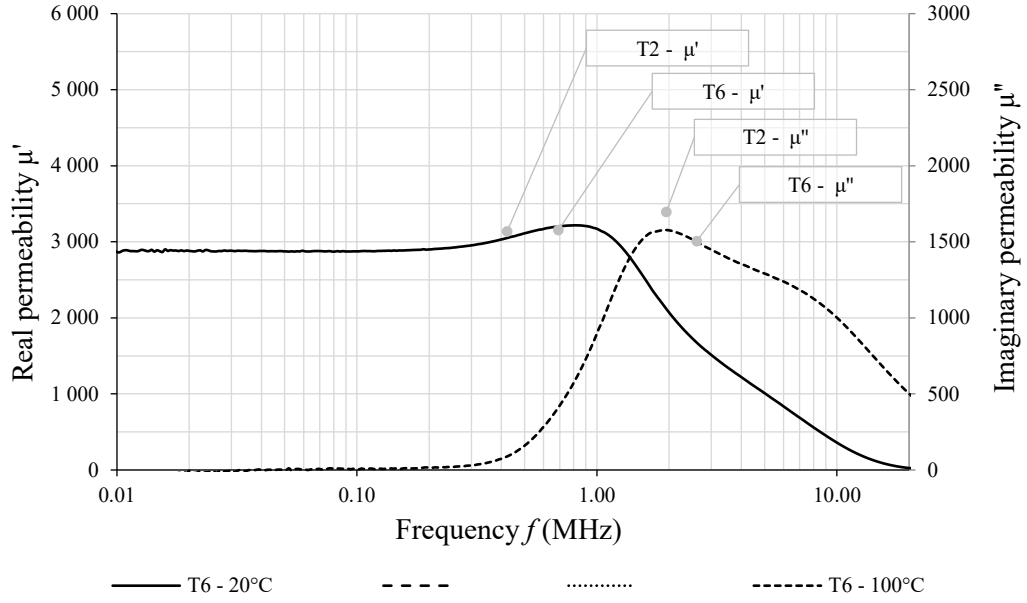


Figure 23. 3C95 ferrite complex permeability vs. frequency.

As shown in Figure 23, the measured real and imaginary permeability as a function of frequency for T6 and T2 cores are almost identical. For the T2 core, the real permeability drops slightly faster above 3 MHz. This is caused by higher losses, which is also visible as higher imaginary permeability. There are two main reasons as to why this difference is visible. The first is that the T2 core was machined out of a bigger ferrite block, in contrast to the T6 core which was pressed and sintered. Therefore, the core was subjected to high mechanical stress during machining, which may have resulted in unavoidable variations of material properties. The second reason could be that the measured parameters are very small, and hence an additional error from the device could have affected the measured parameters.

The dimensions of the tested Mn-Zn ferrites affect the measured core permeability characteristic; therefore, the selected core should have the smallest dimensions possible. On the other hand, the small core dimensions directly translate to small values of measured resistance and reactance. The toroidal core T6/4/2.8 mm has been selected as the core which provides the material data with the highest possible accuracy as it comes from the press and sintering process without additional machining that may affect material parameters. In order to define the complex permeability of the T6 core, a dedicated test fixture was also developed, as presented in Figure 23. The test fixture provides one turn equally distributed around the tested core without any mechanical stress and a reliable connection to measurement device via a concentric cable. The test fixture may be easy duplicated as it is built with off-the-shelf parts. Therefore, the material complex permeability characteristic for the T6 core, made of various materials, could be easily reproduced.

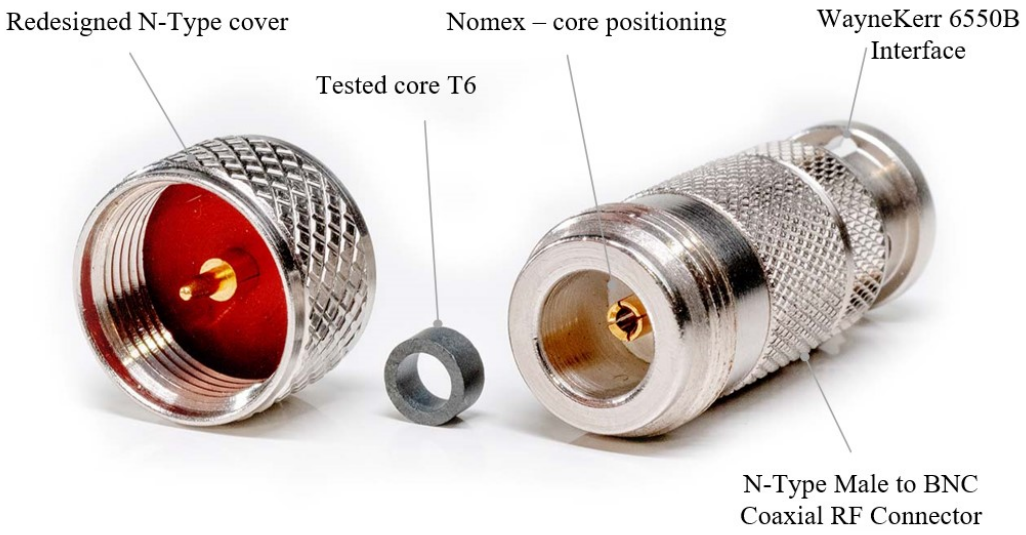


Figure 24. Short-ended coaxial line to measure the permeability characteristic.

Additionally, the complex permeability vs. frequency characteristics for various core sizes made of 3F36, 3E65 and 3E10 ferrite material are shown in Figure 25, Figure 26, and Figure 27, respectively.

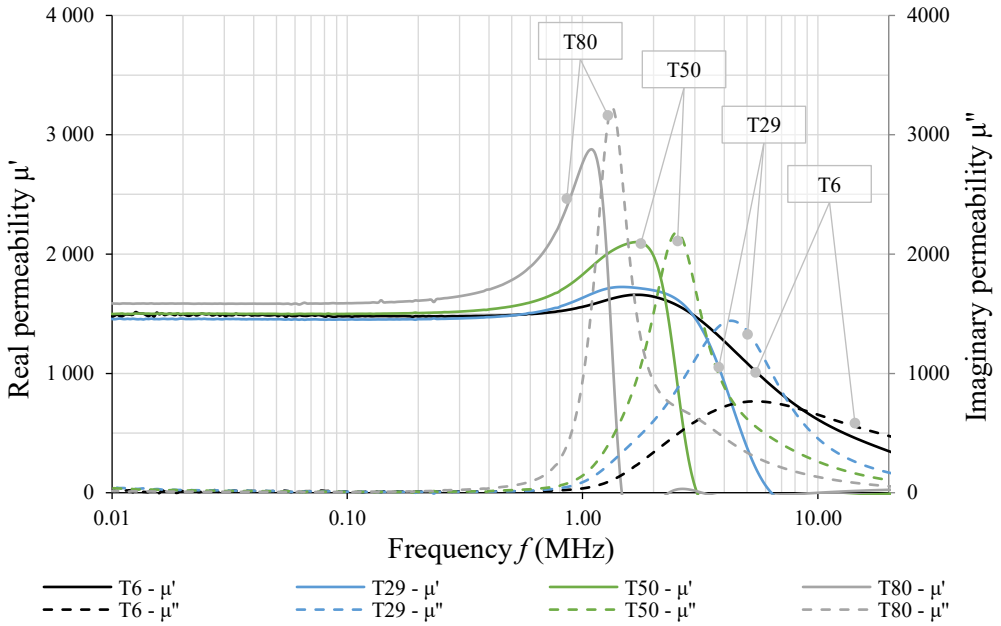


Figure 25. 3F36 ferrite complex permeability vs. frequency.

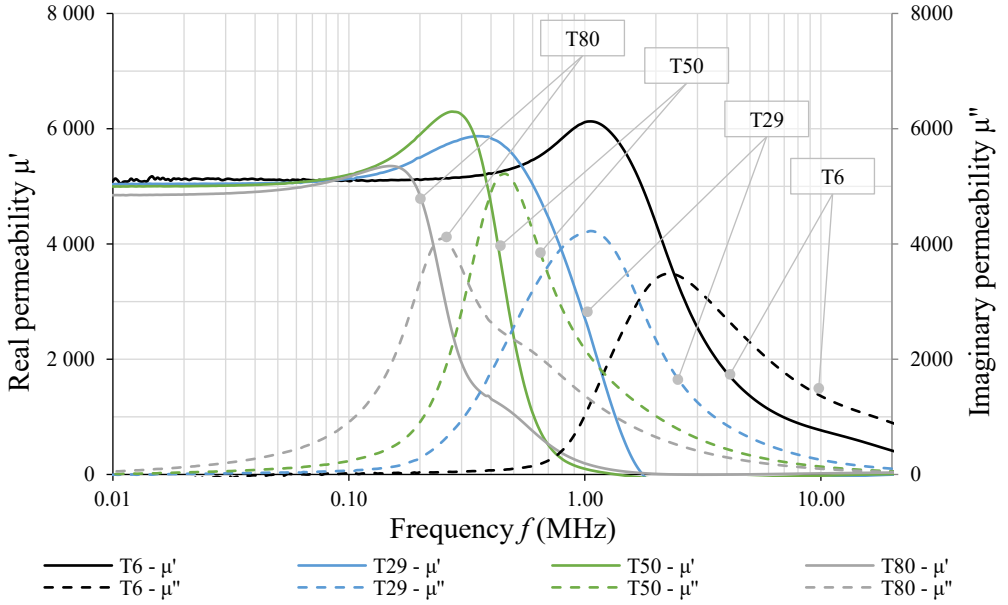


Figure 26. 3E65 ferrite complex permeability vs. frequency.

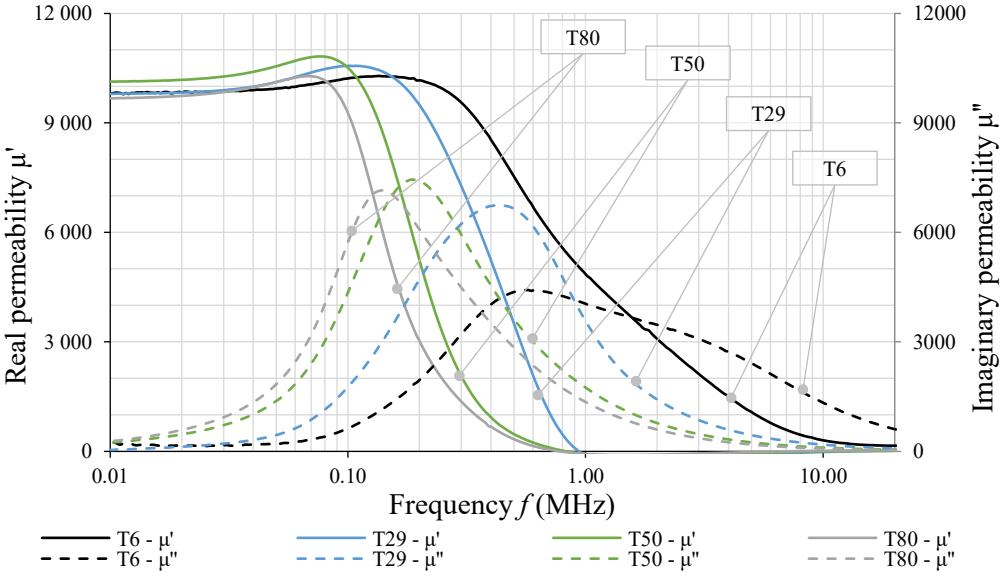


Figure 27. 3E10 ferrite complex permeability vs. frequency.

In all the tested Mn-Zn materials, the dimensions of the tested samples impact the measured complex permeability. A proper quality design of magnetic components for high-frequency applications requires detailed information on the magnetic materials. Tests show that permeability greatly depends on physical size. The magnetic material complex permeability is strongly affected by the high frequency effects associated with sample size increases. Therefore, the smallest cores provide the material data with the highest possible accuracy for further calculations.

Appendix A contains experimentally measured complex permeability characteristics for Mn-Zn ferrites: 3E10, 3F36, 3E65 and 3C95, provided in table format.

2.1.2 Complex permeability temperature effect

Magnetic properties of soft ferrites are sensitive to temperature. In general, the higher the material permeability, the lower the Curie temperature. The Curie temperature is the temperature above which thermal agitation overcomes the alignments of magnetic moments and causes the material to become paramagnetic. In most Mn-Zn ferrite materials, the permeability increases with rising temperature up to its peak value just below the Curie point, and then decreases to its function limit at μ_0, above the Curie temperature. The temperature's effect on the complex permeability is shown in Figure 28 and Figure 29 for the 3C95 T6 and T152 cores. During the measurements of complex permeability at higher temperatures, it is necessary to control the time to reach the steady-state temperature throughout the ferrite sample. If this is ignored, the temperature gradient within the sample will have a substantial effect on the measurements, rendering them unreliable. The temperature during the measurements of complex permeability was controlled with a thermal chamber.

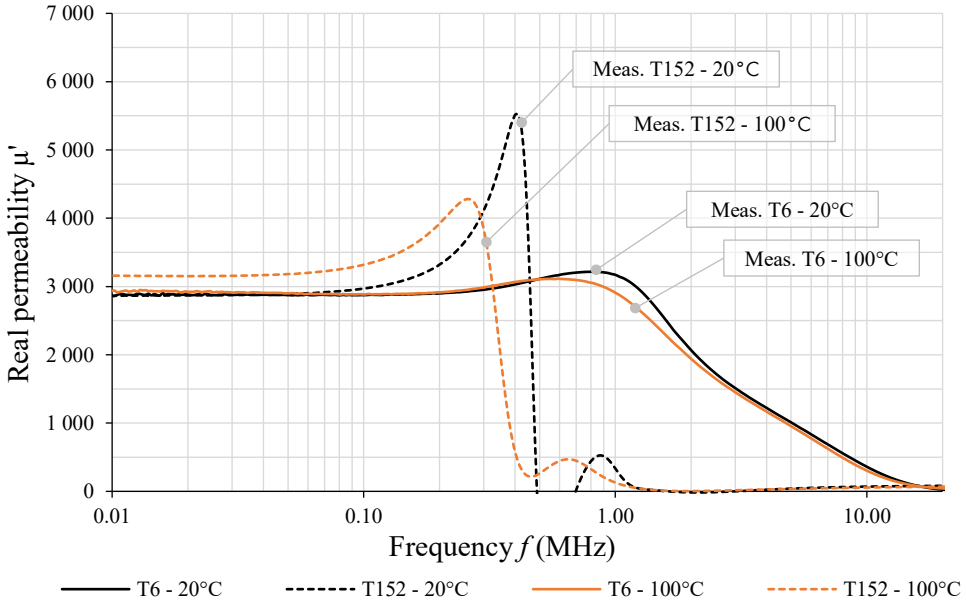


Figure 28. 3C95 ferrite real permeability vs. frequency and temperature.

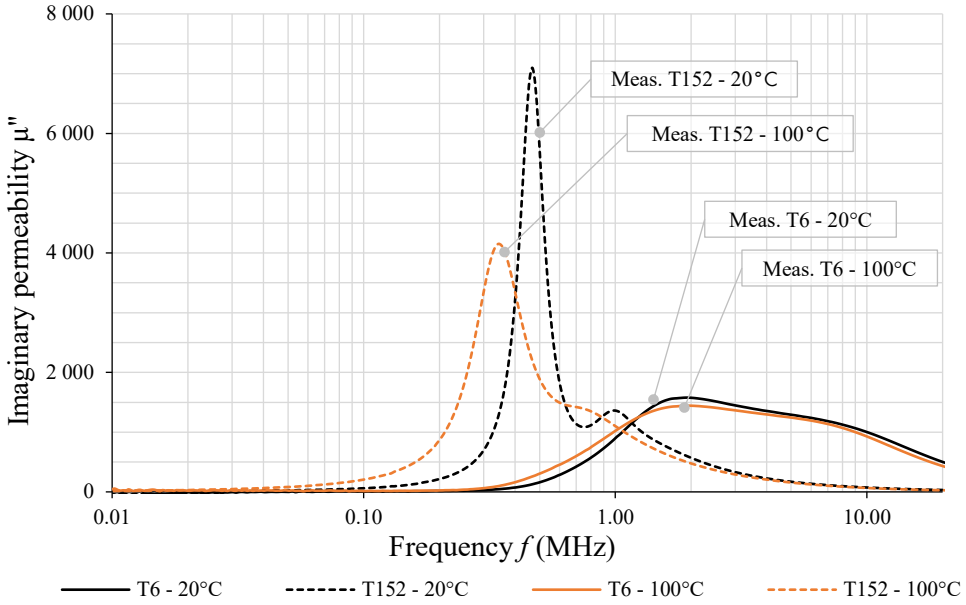


Figure 29. 3C95 ferrite imaginary permeability vs. frequency and temperature.

As shown in the complex permeability plots, the large ferrite sample show a high temperature dependency. At a temperature of 100 °C, the real permeability peak decreases from 400 kHz down to 250 kHz. Small samples are less susceptible, rendering the temperature effect negligible.

Ferrite manufacturers are able to control the permeability change according to the temperature or achieve the desired permeability for a particular temperature range. This can be achieved through the controlling of the oxygen partial pressure during the ferrite sintering process. As a result, the permeability temperature characteristic exhibits a secondary maximum, which can be placed at any temperature below the Curie Point. Most of the Mn-Zn ferrites are designed to feature almost the exact permeability at 25 °C, and around 100 °C, which is the typical operating temperature for the magnetic components based on the ferrite. However, in case of special requirements ferrite manufactures are able to control the permeability change according to the temperature in any way.

Finally, the complex permeability frequency characteristic for two temperatures, for various core sizes and materials, are shown from Figure 30 to Figure 32. The characteristics are presented for T6 and T80 cores made of 3F36, 3E65 and 3E10.

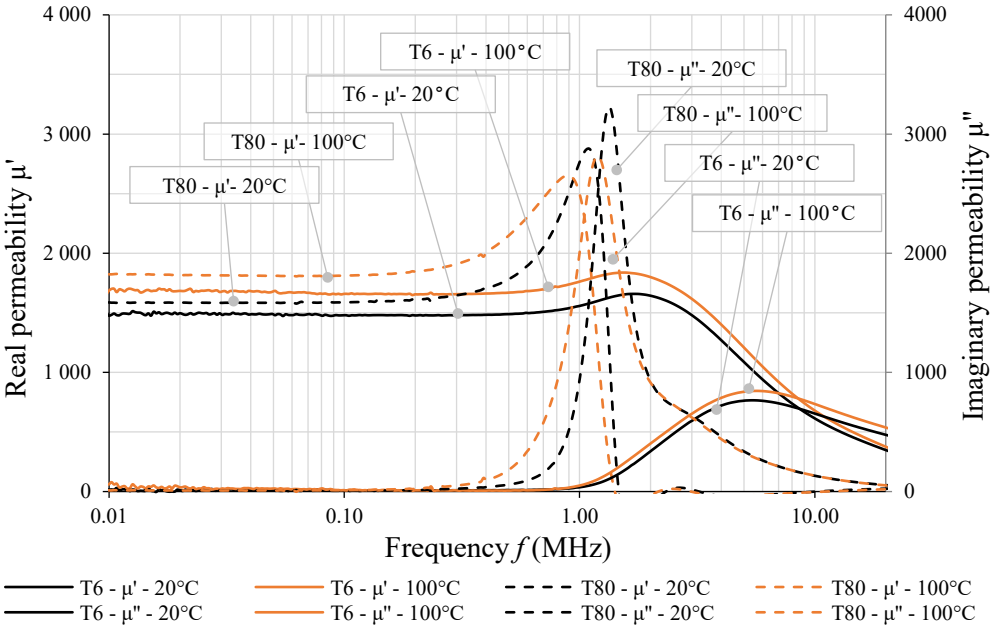


Figure 30. 3F36 ferrite complex permeability vs. frequency and temperature.

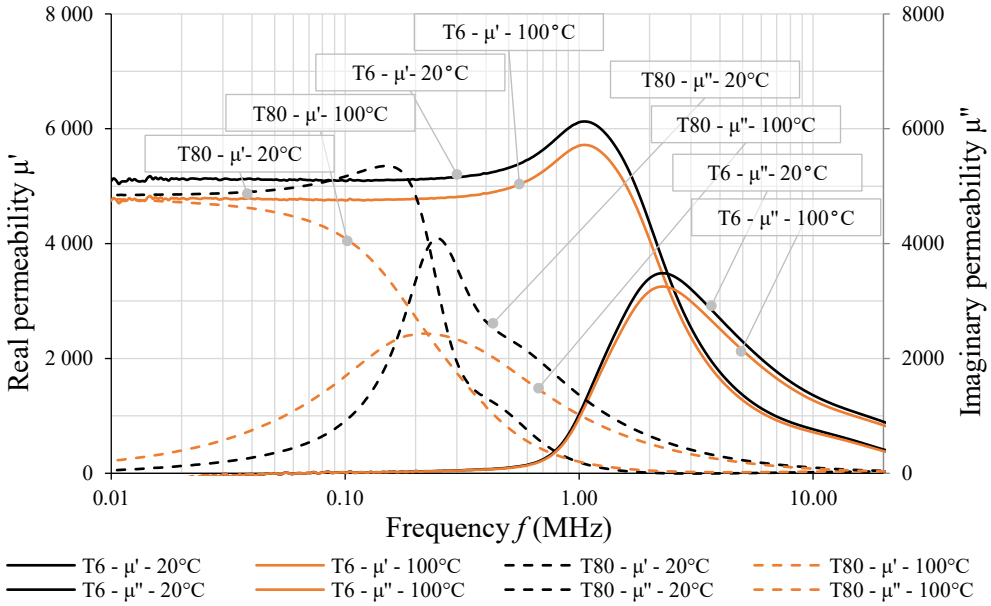


Figure 31. 3E65 ferrite complex permeability vs. frequency and temperature.

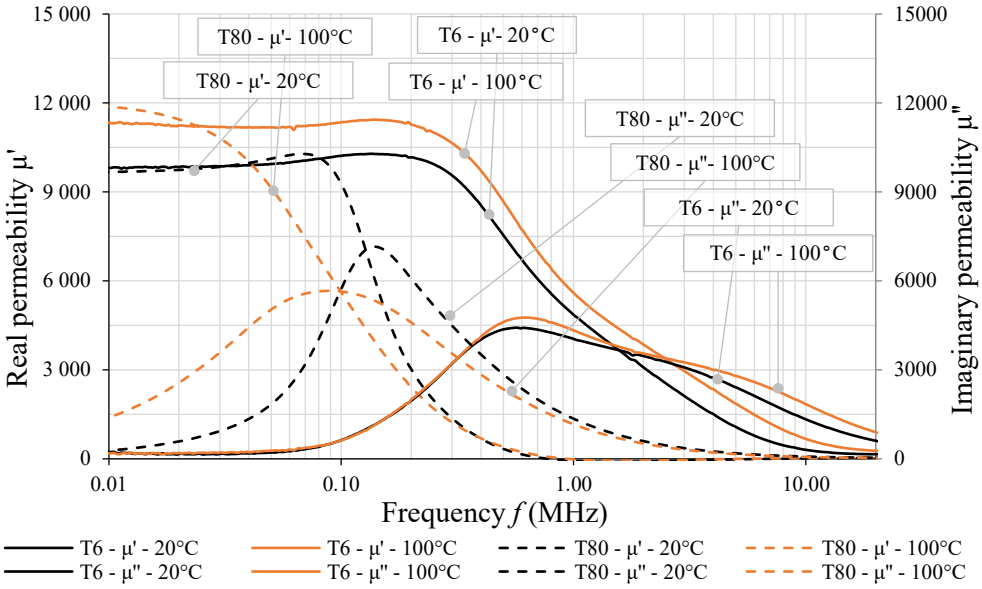


Figure 32. 3E10 ferrite complex permeability vs. frequency and temperature.

2.1.3 Complex permeability force effect

The magnetic core is prone to mechanical stress. Ferrite cores are especially sensitive to mechanical stress of various origins. Surface stress is present in some ferrite cores as surface grinding is necessary to achieve the required dimensions or to provide the required surface finishing. Compression force may be applied due to core clamping, or winding with a high gauge magnet wire directly on the core. Thermal expansion is also an important factor as it may both compress and expand the core. High permeability materials have a small total anisotropy: therefore, stress anisotropy is an important element of the total anisotropy. In ferrite materials the magnetocrystalline anisotropy is minimized; therefore, the anisotropy as a result of stress may have the dominant role. When a large mechanical force is applied to the ferrite core, the stress anisotropy acts against the magnetization. In consequence, changes in the externally applied stress might generate major changes in permeability [34],[38]. In order to measure the effect of stress on the ferrite permeability, an additional fixture was built, as shown in Figure 33. The permeability measurement was performed on a ring core with an external diameter of 50 mm, an inner diameter of 30 mm, and a height of 19.5 mm with only one turn.

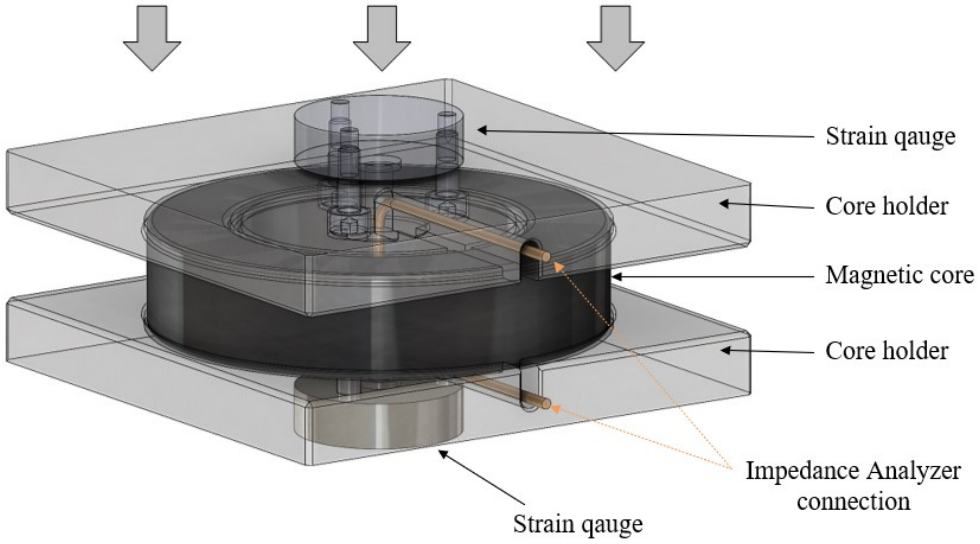


Figure 33. Measurement setup for testing impact of mechanical stress on magnetic permeability.

The impact of the mechanical stress on ferrite material permeability for six MnZn samples is shown in Figure 34. All the tested ferrite materials: (3C95, 3E65, 4S60, 3F36, 3E15 and 3E10) have negative bulk magnetostriction; therefore, whenever small stresses are applied, the permeability rises and then decreases together with increasing force. Measurements are performed with a Wayne Kerr 6550B analyzer at 10 kHz.

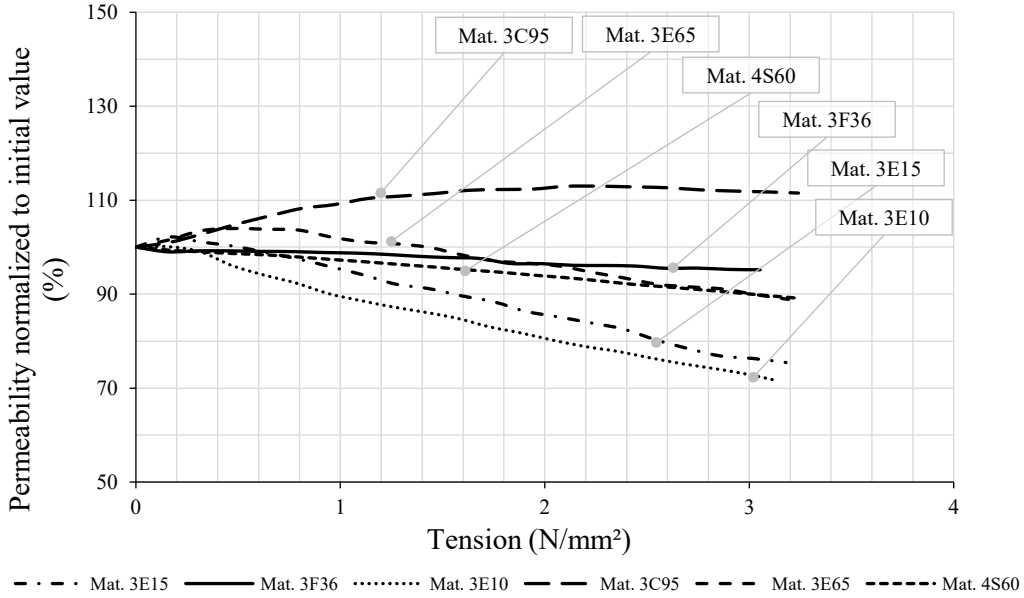


Figure 34. MnZn ferrite permeability change vs. mechanical pressure based on the experimental data.

As a next step, mechanical stress effect on complex frequency characteristic for three different T29 cores, made of 3F36, 3E65 and 3E10 ferrite, were tested and the results are shown from Figure 35 to Figure 37. As show in the figures, the complex permeability is mechanical-stress dependent. The higher the stress, the more significant the real and imaginary permeability drop. Material with the lowest permeability, such as 3F36, show the lowest stress dependence, while the high permeability materials, such as the 3E10, exhibit the highest.

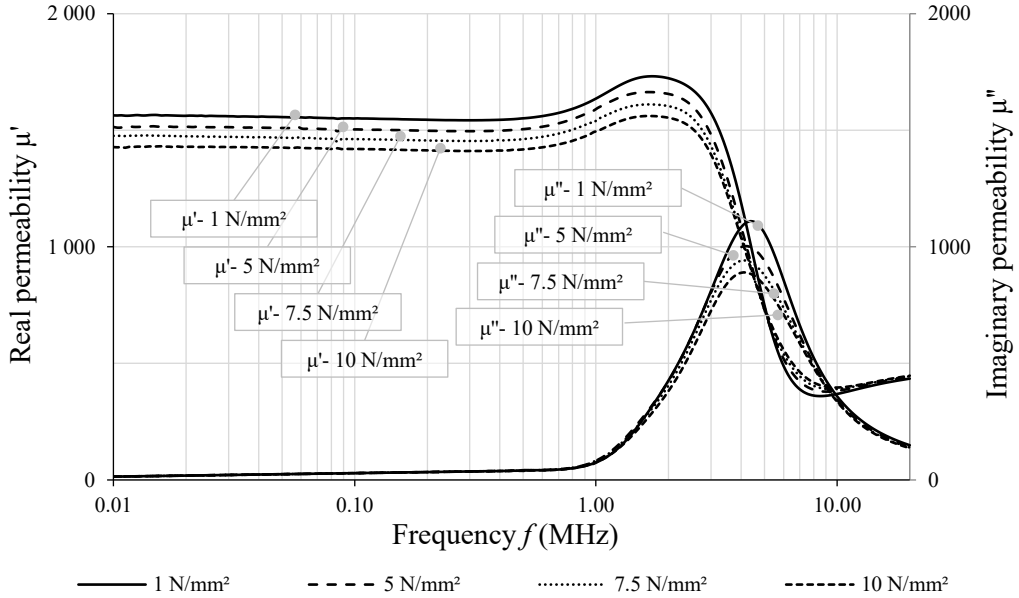


Figure 35. 3F36 ferrite complex permeability vs. mechanical pressure.

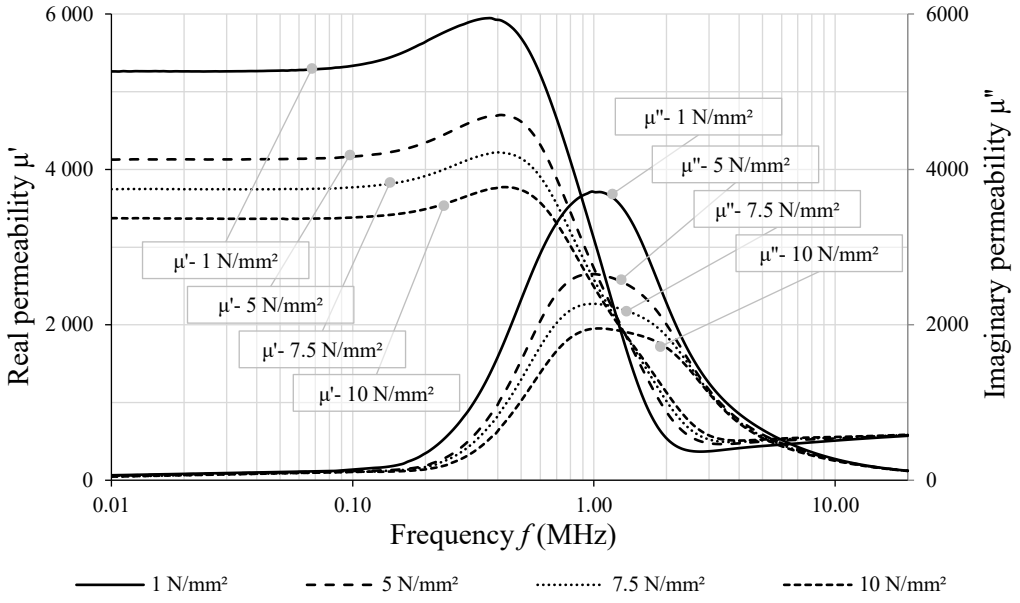


Figure 36. 3E65 ferrite complex permeability vs. mechanical pressure.

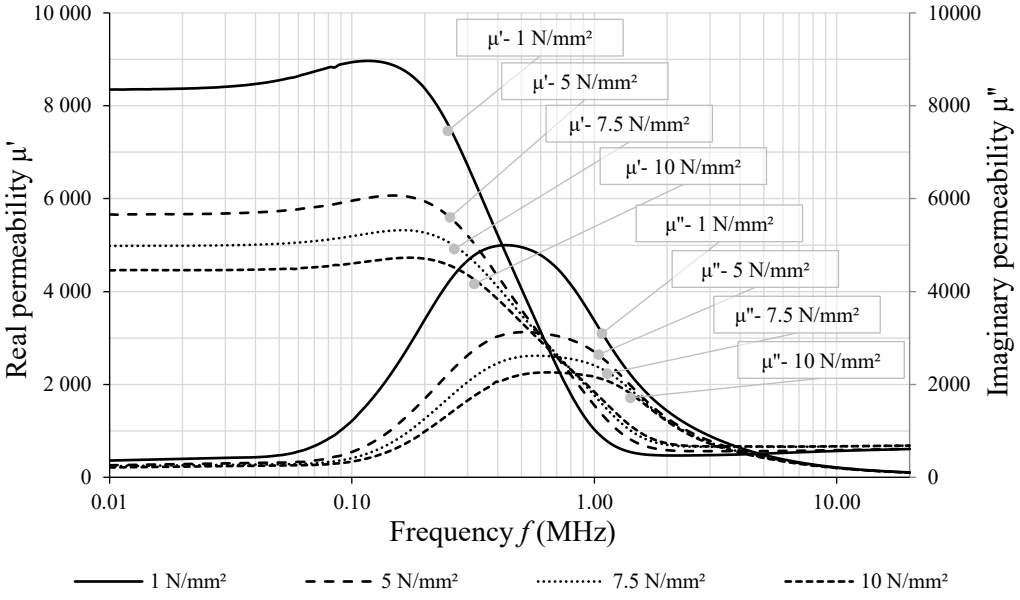


Figure 37. 3E10 ferrite complex permeability vs. mechanical pressure.

2.2 Complex permittivity characteristic

Complex permittivity, as in the case of complex permeability, is the second parameter which should be taken into account during the magnetic material selection process. The combination of the high permeability and the high permittivity of MnZn ferrite affects the core high-frequency performance due to the skin effect and dimensional resonance. Therefore, accurate identification of the magnetic material complex permittivity is essential to provide high quality physical phenomena modelling and to improve the EMI filter design process.

Complex permittivity describes the material interaction with an electric field. The real part of permittivity ε' defines how much energy from an external electric field is stored in a material [34]. The imaginary part of permittivity ε'' is called the 'loss factor', and it describes how dissipative or lossy the material is in the presence of an external electric field. In the thesis, the parallel equivalent circuit is assumed for all used complex symbols ε' and ε'' without the identification of the series or parallel inductive circuit. Figure 38 shows an equivalent circuit for parallel representation of the complex permittivity, as well as a vector diagram corresponding to a parallel circuit.

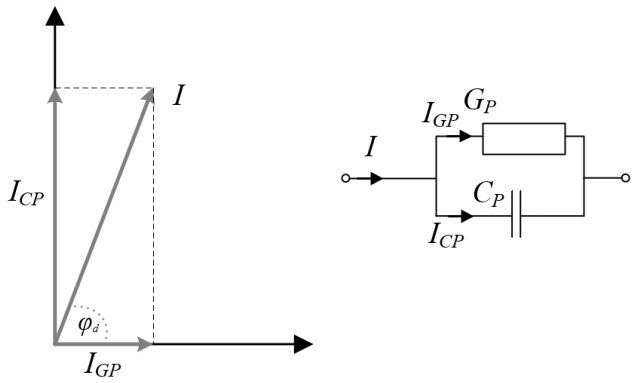


Figure 38. Equivalence of parallel capacitive circuit [34].

The complex admittance can be represented by a parallel model based on complex permittivity in the following manner:

$$\bar{Y} = j\omega C_P + G_P = j\omega\varepsilon_0 \frac{A}{d}(\varepsilon_P' - j\varepsilon_P'') \tag{2.6}$$

$$\varepsilon_P' = \frac{C_P d}{\varepsilon_0 A} \tag{2.7}$$

$$\varepsilon_P'' = \frac{G_P d}{\omega\varepsilon_0 A} = \frac{\sigma}{\omega\varepsilon_0} \tag{2.8}$$

$$tan\delta_d = \frac{\varepsilon_P''}{\varepsilon_P'} \tag{2.9}$$

where G_P is the measured conductance, C_P is the measured capacitance, ε_P' is the real component of the parallel relative complex permittivity, ε_P'' is the imaginary component of the parallel relative complex permittivity, ε_0 is the vacuum permittivity, d is the tested sample thickness, A is the test sample cross section, σ is the material conductivity, and $tan\delta_d$ is the dielectric loss tangent.

2.2.1 Complex permittivity test setup

The choice of the permittivity measurement techniques depend on many factors, such as the frequency, the expected value of complex permittivity, the tested material properties (homogeneous, isotropic) and the form (liquid, powder, solid), as well as the sample size and temperature. Figure 39 presents a summary of the available measurement techniques with reference to frequency and loss [39],[40].

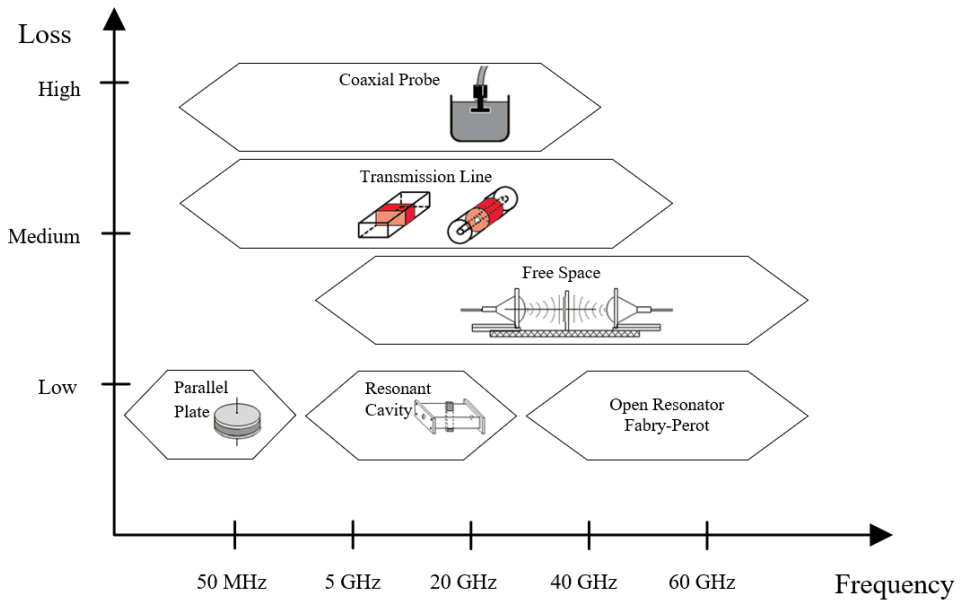


Figure 39. Summary of measurements techniques for material dielectric properties.

As the materials are low loss the most suitable measurement technique for defining the complex permittivity of Mn-Zn ferrites is the parallel-plate method. This method uses a parallel-plate capacitor as a sample holder, with the tested material in between. The material is subjected to an AC source, while the actual voltage and current across the material is monitored by an LCR analyzer. As a result, the tested material parameters are derived by knowing the dimensions of the tested samples and by measuring its capacitance and dissipation

factor. In order to define the ferrite electrical characteristics based on the parallel plate method, a dedicated test fixture was developed as presented in Figure 40 [41]-[42]. The test fixture has four exchangeable sets of electrodes that can be used for measuring custom shaped samples: three electrodes for testing round cross-section samples with diameters 10 mm, 2.4 mm and 1.0 mm, and one electrode for testing rectangular cross-section samples with dimensions of 2.8 and 10 mm. Each electrode is shielded to minimize the effect of fringing fields. Figure 41 shows the electrodes and ferrite samples used for measuring the complex permittivity of Mn-Zn ferrites.

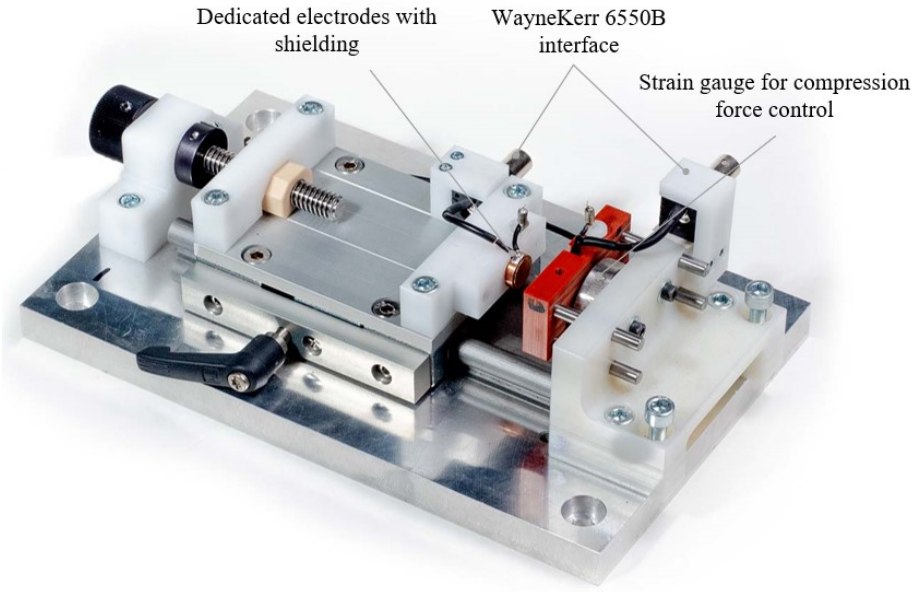


Figure 40. Measurement fixture to define ferrite permittivity characteristic.

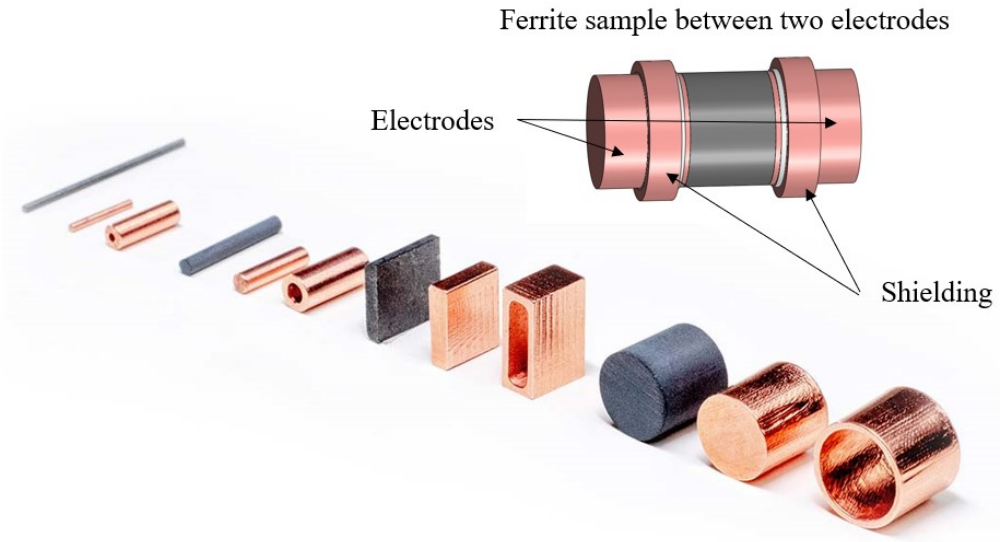


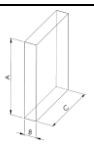
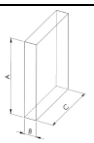
Figure 41. Electrodes and tested ferrite samples.

The test fixture is also equipped with strain gauges to control the ferrite stress during measurements. The permittivity characteristics are measured using a Wayne Kerr 6550B analyzer up to 20 MHz. During the test, a sample is placed between the copper electrodes to measure its admittance. All tested ferrite samples have metalized contact surfaces to minimize contact resistance. Before metallization, test surfaces had been polished, and finally thin layers of the graphite paint were applied on test surfaces. Open, short and load compensation of the test fixture is performed before each test. For the short compensation, both electrodes are shortened by closing the fixture so that both electrodes are in contact. During the open compensation, the test fixture is loaded with a plastic dummy whose length corresponds to the tested ferrite length. During the load compensation, the fixture is loaded with a 50 Ω resistor and a 100 pF capacitor.

2.2.2 Complex permittivity physical sample size effect

As with the measurements of complex permeability, physical sample size plays an important role in the complex permittivity measurements. The size of the tested sample could be within the range of the electromagnetic wave wavelength for the frequencies of interest. Thus, the developed dimensional resonance may dominate the measured core parameters. Eight samples were prepared to demonstrate the influence of sample size on the complex permittivity characteristics. The sample details are presented in Table 4. Samples differ from one another in their cross-sectional dimensions, which directly affect the dimension resonance.

TABLE 4. CORE PARAMETERS FOR COMPLEX PERMITTIVITY MEASUREMENTS.

Core type	Core material	Shape	Dimensions	Core cross section dimension	Core cross section	Core volume
Unit	-	-	mm	mm	mm^2	mm^3
Sample 1	3C95 Batch 1		10 x 3.0	10	78.5	235
Sample 2	3C95 Batch 1		10 x 6.0	10	78.5	471
Sample 3	3C95 Batch 1		10 x 12	10	78.5	942
Sample 4	3C95 Batch 2		10 x 12	10	78.5	942
Sample 5	3C95 Batch 1		10 x 2.8 x 10	10 x 2.8	28	280
Sample 6	3C95 Batch 2		10 x 2.8 x 10	10 x 2.8	28	280
Sample 7	3C95 Batch 1		2.4 x 24	2.4	4.52	108
Sample 8	3C95 Batch 1		1.0 x 24	1.0	0.78	18.8

The calculated half-wavelength for the 3C95 material as a function of frequency is presented in Figure 42. Additionally, the smallest cross-sectional dimension of each tested sample is indicated on the graph. The dimensional resonance is visible in Sample 1-4 at 900 kHz, in Sample 5-6 at 8 MHz, in Sample 7 at 15 MHz, while for Sample 8 this frequency is beyond 20 MHz.

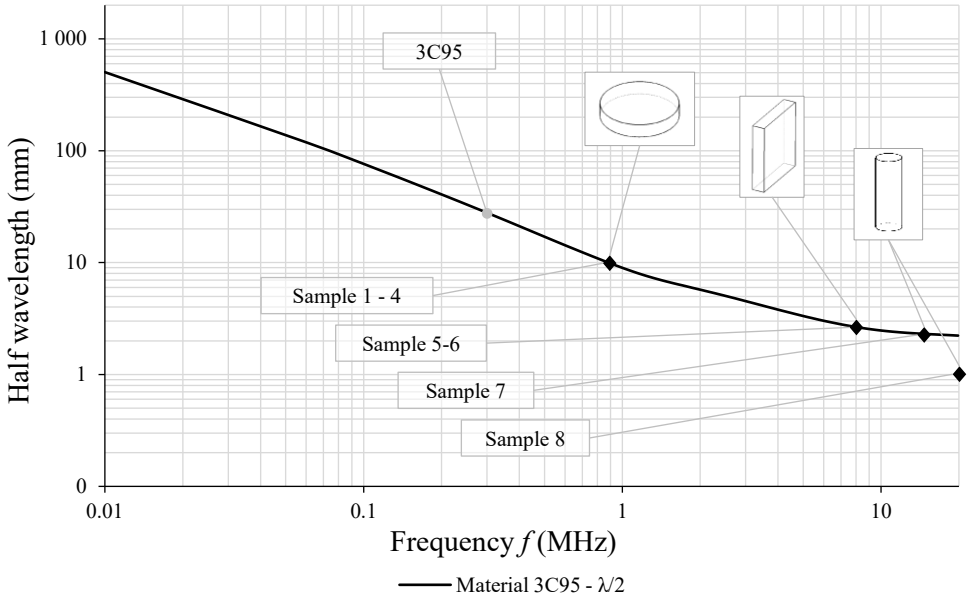


Figure 42. Calculated half wavelength in 3C95 ferrite.

As a next step, the samples presented in Table 4 were tested in the developed test fixture. The electrical properties of the tested samples were extracted from the admittance. Plots of real and imaginary permittivity for the tested samples as a function of frequency are shown in Figure 43 and Figure 44, respectively. For the tested discs, samples 1 to 4, with a diameter of 10 mm, the real permittivity drops sharply at 1.5 MHz. The dimensional effect for those samples is also visible in the imaginary permittivity characteristic at 900 kHz, as it starts to increase. The sample height, in the direction of the applied E field, has little effect on the measured complex permittivity. As for the tested samples, if the smallest cross-section decreases, the dimensional resonance frequency increases. For sample 8, as the smallest rod core that could possibly be manufactured, the real permittivity decreases gradually with frequency. However, the imaginary part shows a slow growth above 10 MHz, which suggests that dimensional resonance will occur at higher frequencies. Two sets of samples, sample 3 and 4 as well as sample 5 and 6, were made of two different batches of the 3C95 material. For those samples, there is almost no difference in the complex permittivity characteristic.

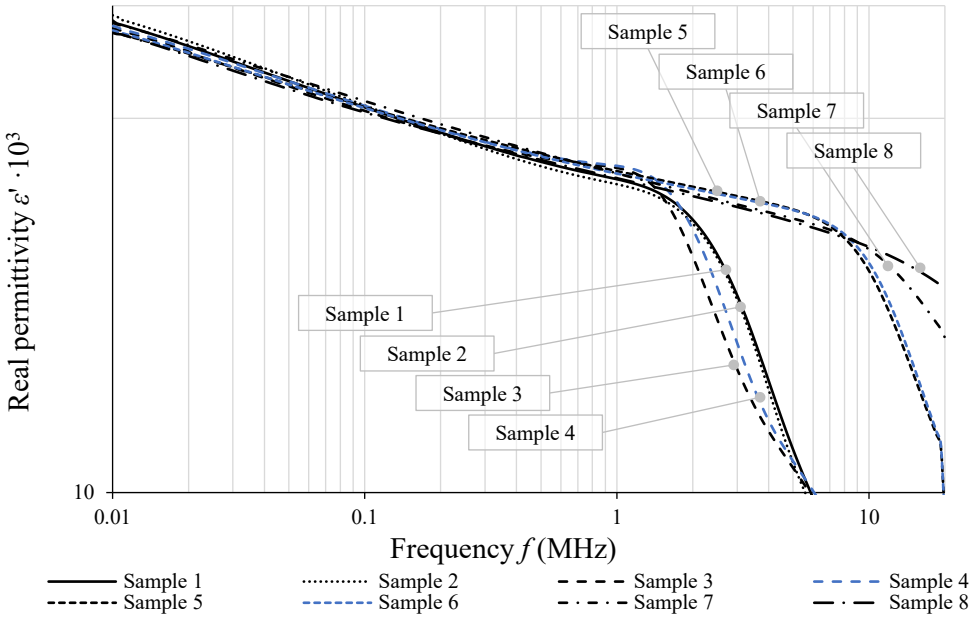


Figure 43. 3C95 ferrite real permittivity vs. frequency.

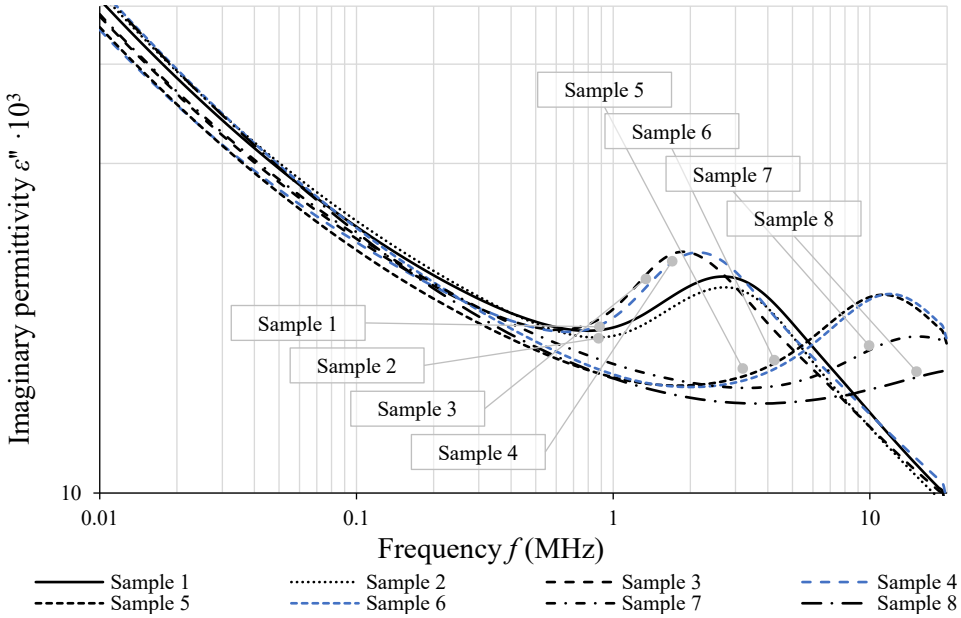


Figure 44. 3C95 ferrite real permittivity vs. frequency.

As illustrated in both plots, the high-frequency effects are visible in the tested samples, while the difference in the measured complex permittivity for high frequencies is the result of the dimensional resonance developed due to the sample size. Samples with the smallest cross sectional dimension should be selected to measure the complex permittivity characteristics. However, attention must be paid during core size selection to both core cross-section dimensions. The core surfaces were polished before the metallization; however, this does not eliminate the probability that some small air gaps may have formed between the electrodes

and sample. These air gaps can be a significant source of error as they could create additional capacitors in series to the tested samples. Core samples with a small cross section help to minimalize these effects, as high capacitance is achieved by a large plate area.

2.2.3 Data extrapolation at higher frequencies

There are technical limitations to producing core samples of extremely small dimensions. The manufacturing of small rod cores is not possible for all ferrite materials as compression forces during the forming process are much smaller than for toroidal cores. As presented in the previous section, sample 8 is the smallest rod core that could be manufactured out of 3C95 material. Despite that, the dimensional resonance is still noticeable above 10 MHz. The dimensional resonance in magnetic materials with higher permeability and permittivity may occur at lower frequency; therefore, getting reliable material data up to 10 MHz may not be possible. On the other hand, core modeling requires reliable material data in the frequency range from 150 kHz to 30 MHz, which is the usual frequency range for the conducted emissions. For this reason, a measurement extrapolation was used to obtain high quality material data at higher frequencies. The dimensional-resonance effect can be eliminated by using an equivalent circuit to extrapolate the measurements. The equivalent circuit assumes that the parameters extracted out of the sample are examined at a frequency where dynamic effects are not present and allow the modeling of fundamental core behavior regardless of its size and operating frequency. The state-of-the art literature provides two equivalent circuit models for ferrite modelling. The first equivalent circuit is a combination of parallel *RC* pairs connected in series to represent a ferrite granular structure. It is also recognized that this model shows good accuracy in the limited frequency range from 5 kHz to 80 kHz. As a result, the second equivalent circuit model was proposed based on constant phase elements (CPE) that replace capacitances in the first equivalent circuit model [43]. The equivalent circuit is a parallel network of resistance and CPE pairs connected in series to represent the ferrite granular structure. The CPE is advantageous for modelling an imperfect capacitance, where the effective capacitance and resistance decrease as frequency increases. The CPE element is characterized by two parameters: Q and n, for $n = 1$, the CPE corresponds to a pure capacitor. The 2-stage equivalent circuit of a MnZn ferrite with CPE is shown in Figure 45.

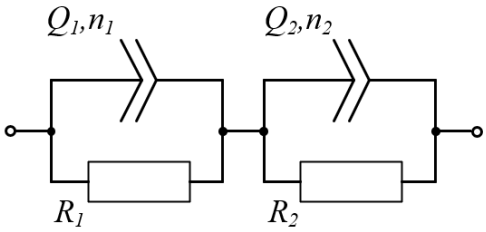


Figure 45. Equivalent electrical circuit of a MnZn ferrite based on constant phase element [43].

The complex impedance of the proposed equivalent circuit and its real and imaginary components are as follows [44]:

$$Z(\omega) = \frac{R_1}{1 + (j\omega)^{n_1} Q_1 R_1} + \frac{R_2}{1 + (j\omega)^{n_2} Q_2 R_2} \tag{2.10}$$

$$Re\ Z(\omega) = \frac{R_1(1 + \omega^{n_1}\cos(\frac{\pi n_1}{2})Q_1 R_1)}{1 + \omega^{n_1} Q_1 R_1 (2\cos\left(\frac{\pi n_1}{2}\right) + \omega^{n_1} Q_1 R_1)} + \frac{R_2(1 + \omega^{n_2}\cos(\frac{\pi n_2}{2})Q_2 R_2)}{1 + \omega^{n_2} Q_2 R_2 (2\cos\left(\frac{\pi n_2}{2}\right) + \omega^{n_2} Q_2 R_2)} \tag{2.11}$$

$$Im\ Z(\omega) = -\frac{\omega^{n_1} R_1 sin\left(\frac{\pi n_1}{2}\right) Q_1 R_1}{1 + \omega^{n_1} Q_1 R_1 \left(2\cos\left(\frac{\pi n_1}{2}\right) + \omega^{n_1} Q_1 R_1\right)} - \frac{\omega^{n_2} R_2 sin\left(\frac{\pi n_2}{2}\right) Q_2 R_2}{1 + \omega^{n_2} Q_2 R_2 (2\cos\left(\frac{\pi n_2}{2}\right) + \omega^{n_2} Q_2 R_2)} \tag{2.12}$$

The EIS Spectrum analyzer software was used to determine equivalent model parameters based on the measured core characteristics [44]. The extrapolation accuracy depends on the last point used in the curve fitting. The selected point shall not be affected by high-frequency effects, such as eddy currents and dimensional resonance. As a general rule, the selected point is determined by the change of function monotony in the plane of imaginary vs. real permittivity. Then, the obtained equivalent model will give the natural material characteristic without core size effects. Real and imaginary permittivity frequency characteristics based on the CPE equivalent model are shown in Figure 46 and Figure 47, respectively. Measured data from Sample 5 and Sample 7 may be used for high frequency extrapolation with the same result. The equivalent circuit parameters for 3C95 ferrite are presented in Table 5.

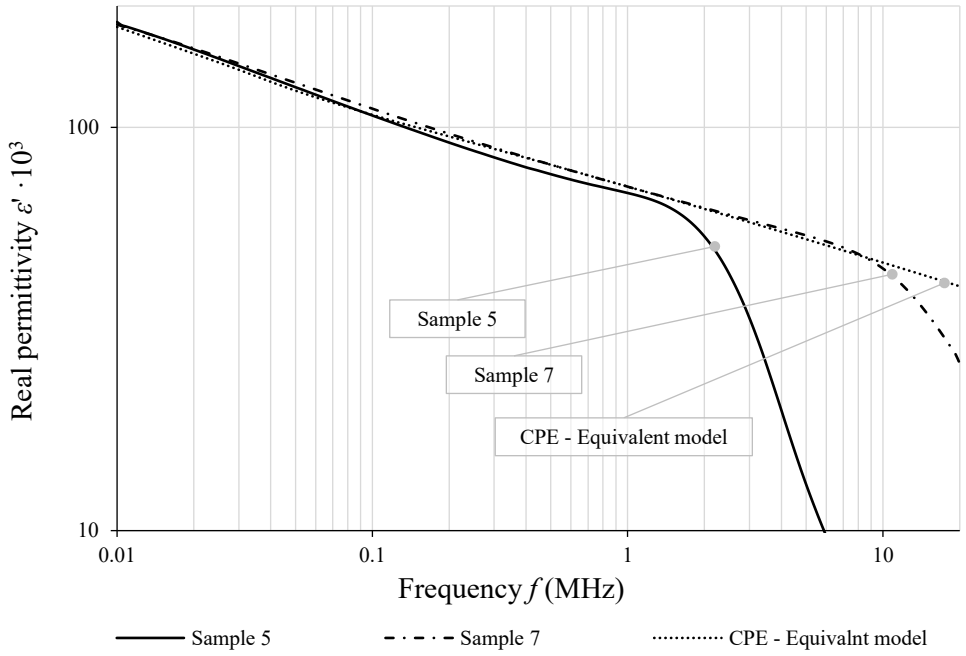


Figure 46. 3C95 ferrite real permittivity vs. frequency based on the CPE.

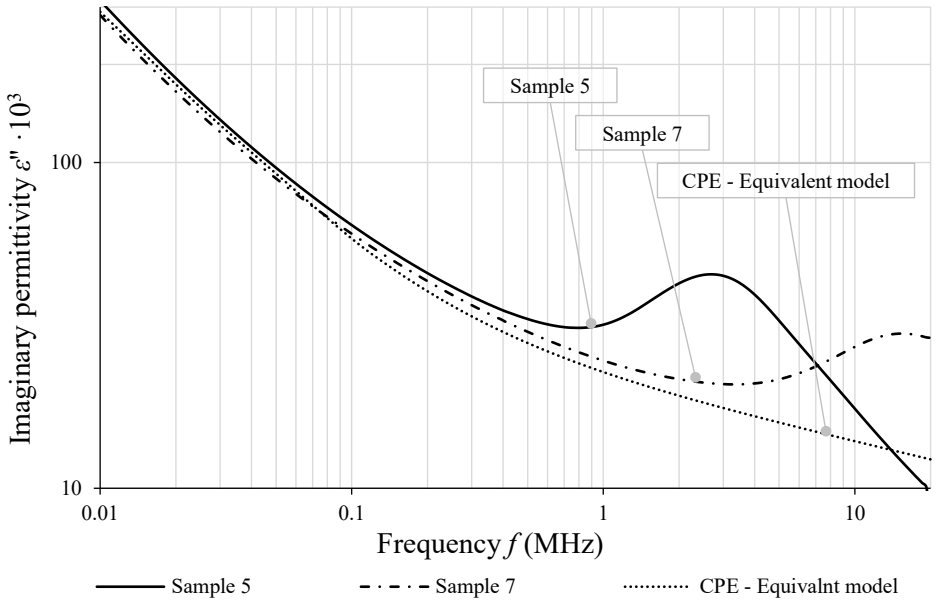


Figure 47. 3C95 ferrite imaginary permittivity vs. frequency based on the CPE model.

TABLE 5. 3C95 CPE EQUIVALENT PARAMETERS TO MODEL REAL AND IMAGINARY PERMITTIVITY.

R_1	Q_1	n_1	R_2	Q_2	n_2
3.953×10^{6}	4.006×10^{-7}	0.215	9.854×10^{6}	4.898×10^{-11}	1.0

Seven Mn-Zn ferrite materials were selected to determine the electrical properties. Thus, the obtained permittivity vs. frequency characteristic provides the material data with the highest possible accuracy for further calculation. Plots of real and imaginary permittivity as a function of frequency are shown in Figure 48 and Figure 49, respectively.

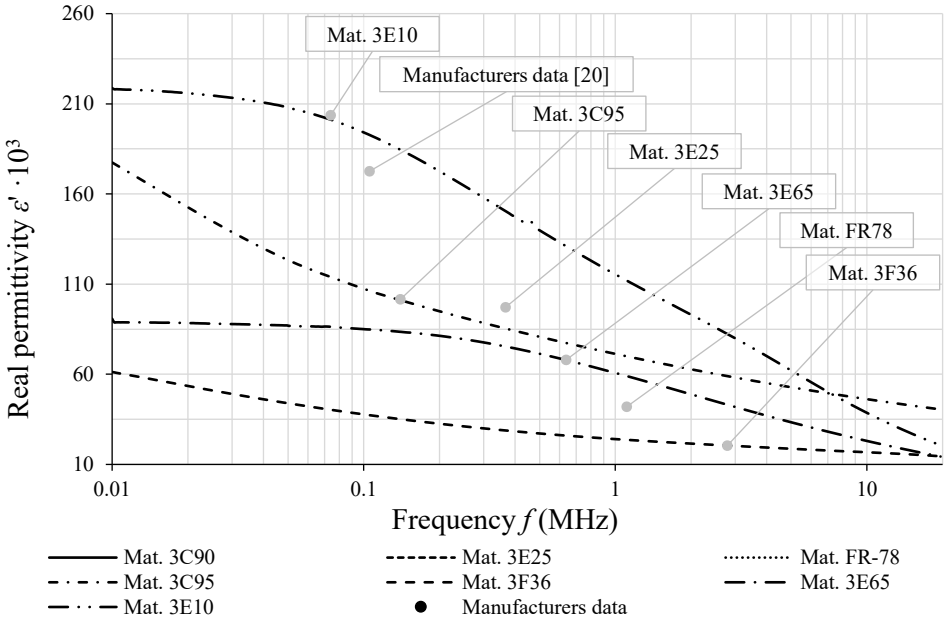


Figure 48. Mn-Zn ferrite real permittivity vs. frequency based on the experimental data.

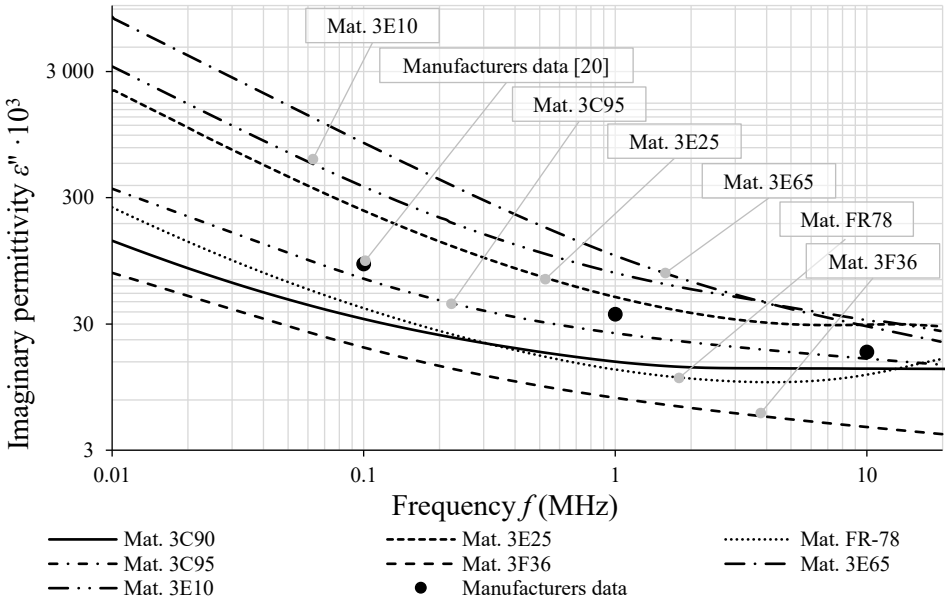


Figure 49. Mn-Zn ferrite imaginary permittivity vs. frequency based on the experimental data.

Appendix B contains tabulated complex permittivity characteristic for the Mn-Zn ferrite.

2.2.4 Complex permittivity temperature effect

The influence of temperature on ferrite dielectric properties for three selected materials 3C95, 3F36 and 3E10, is shown in Figure 50, Figure 51, and Figure 52, respectively. Ferrite complex permittivity shows a high temperature dependency similar to the complex permeability temperature dependency. At temperature increase causes an increase in real permittivity in the analyzed frequency range. Material 3E10 shows the highest temperature dependence. Imaginary permittivity also increases with temperature. The biggest parameter variation is observed at low frequencies for all tested materials.

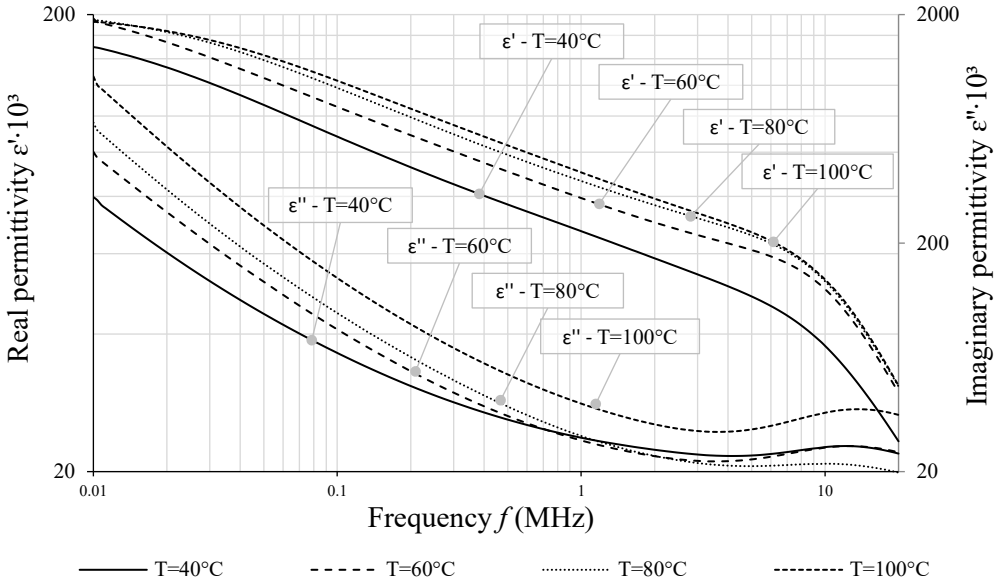


Figure 50. 3C95 ferrite complex permittivity vs. frequency and temperature.

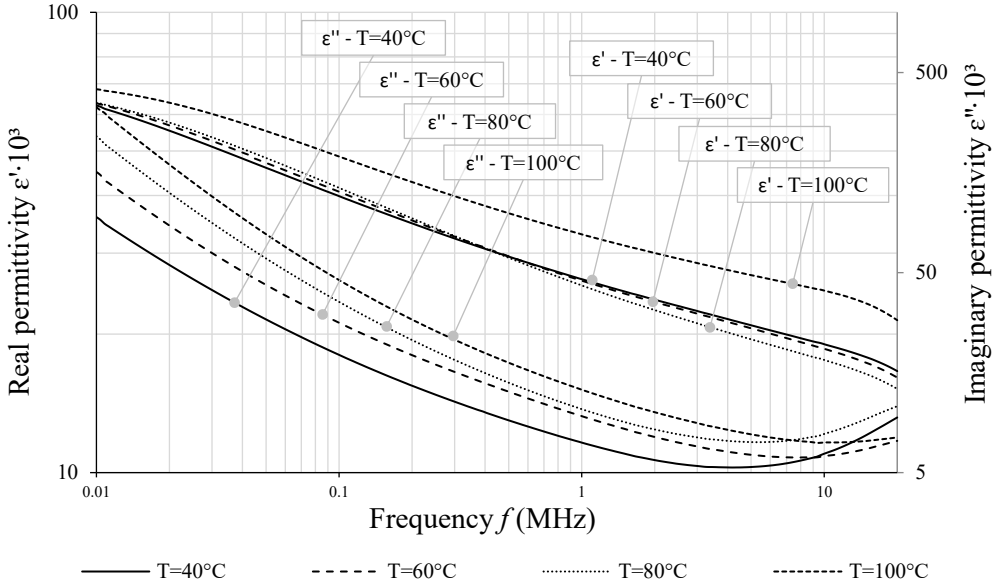


Figure 51. 3F36 ferrite complex permittivity vs. frequency and temperature.

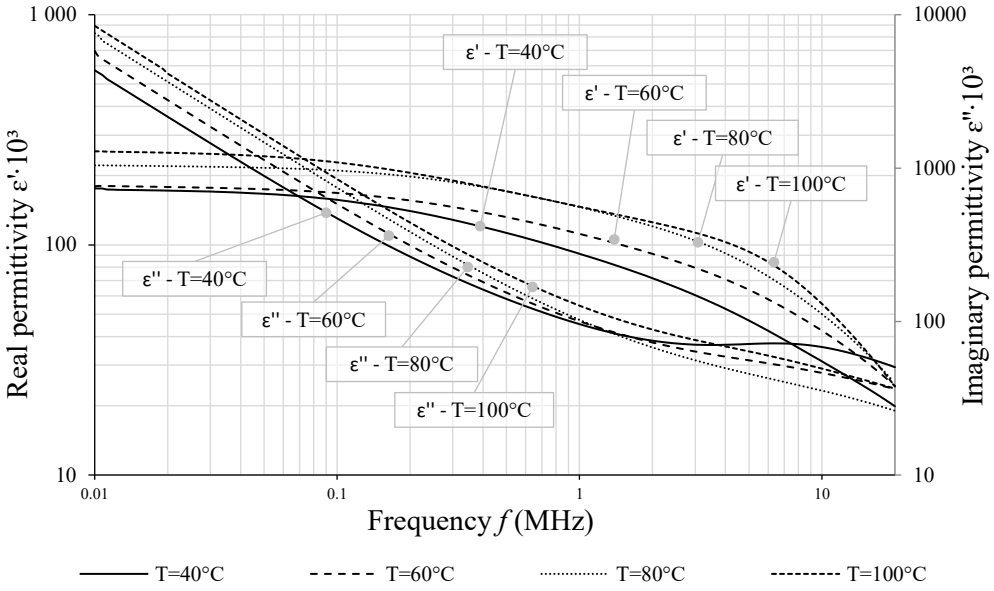


Figure 52. 3E10 ferrite complex permittivity vs. frequency and temperature.

2.2.5 Complex permittivity force effect

The proposed test fixture is equipped with strain gauges for compression force control. The force applied during the measurements ensures that the impact of sample contact resistance is minimized. However, excessive force may cause significant parameter variation. The compression force influence on the ferrite dielectric properties for three selected materials 3C95, 3F36 and 3E10, is shown in Figure 53, Figure 54 and Figure 55, respectively. Real permittivity increases with pressure, while the dielectric constant is somewhat complementary to permeability. Imaginary permittivity shows a small pressure dependence, the biggest imaginary permittivity variation is visible at the frequency where the dimensional resonance occurs.

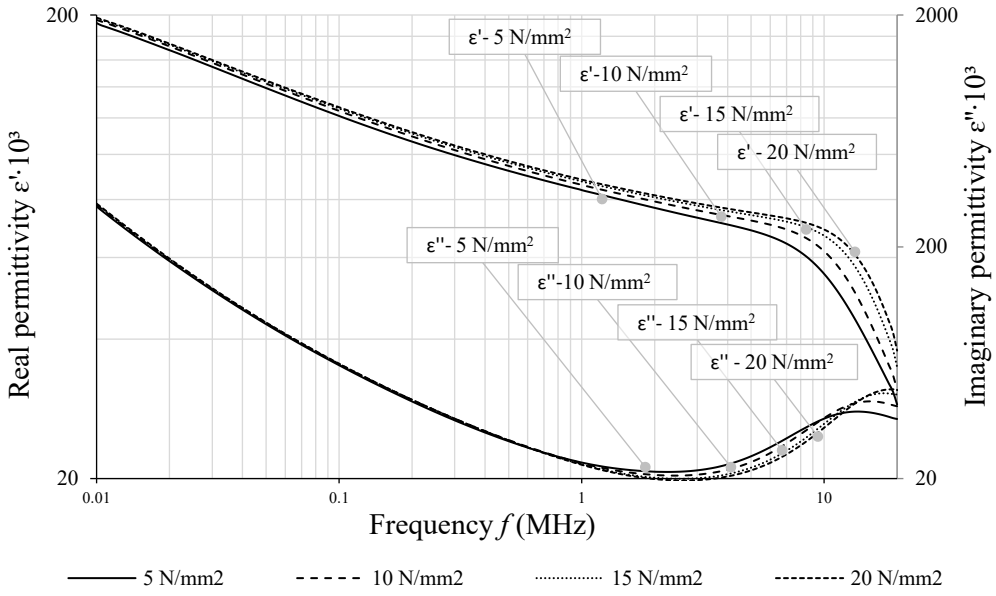


Figure 53. 3C95 ferrite complex permittivity vs. frequency and tension.

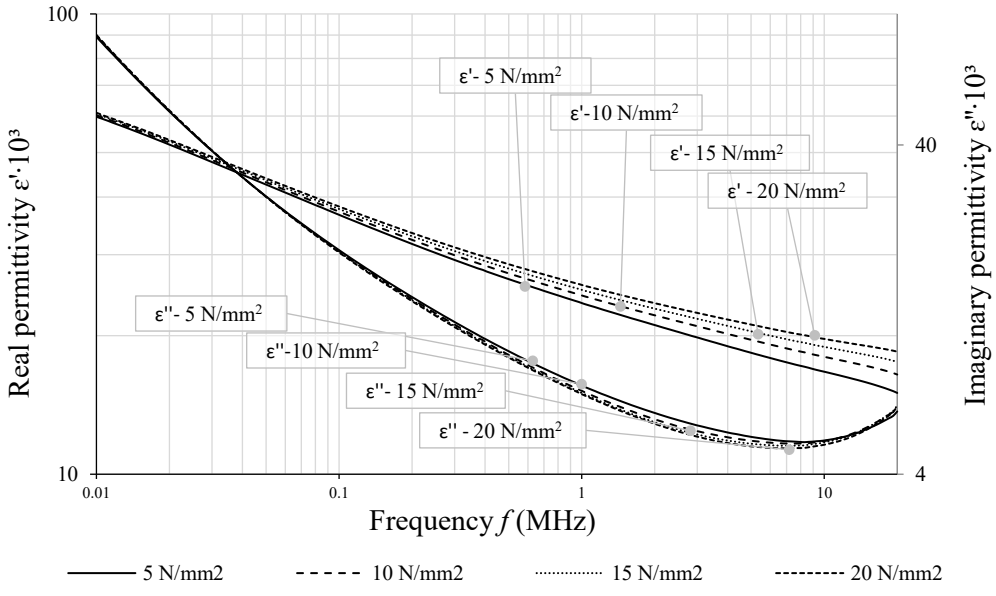


Figure 54. 3F36 ferrite complex permittivity vs. frequency and tension.

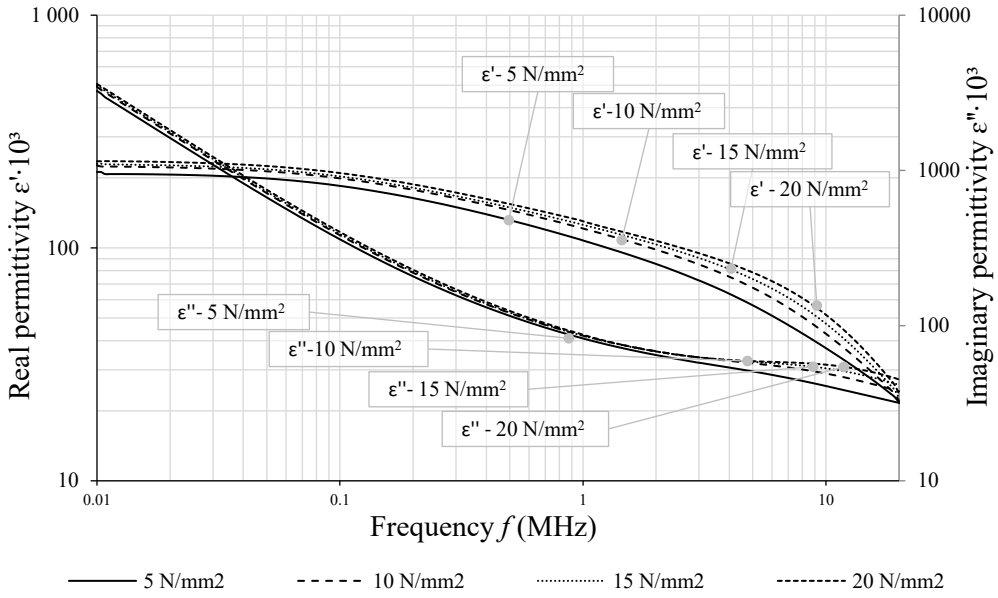


Figure 55. 3E10 ferrite complex permittivity vs. frequency and tension.

2.3 Power losses

Accurate core loss prediction is an essential part of the magnetic component design process in power electronics applications. State-of-the-art methods are based on the sinusoidal excitation loss measurement for small cores with an external diameter of 29 mm. This constitutes a foundation for the widely-used Steinmetz equation [34]. However, the Steinmetz equation parameters are provided as constants regardless of the core shape and size, which is counter intuitive to the findings presented in section 2.1.

2.3.1 Loss tangent

The primary method to validate and assess the ferrite core performance is the magnetic loss tangent which is based on frequency characteristics of the complex permeability at a low-field amplitude. As shown in Section 2.1, the dimension of the tested Mn-Zn ferrites affects the measured complex permeability and thus the power loss itself. Figure 56 shows the magnetic loss tangent for 3C95 material measured for three core sizes. The loss tangent curves show that the magnetic loss tangent for the tested cores are nearly equal at low frequency, and as frequency increases, the loss tangent also increases, but disproportionally. The magnetic loss tangent in the larger core increases much faster than in the case of the small core, and for the T87 core, at 500 kHz, it is 5 times higher than for T29.

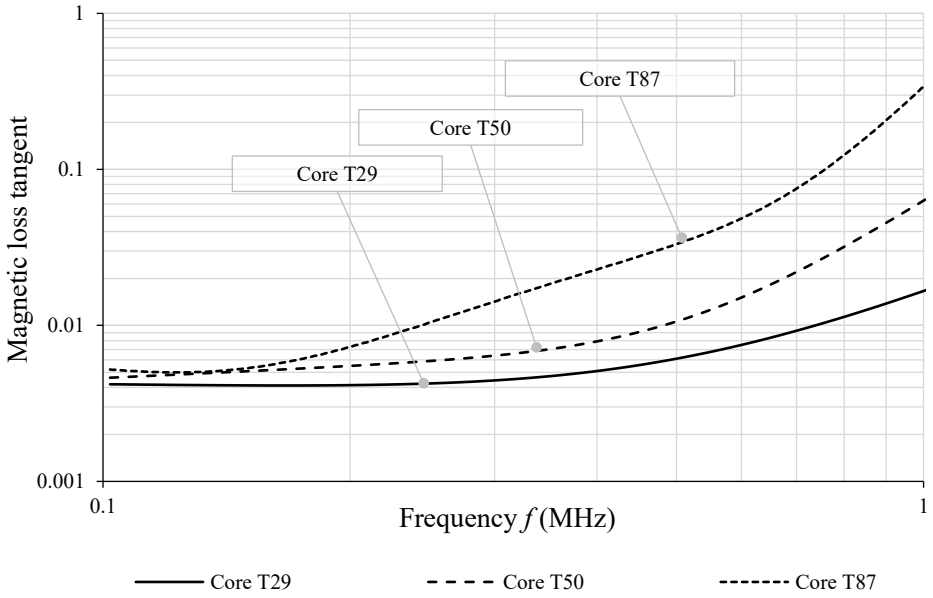


Figure 56. The magnetic loss tangent vs. frequency for 3C95 material based on experimental data.

2.3.2 Performance factor

One of the most popular parameters to compare material losses as a function of frequency is the performance factor [46]. The multiplication of the maximum allowed flux density, B, and the sinusoidal frequency, f, describes the performance factor PF:

$$PF = B \cdot f \tag{2.13}$$

A high-performance factor indicates a material that allows for operation with the highest flux density at a specific frequency and power loss density. Parameterized power loss density is an indicator that links the magnetic performance with the thermal capability of the component. The performance factor is also included in Faraday's Law and describes the effective cross sectional area of the core:

$$A_C = \frac{V_{RMS}\sqrt{2}}{2\pi \cdot B \cdot f \cdot N} = \frac{V_{RMS}\sqrt{2}}{2\pi \cdot PF \cdot N} \tag{2.14}$$

where A_C is the effective core cross section, V_{RMS} is the rms value of the voltage across the winding and N is the number of turns.

The core size and operating frequency have strong impacts on the power losses. In order to show this dependency three core samples, T29, T50 and T87 made of 3C95 ferrite material, were tested.

The core losses were measured with the two-winding method, including an adjustable compensation capacitor to cancel the reactive voltage [47]. The measurement setup and windings arrangement are presented in Figure 57. The test system is powered by a signal generator with amplifier AR800A3B, while the voltage and current are measured with a Tektronix MSO56 oscilloscope, equipped with two TIVH08 voltage probes and a TCP0030A current probe [48].

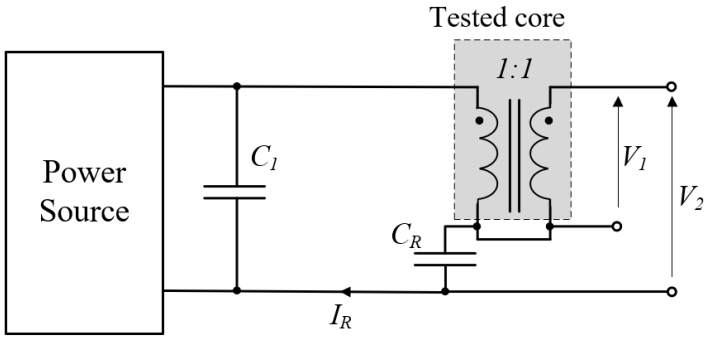


Figure 57. Core power loss measurement setup with sinusoidal excitation.

Performance-factor frequency characteristics for various core sizes for 3C95 material are shown in Figure 58. The performance factor curves for 3C95 material show that the power loss density for the tested cores are nearly equal at low frequency, up to 100 kHz. As frequency increases, the power losses also increase. Power losses in the larger cores increase much faster than for the small cores. At 600 kHz, the power losses for T87 core are 35% higher than for T29.

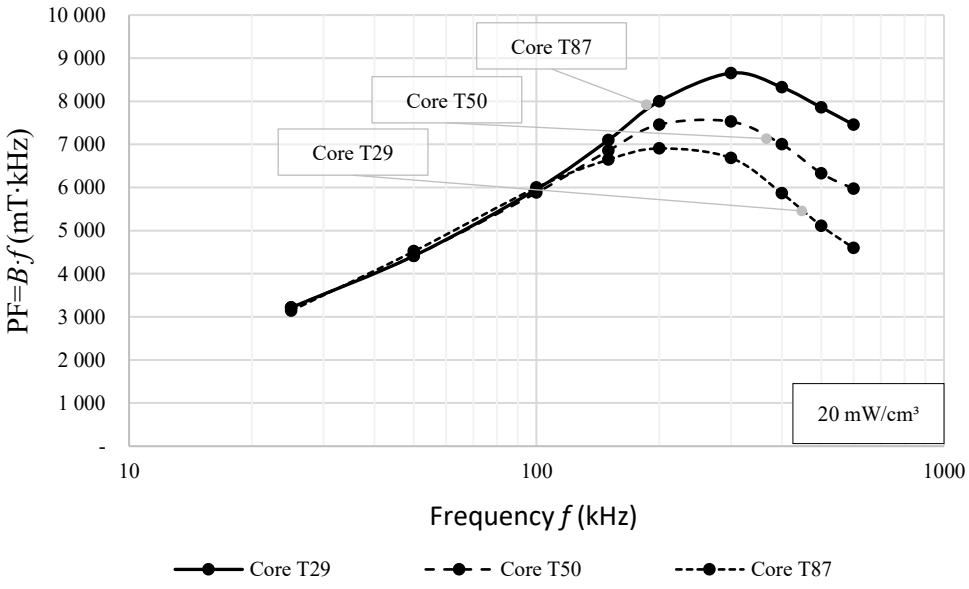


Figure 58. The performance factor vs. frequency for 3C95 material.

2.3.3 Power loss under the rectangular excitation

The magnetic loss tangent and power factors curves show a strong loss variation for the different core sizes. There is an indication that the state-of-the-art methods become insufficient due to the input data based on one core size. As a consequence, a decision was made to perform a preliminary investigation of the core size effect on power losses at a high field amplitude. In modern power electronics systems, the voltage across the inductors and transformers shows a rectangular shape, therefore the core losses described in this section are measured for rectangular wave excitation as well.

In order to measure core losses, the *B-H* loop measurement is evaluated as the most suitable [49],[50]. Among other advantages, this approach offers fast measurements (compared to other methods, e.g., calorimetric measurements) and good accuracy. Furthermore, copper losses are excluded from the measurements by means of two windings placed around the tested core. The sense winding (secondary winding) voltage, V_{DUT}, is integrated to calculate the core flux density, *B*, defined as:

$$B(t) = \frac{1}{N \cdot A_C} \int_0^t v_{DUT}(t)dt \tag{2.15}$$

The current in the excitation winding (primary winding) is proportional to the magnetic field strength *H* as follows:

$$i(t) = \frac{H(t) \cdot l_c}{N} \tag{2.16}$$

The simplified schematic and a photo of the power stage are shown in Figure 59. The test system includes a power stage, a power supply, an oscilloscope and a computer with Matlab [51].

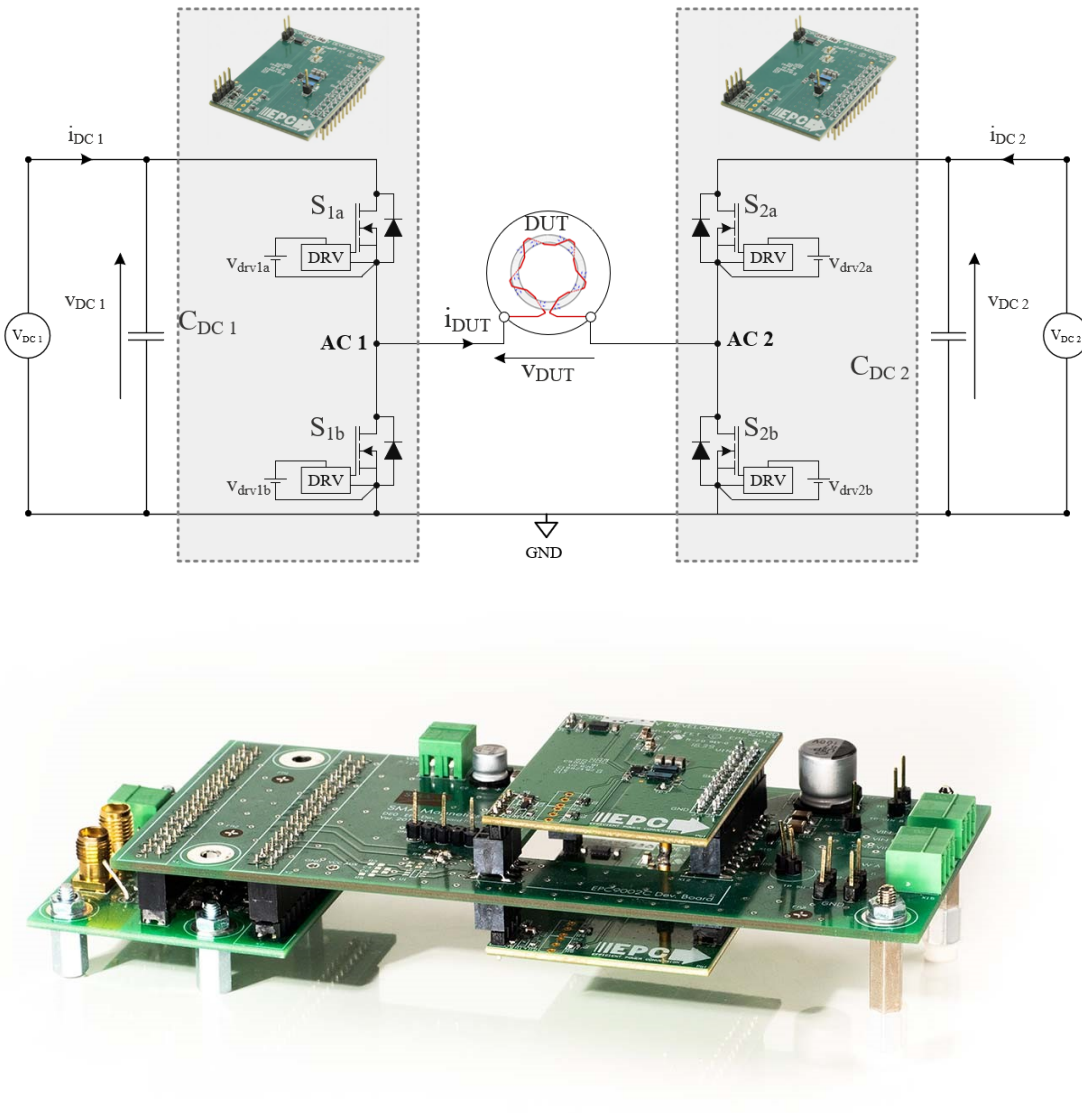


Figure 59. Schematic and photo of the core loss test setup.

The backbone of the system includes two development boards PEC2001C, with each board containing two GaN FET transistors in a half bridge configuration with Texas Instrument's LM5113 gate driver, a power supply, and a bypass capacitor [52]. The boards also provide all the necessary components together with a layout for optimum switching performance, including various probe points for waveform measurements. The test setup may be easily duplicated, as the detailed schematic diagram and PCB layout are shown in Appendix C. The power stage is capable of a maximum input voltage of 60 V, output current of 10 A, and a switching frequency of up to 500 kHz. The developed test setup allows an application of a general rectangular voltage wave with variable duty cycle as well as asymmetric rectangular wave with constant volt-seconds, in each half of the waveform. The test system is controlled by Matlab, while voltage and current are measured with a Tektronix MSO56

oscilloscope, equipped with a TIVH08 voltage probe and a TCP0030A current probe [47]. The measured waveforms together with calculated energy and the B-H loop at a single operating point, f=100 kHz, V_{IN} = 9 V are illustrated in Figure 60.

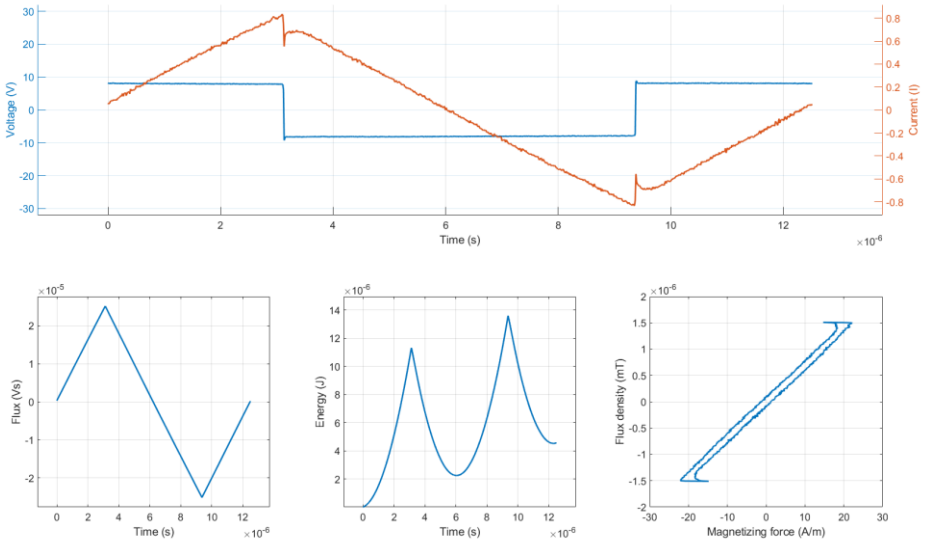


Figure 60. Waveforms used by the Matlab program to calculate core losses at each operating point [53].

Core losses under the rectangular excitation were measured for three different core samples, T29, T50 and T87, made of 3C95 ferrite material. All tested cores were subjected to the same core flux density at each frequency. Figure 61 shows a Herbert curve in which core losses per unit volume are plotted as a function of frequency to illustrate the core size effect on power losses. The Herbert curves for the 3C95 material show that the power loss density for the tested cores is nearly equal at low frequencies [54]. In addition, if the frequency increases, the power losses decrease to the minimum at 150 kHz. Further frequency increases cause the power losses to increase. The power losses in the T87 core are much higher than in the case of the T29 core. An additional feature of the Herbert curve, which increases its attractiveness, is the direct identification of optimum operating frequency for the core, showing at the same time core losses at other operating points.

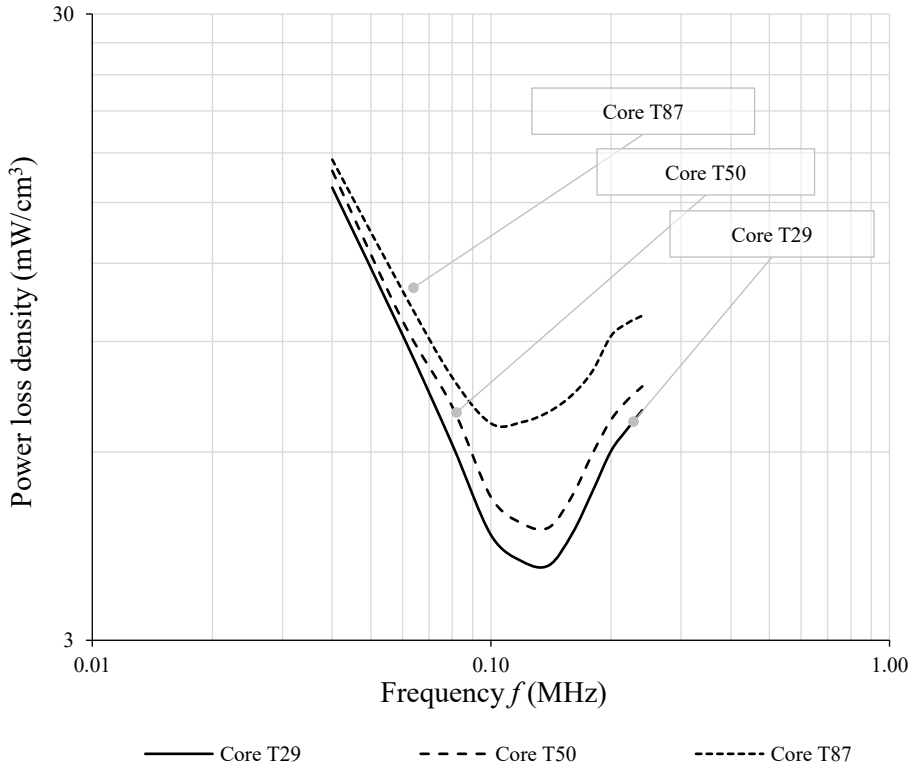


Figure 61. Herbert curve, power loss density vs. frequency for 3C95 material.

Magnetic losses in ferrite cores cannot be accurately calculated from published loss curves, as they do not account for performance deterioration with size. The magnetic loss tangent frequency characteristics show core loss increases up to the frequency where dimensional resonance is visible. Measurement with a higher field amplitude shows a local loss minimum at low frequency which is not visible in the low-field amplitude characteristic. Therefore, further in-depth analysis is required to quantify this effect, as the increase in eddy current losses could dominate the measurements at high field amplitude and suppress the dimensional resonance. It may lead to the conclusion that dimensional resonance has a significant effect on EMI filters that by nature operate at much lower signal levels.

2.4 Conclusions

A design of magnetic components intended for high-frequency applications requires detailed information on magnetic materials. This chapter outlined the measurement methods used to determine the critical material parameters. The results of the tests produced a significant observation that permeability, permittivity, and power loss vary with the physical core size. In general, the performance deteriorates as the size increases. The performance drop

in permeability and power loss is seen at lower frequencies for large size cores. The permeability and permittivity change with the levels of applied compression force and temperature that can be experienced in applications. The CPE method has been introduced to enable accurate modelling of the core permittivity vs. frequency.

3 MODELLING OF MAGNETIC FIELD DISTRIBUTION IN MN-ZN FERRITE CORES

Abstract - This chapter presents a comprehensive investigation of magnetic flux distributions in Mn-Zn ferrite cores. As the performance of the material is known from chapter 2 we can now develop specific models to calculate the flux distribution for specific core shapes. FEM analysis is known as the high-fidelity method for magnetic flux calculation; however, it is burdened with substantial calculation time. Therefore, two additional methods which both simplify the calculation process, and also retain the merit of a detailed analysis of the magnetic flux distribution, are presented: (i) the 1-D analytical model and (ii) the shell-based transmission-line model. The detailed analysis of the magnetic flux distribution, based on each model, is presented across a range of selected core sizes and materials. The accuracy of the models is validated by comparison with experimentally measured characteristics of complex permeability.

Section 3.1 presents a short introduction to a detailed analysis of the magnetic flux distribution in Mn-Zn ring cores, based on the complex material characteristics. Section 3.2 outlines the 1-D model capturing the impact of the skin depth and dimensional resonance on the magnetic flux distribution. Section 3.3 discusses a novel, intuitive shell-based transmission line model. The results of the magnetic flux analysis, based on FEM modelling, are presented in Section 3.4. A practical aspect of the analysis is discussed in Section 3.5, while a brief conclusion is presented in Section 3.6.

The results of this chapter have been published in the following papers and presentations:

- M. Kacki, M.S. Rylko, J.G. Hayes, C.R. Sullivan, "Analysis and Experimental Investigation of High-frequency Magnetic Flux Distribution in Mn-Zn Ferrite Cores," *IEEE Transactions on Power Electronics* (Early Access), August, 2022.

3.1 Introduction

In order to design magnetic components for high frequency, high power applications, detailed information on the magnetic core performance is required. The magnetic material tests show that the core properties such as permeability, permittivity and power loss deteriorate as the core size increases; thus, in order to have good quality input data for core modeling, it is necessary to measure the frequency characteristic for each of the considered core sizes as well as the material. This approach is not only laborious but also time-consuming as the considered core shapes must be available before the design process is started. What is more, it requires the engineer to possess a large database with the core characteristics for various shapes and materials. Alternatively, a specific model that predicts core performance based on reference material characteristics can be employed. Such a model must provide an analytical interpretation of the magnetic material performance over frequency and physical size, including high-frequency effects such as skin depth and dimensional resonance. Therefore, two alternatives to the FEM calculation methods for detailed analyses of the magnetic flux distribution are introduced: the 1-D analytical model and the shell-based transmission-line model.

3.2 1-D analytical field distribution model

3.2.1 Theory

The analytical model (3.1) has previously been developed for the magnetic field calculation within an infinite ferrite plate [55], [56]. The plane is infinite along the *y* and *z* axes, and finite along the *x* axis, as shown in Figure 62. The equation allows for the modeling of the electromagnetic wave propagation in lossy materials, suitable for ferrite materials. The solution of the Maxwell`s equations for a sinusoidal source magnetic field *H* of a linear, homogeneous, and isotropic material yields the expression (3.1), below. Further analyses are carried out with those assumptions.

$$H_y(x) = H_0 \frac{\cos\left(\frac{j\bar{k}x}{c}\right)}{\cos\left(\frac{j\bar{k}d}{2c}\right)} \tag{3.1}$$

$$\bar{k} = \omega\sqrt{(\mu' - j\mu'')(\varepsilon' - j\varepsilon'')} \tag{3.2}$$

where d is the ferrite thickness, k is the complex wave propagation constant, c is the speed of the light in a vacuum, H_0 is the boundary-condition value of the magnetic field on the two infinite surfaces of the ferrite plate, and H_y is the calculated value of the magnetic field.

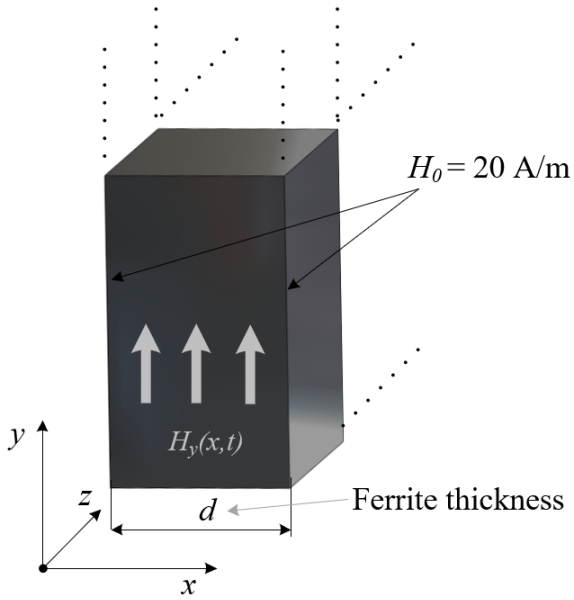


Figure 62. Ferrite infinite plate for analytical calculation of the flux distribution in the core.

Equation 3.1 shows that the magnetic field distribution within the infinite ferrite plate depends on complex material properties through a propagation constant, and ferrite plate thickness, d. Since the material properties are frequency dependent, the resultant magnetic field distribution must also be frequency dependent. The flux density $B(x)$ in the analyzed core plate is related to the $H(x)$ field through the permeability of the core. Core losses are modeled by the material complex permeability and permittivity. Therefore, the magnitude of the flux density, at any point in the core, is the result of an in-phase real part and out-of-phase imaginary part.

3.2.2 Results

As part of the first phase, the equation is used to model the field distribution in two specific ferrite materials: 3F36 and 3E10. The ferrite plate thickness and the considered frequency range are individually selected for each material to illustrate the high frequency effects.

The calculated real and imaginary components of the magnetic field for the 3F36 material in an infinite ferrite plate with a thickness of 15 mm, and a magnetic field of 20 A/m are shown in Figure 63 and Figure 64, respectively. The real part of the magnetic field within the 3F36 ferrite core is uniform, and in phase with the source field at low frequencies. At

approximately 1 MHz, there is a noticeable peak in the magnetic field due to dimensional resonance. As frequency increases, the magnetic field drops sharply. The imaginary part of the magnetic field shows a significant loss increase in the frequency range between 1 and 2 MHz.

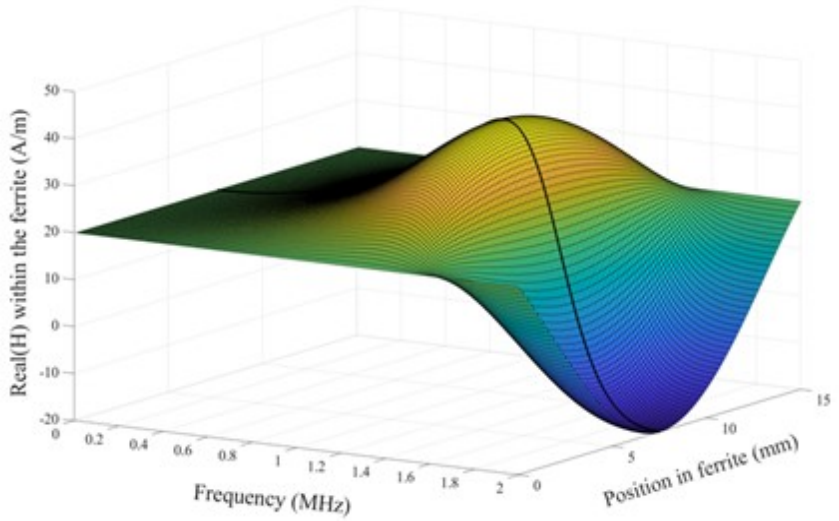


Figure 63. Calculated real field component within 15 mm ferrite plate of 3F36 material.

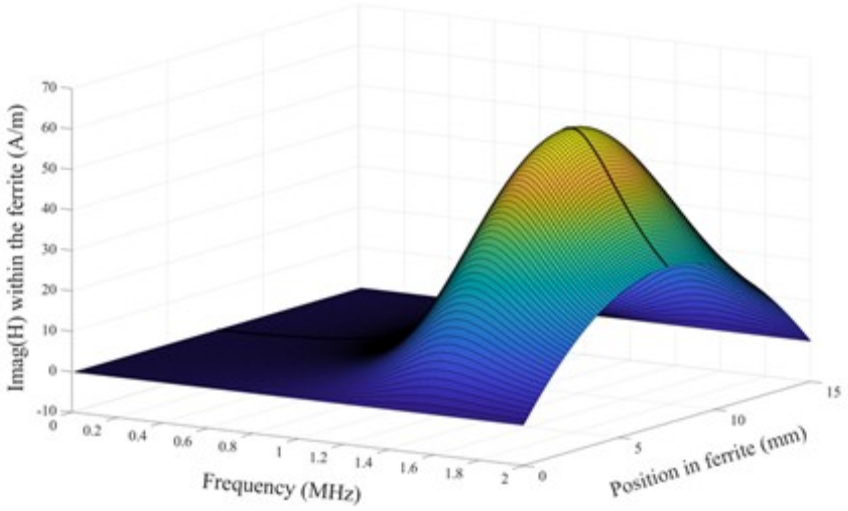


Figure 64. Calculated imaginary field component within 15 mm ferrite plate of 3F36 material.

Figure 65 and Figure 66 show the real and the imaginary components of magnetic field plotted at a constant frequency of 1 MHz for ferrite plates with a varying thickness ranging from 5 mm to 40 mm.

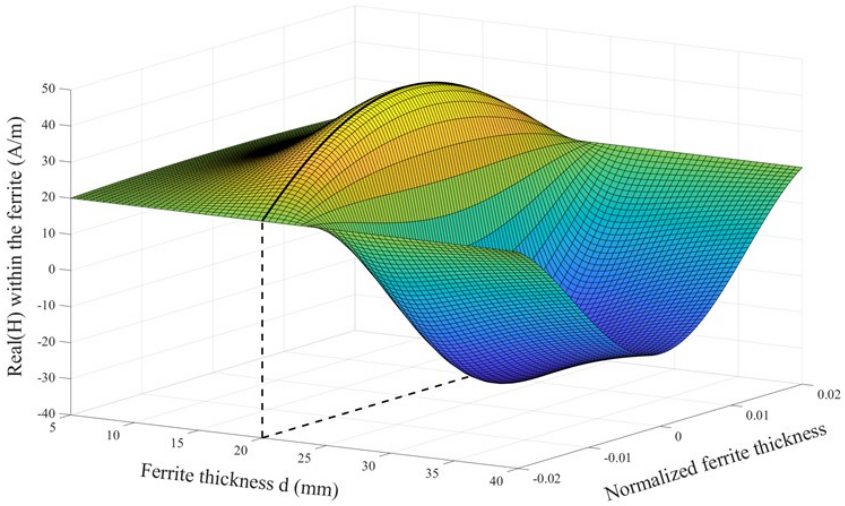


Figure 65. Calculated real field component within ferrite plate for various thicknesses of 3F36 material.

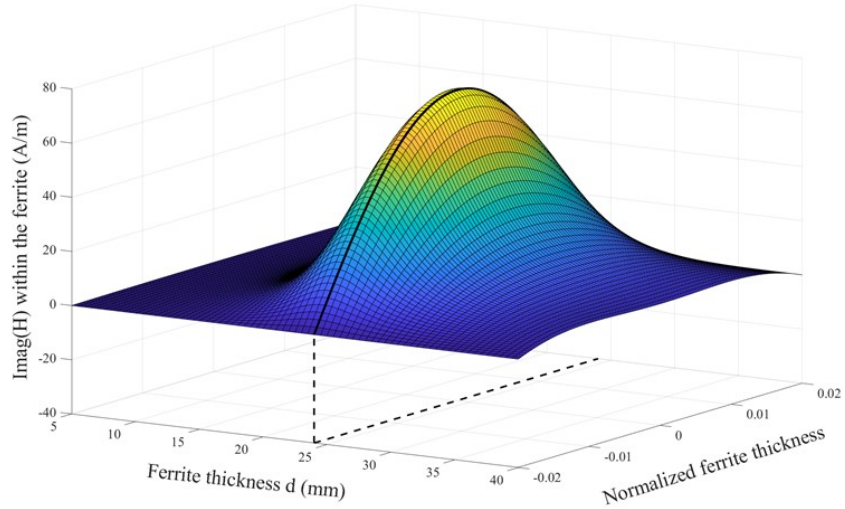


Figure 66. Calculated imaginary field component within ferrite plate for various thicknesses of 3F36 material.

Figure 64 and Figure 65 show that if the thickness of the ferrite plate is low, the magnetic field is uniform and in phase with the excitation field. The plots indicate that a dimensional resonance is established for a specific core size and frequency. In order to maximize the effect of the 3F36 material permeability in a real application operating at 1 MHz, the core cross section dimension should not exceed 20 mm, where the magnetic field shows a noticeable peak. The loss peak is visible in the core when the cross-section dimension is equal to 24 mm.

The calculated real and imaginary component of the magnetic field for 3E10 material in an infinite ferrite plate with a thickness of 10 mm, and an excitation field of 20 A/m is

shown in Figure 67 and Figure 68, respectively. For the 3E10 material, the frequency is limited to 500 kHz while the ferrite thickness is set to 10 mm.

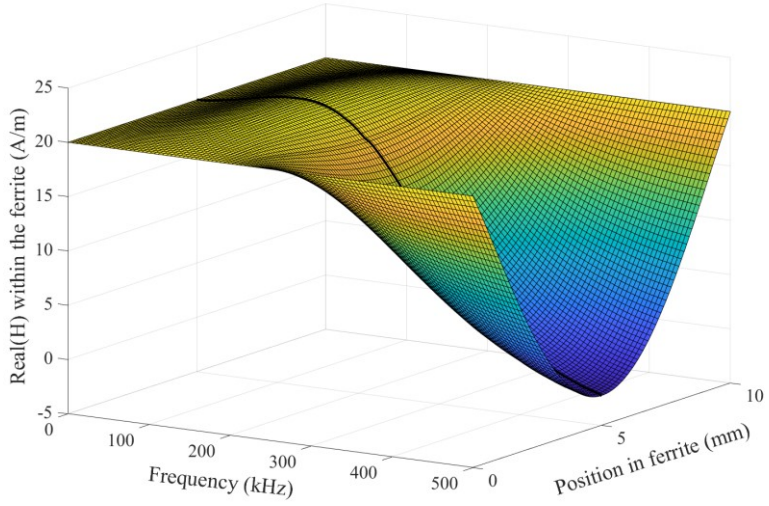


Figure 67. Calculated real field component within 10 mm ferrite plate of 3E10 material.

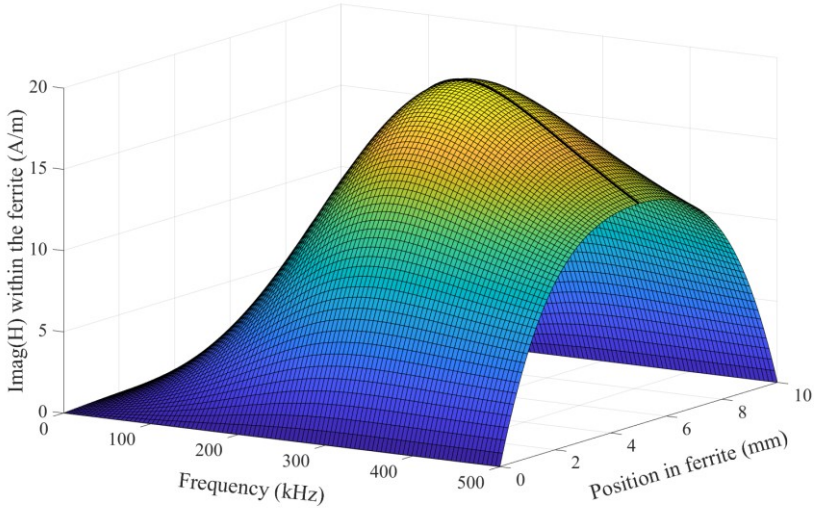


Figure 68. Calculated imaginary field component within 10 mm ferrite plate of 3E10 material.

The magnetic field within the 3E10 ferrite plate gradually decreases as the frequency increases. The onset of the skin effect starts at 100 kHz. In this case, the frequency above 100 kHz is considered high, since the magnetic field is concentrated around the outer core surface at higher frequencies and becomes weaker in the core center. Analytical results for the 3E10 ferrite look similar to the classic high-frequency current distribution in a rectangular conductor. The imaginary part of the magnetic field shows a significant loss increase in the

frequency range between 200 kHz and 500 kHz. However, the loss peak is 3 times lower than for the 3F36 material shown in Figure 66. The magnetic field change in the analyzed frequency range for the 3E10 material is moderate as opposed to the 3F36 material which is degraded significantly due to dimensional resonance.

Figure 69 and Figure 70 show real and imaginary magnetic fields plotted for a constant frequency of 250 kHz for a 3E10 ferrite plate of variable thickness from 5 mm to 40 mm.

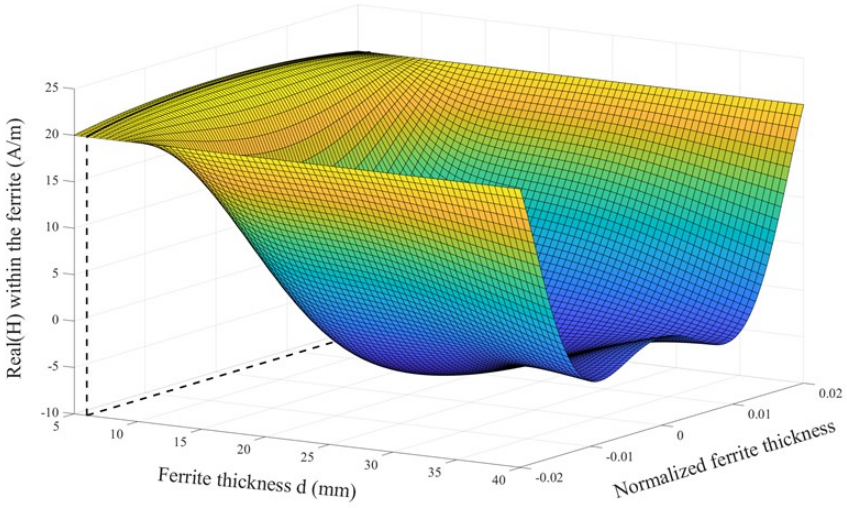


Figure 69. Calculated real field component within ferrite plate for various thicknesses of 3E10 material.

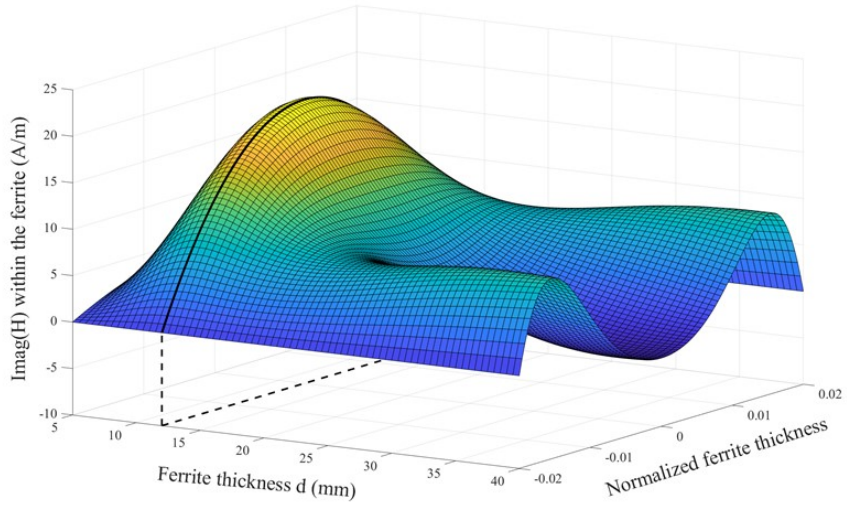


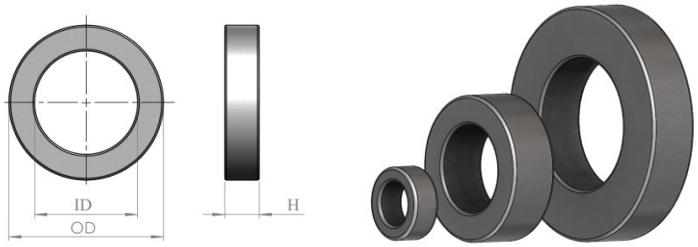
Figure 70. Calculated imaginary field component within ferrite plate for various thicknesses of 3E10 material.

The plots indicate that only small ferrite cores, with a cross-sectional dimension of up to 6 mm, show uniform flux distribution free from skin effects. The peak of the loss shown in the imaginary component of the magnetic field is visible for the core with a cross-sectional dimension of 12 mm.

3.2.3 Experimental validation

The field distribution plots, presented already above, depict a relation between the size of the core, frequency, and the complex material characteristic, as well as its impact on the core's overall performance. Although, the presented characteristics indicate material performance, the practical application requires that the complex permeability characteristics should be related to the selected core. In order to show this dependency, the complex permeability characteristics, for three core sizes: T29, T50, and T80 of outer diameter 29 mm, 50 mm, and 80 mm, respectively, made of two materials 3F36 and 3E10, are compared with the 1-D analytical calculation results. Detailed dimensions of the cores are presented in Table 6.

TABLE 6. CORE PARAMETERS USED FOR ANALYTICAL CALCULATION VERIFICATION.

Core type	Core material	Dimensions OD x ID x H	Core cross section dimension	Core cross section	Core volume
Unit	-	mm	mm	mm^2	cm^3
T29	3E10 3F36	29 x 19 x 10.5	5 x 10.5	53	3.96
T50	3E10 3F36	50 x 30 x 14	10 x 14	140	17.59
T80	3E10 3F36	80 x 45 x 17.5	17.5 x 17.5	306	60.13
					

The 1-D analytical equation was used to calculate the magnetic field for an infinite ferrite plate. The thickness of the plate corresponds to the lowest cross-sectional dimension of the tested cores, shown in Table 6. In order to compare the achieved results the complex

permeability for each sample is measured and normalized with respect to the initial permeability for real permeability, and to a maximum value for imaginary permeability. For the calculated field distribution, the magnetic field within the ferrite is integrated over the ferrite thickness and normalized in the same way as measured data. The generated complex permeability characteristics for 3F36 cores are shown in Figure 71 and Figure 72, while for the 3E10 cores the characteristic are shown in Figure 73 and Figure 74.

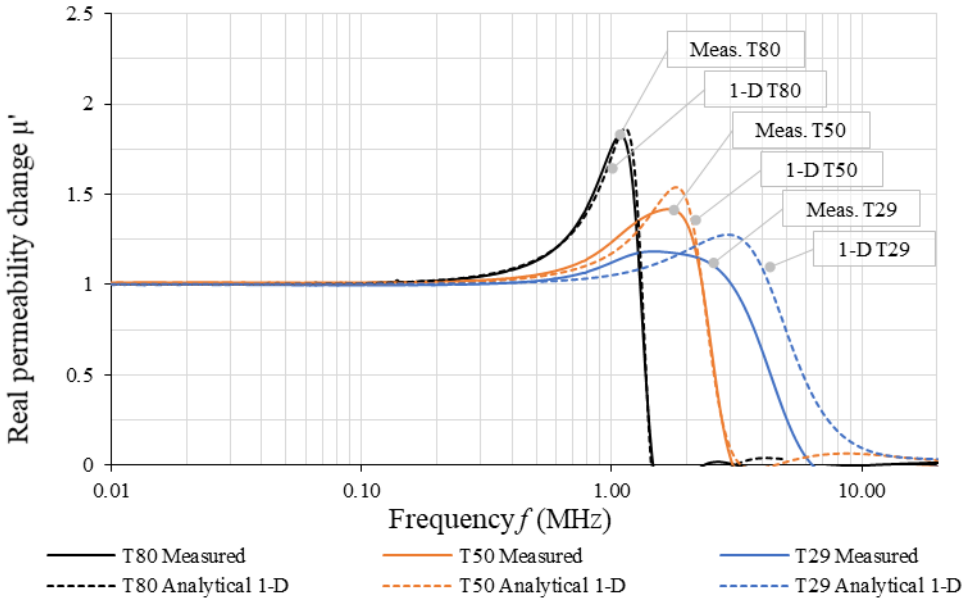


Figure 71. 1-D model calculated and measured normalized real permeability vs. frequency for 3F36 ferrite cores.

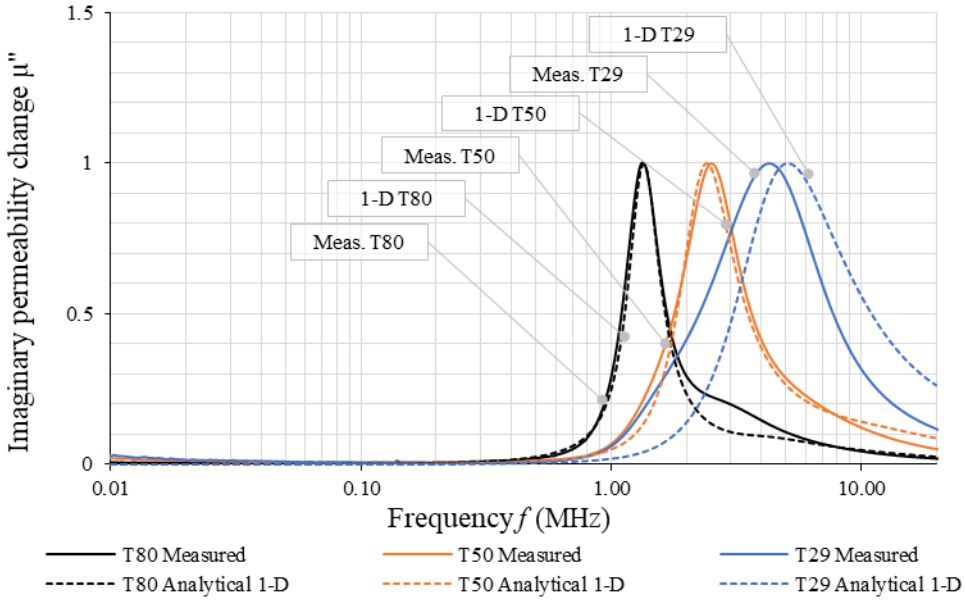


Figure 72. 1-D model calculated and measured normalized imaginary permeability vs. frequency for 3F36 ferrite cores.

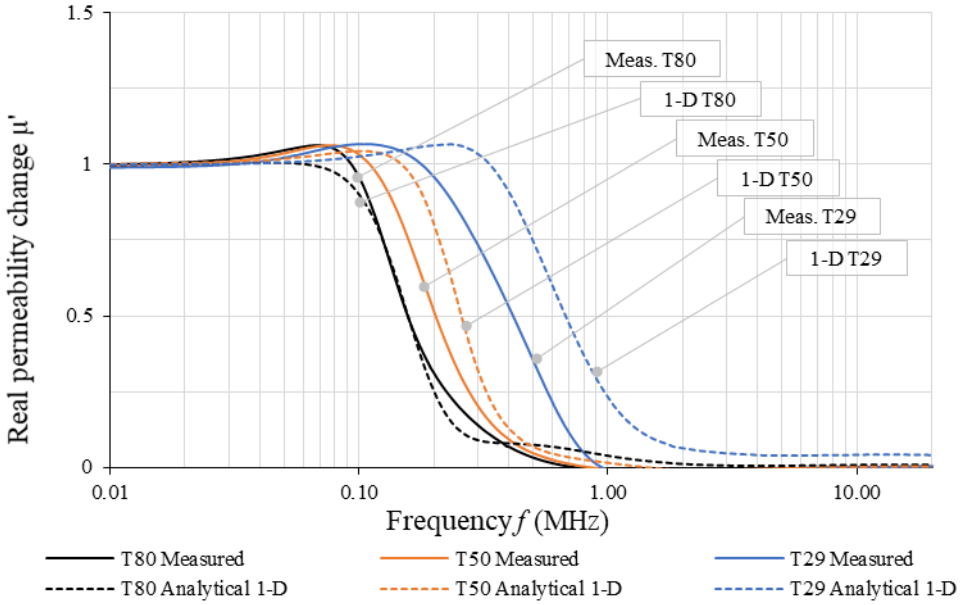


Figure 73. 1-D model calculated and measured normalized real permeability vs. frequency for 3E10 ferrite cores.

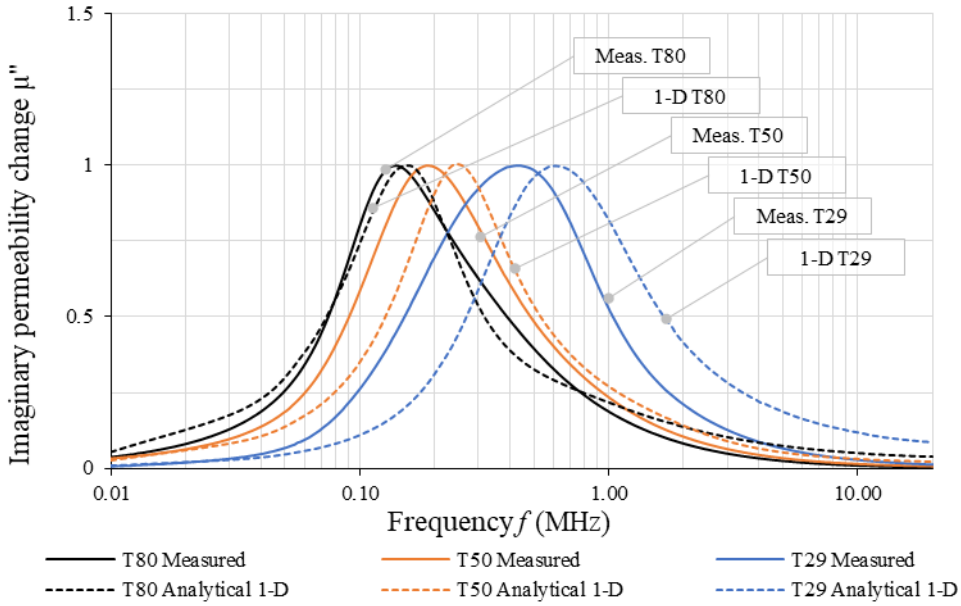


Figure 74. 1-D model calculated and measured normalized imaginary permeability vs. frequency for 3E10 ferrite cores.

The 1-D analytical equation, based on the complex material characteristics, follows the experimental results with a relative accuracy of +/- 10% for the samples with the core cross sectional area shape ratio 1:1. Moreover, it should be stated that the peak of the characteristics is well represented. Therefore, the 1-D model is a good indication of the measured characteristic. The best accuracy is achieved for the biggest core, T80, while the lowest

accuracy is achieved for the T29 core, for both materials. The T29 core falls out of the range due to the core cross-sectional area shape ratio of 2:1. The T80 cores have a square core cross-sectional area, therefore the smallest core cross-sectional dimension used for the magnetic field calculation is the same in both directions and represents a complete field distribution within the core. In the case of the T29 core, the thickness of the ferrite plate was set to 5 mm, while in the other direction, the core height amounts to 10 mm, and the field distributions are different. Therefore, the core shape ratio constrains the 1-D approach to limited core cross sectional area shape ratio.

3.2.4 Conclusions

The plots presented, show that the core frequency characteristic can be modelled and predicted based on the idealized one-dimensional analytical model. The best accuracy is achieved for the biggest core with the lowest for the smallest cores. Both tested materials show similar frequency dependency. In each calculation case the materials' complex permeability and permittivity are key input parameters.

3.3 Core transmission line model

The transmission line model, TLM, with multiple variants is known for the modeling of high-frequency eddy-current effects in power transformers [56]-[58], and the wave propagation modeling in cables, and machine windings [59],[60]. However, the available publications that deal with modeling of ferrite cores are limited [61].

3.3.1 Theory

The core's circuit transmission-line model is especially intuitive to electrical engineers. The calculation can be applied in any circuit simulator and can also be easily incorporated into simulation of a higher-order system. The principle-based approach consists in sectioning the magnetic core, as shown in Figure 75, while existing methods describe the core as a bulk.

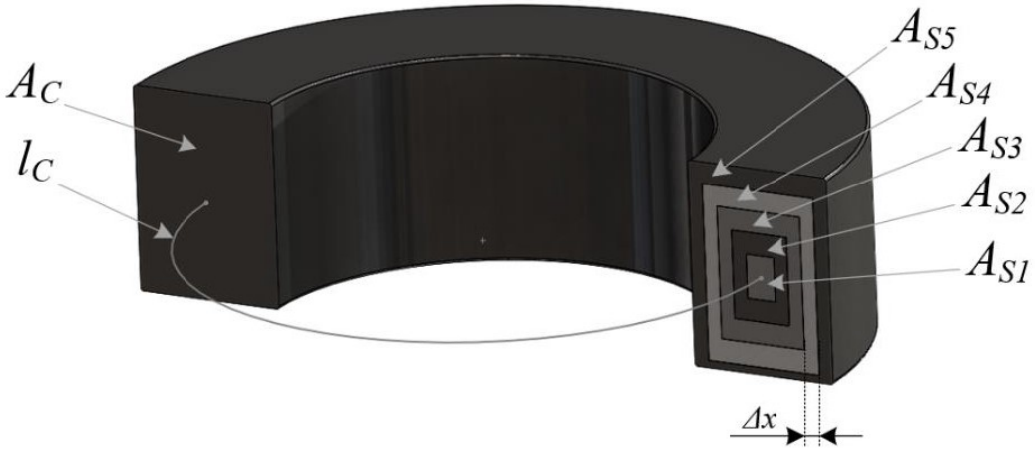


Figure 75. Magnetic core conceptually divided into five concentric shells.

Concentric shells, adequately small in size, can precisely reproduce unequal magnetic flux distributions due to the core skin and dimensional-resonance effects. The transmission line schematic is shown in Figure 76. The core elements are modeled by means of a network of series inductance $L_{1\text{-}n}$ and resistance $R_{1\text{-}n}$ per shell with shunt capacitance $C_{2\text{-}n}$ and resistance $R_{2\text{-}n}$. The RLRC network is combined into the lumped section of the transmission line.

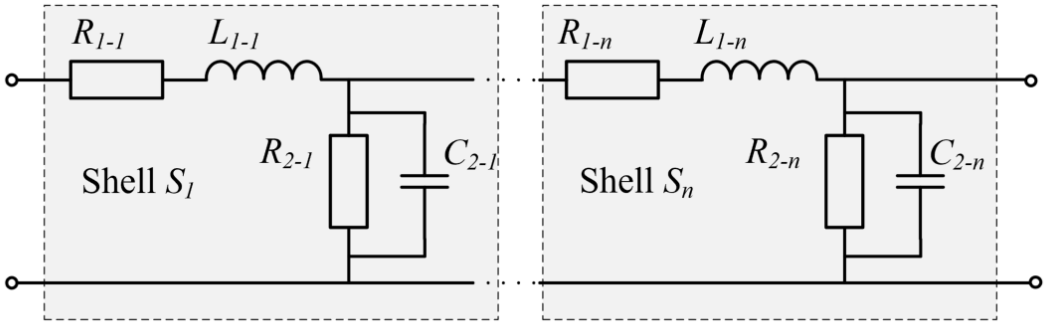


Figure 76. Schematic of the core transmission line model.

The TLM parameters are related to the core geometry as follows [58]:

$$L_0 = \frac{\mu_0 N^2 A_c}{l_c} \tag{3.3}$$

$$R_{1-n} = \mu'' L_0 \omega \left(\frac{A_{sn}}{A_c}\right) \tag{3.4}$$

$$L_{1-n} = \mu' L_0 \left(\frac{A_{sn}}{A_c}\right) \tag{3.5}$$

$$R_{2-n} = \frac{l_{sn}}{\varepsilon'' \varepsilon_0 \omega l_c \Delta x} \tag{3.6}$$

$$C_{2-n} = \frac{\varepsilon' \varepsilon_0 l_c \Delta x}{l_{sn}} \tag{3.7}$$

where A_{sn} is the cross-sectional area of the shell n, A_c is the entire core cross section, l_{sn} is the shell mean path length, l_c is the magnetic core path length, n is the shell number, and Δx is the shell thickness.

The transmission line model uses a magnetic core modeled by concentric shells. The number of shells is related to the model accuracy: the higher the number of shells, the better the calculation accuracy. The TLM accuracy for a T50 core of 3F36 material at a frequency range up to 10 MHz for various number of shells is shown in Figure 77.

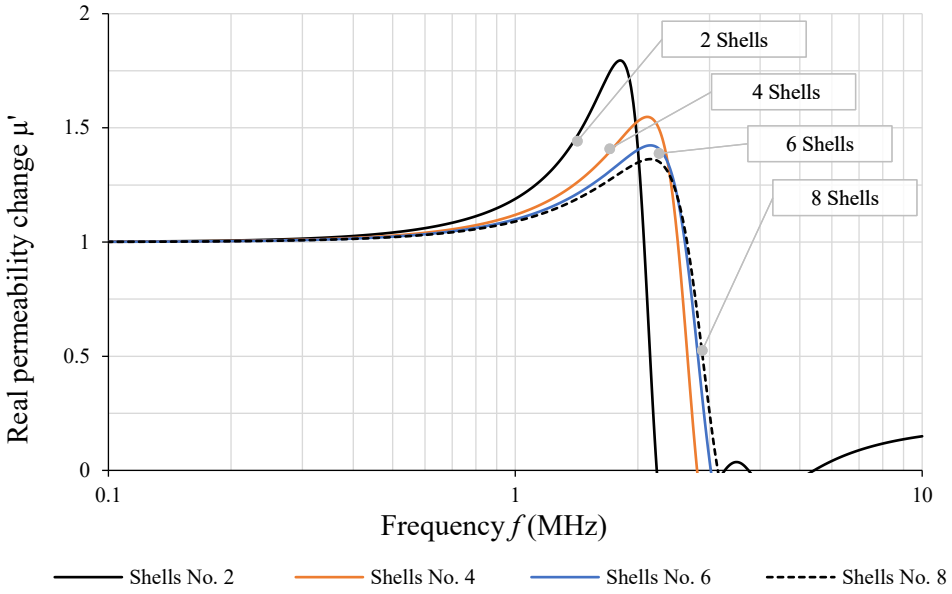


Figure 77. Calculated normalized permeability vs. frequency for T50 3F36 ferrite core for variable shell number.

The effect of the number of shells on the calculated permeability is shown in Figure 77, while the average relative error is shown in Figure 78. The average error is calculated with reference to the permeability characteristic calculated for fifty shells. Further number of shells increase does not results in error decrease. Each material and core size required an individual approach to the shell number selection, and the number of shells is increased until the relevant average error is achieved.

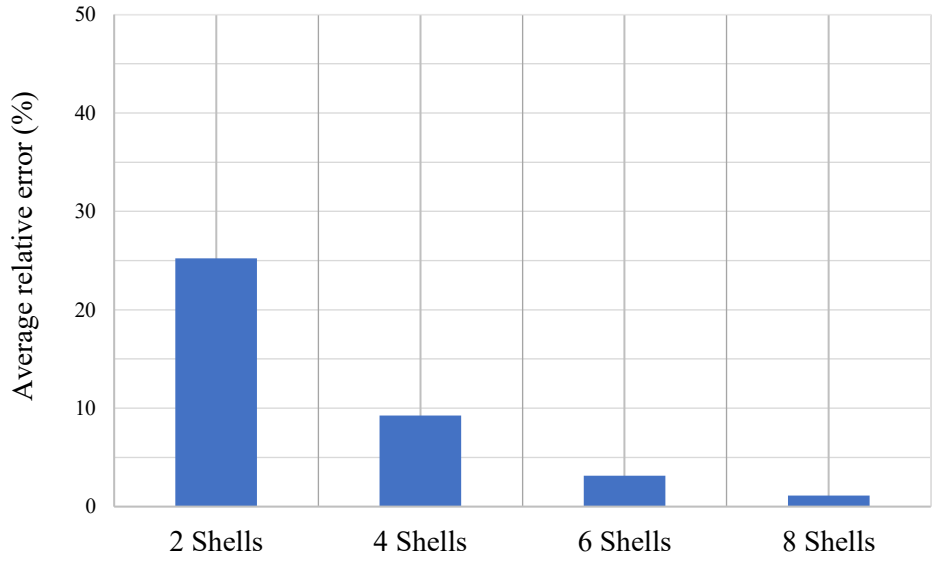


Figure 78. Average relative error vs. number of shells for 3F36 T50 ferrite core.

3.3.2 Results

As part of the first phase, the TLM is used to model the field distribution in the T50 cores made of two ferrite materials: 3F36 and 3E10. The calculated real and imaginary permeability for the 3F36 T50 core is shown in Figure 79 and Figure 80, respectively and plotted vs. frequency and shell number. The T50 core is arbitrarily divided into five concentric shells. Just as in the case of 1-D modeling, the results of each section are normalized to the initial permeability for real permeability, and to the maximum value for imaginary permeability.

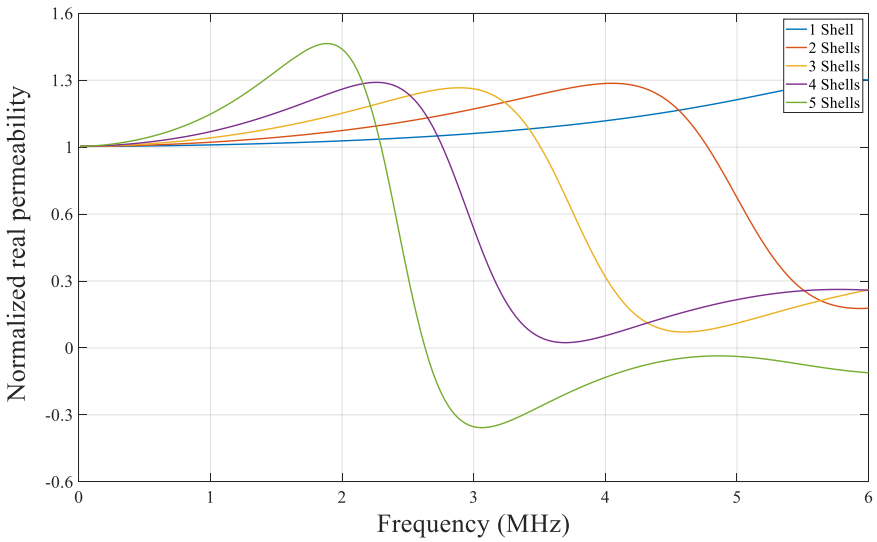


Figure 79. Calculated normalized real permeability for a T50 core of 3F36 material.

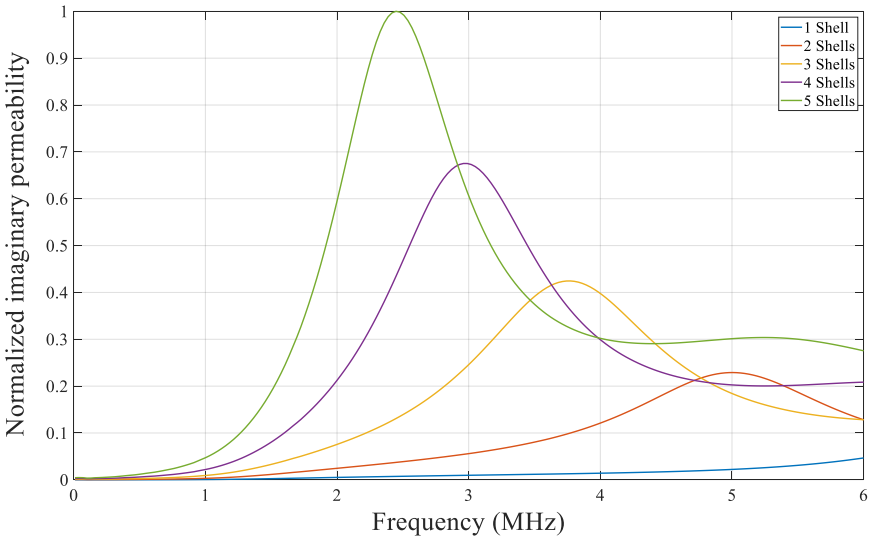


Figure 80. Calculated normalized imaginary permeability for a T50 core of 3F36 material.

As can be seen in the figures, the inner shell S_1 shows a stable complex permeability characteristic up to 6 MHz. The dimensions of this section are only 2 x 2.8 mm. As the shell number grows, the real permeability drops faster, while the peak of the imaginary permeability rises and then plummets.

In the second step, the TLM is used to model the field distribution in the T50 made of 3E10 material. The calculated real and imaginary permeability are shown in Figure 81 and Figure 82, respectively and plotted vs. frequency and shell number. The calculated characteristics for the T50 core are presented in exactly the same way as for the 3F36 material. The real permeability characteristic within the 3E10 ferrite core gradually decreases as the frequency increases. As the number of shells grows, the real permeability characteristic drops faster, while the peak of the imaginary permeability characteristic becomes more and more visible.

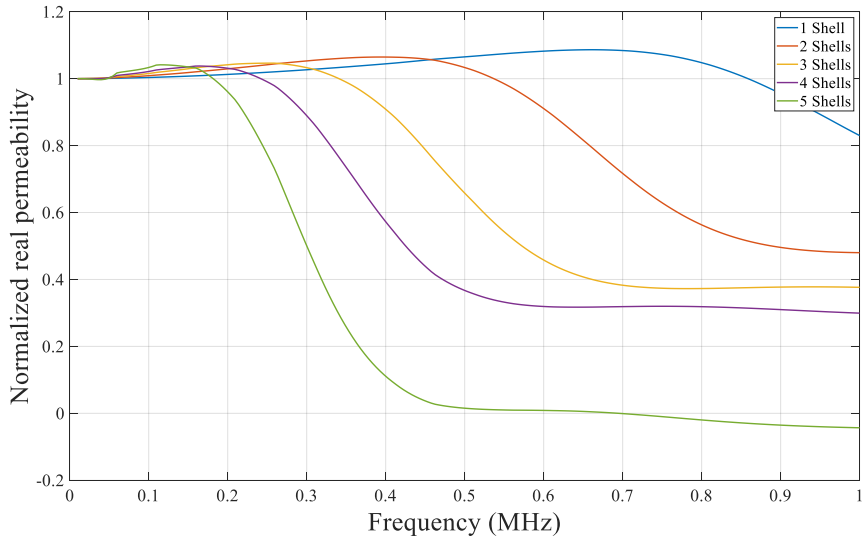


Figure 81. Calculated normalized real permeability for a T50 core of 3E10 material.

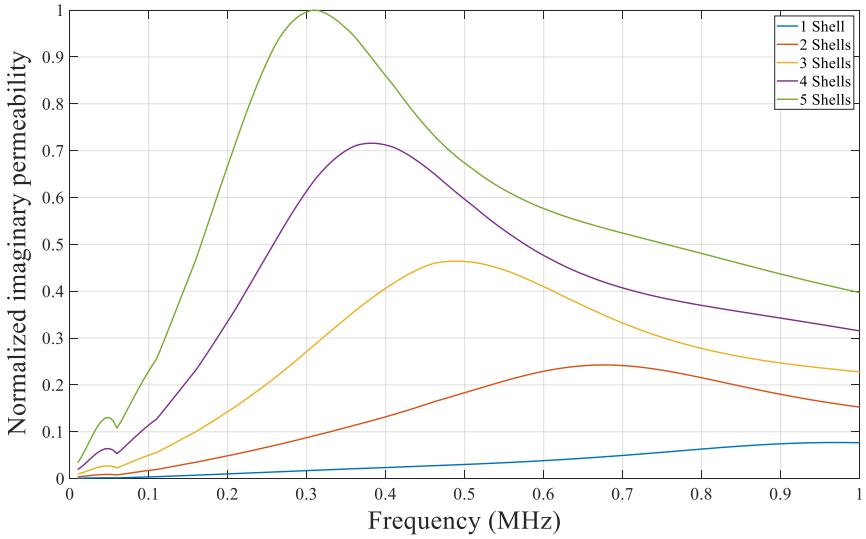


Figure 82. Calculated normalized imaginary permeability for a T50 core of 3E10 material.

3.3.3 Experimental validation

The transmission-line model is used to calculate the frequency-dependent permeability characteristics for the cores presented in Table 6. Each magnetic core was arbitrarily divided into fifteen concentric shells in order to minimize the calculation error. However, the shell number shall be determined individually for each material and core size by means of the accuracy error criterion as discussed in section 3.3.1. Generated complex permeability characteristics for 3F36 cores are shown in Figure 83 and Figure 84, while for the 3E10 cores they are shown in Figure 85 and Figure 86. The core transmission line model based on the complex material characteristics correlates well with the measured characteristic. The relative accuracy of +/- 5 % is achieved for the T50 and T29 cores, made of 3F36 material, when recreating the real permeability measured characteristic. The peak of the imaginary permeability characteristics is also well represented; however, oscillations are visible when the calculated characteristics drop to 30 % of the peak value. For the 3E10 material, the best representations of the real and complex permeability characteristics are achieved for the T29 core. The shape pf the cross-sectional area of the cores does not have a negative impact on the core's transmission line model accuracy as in the 1-D model.

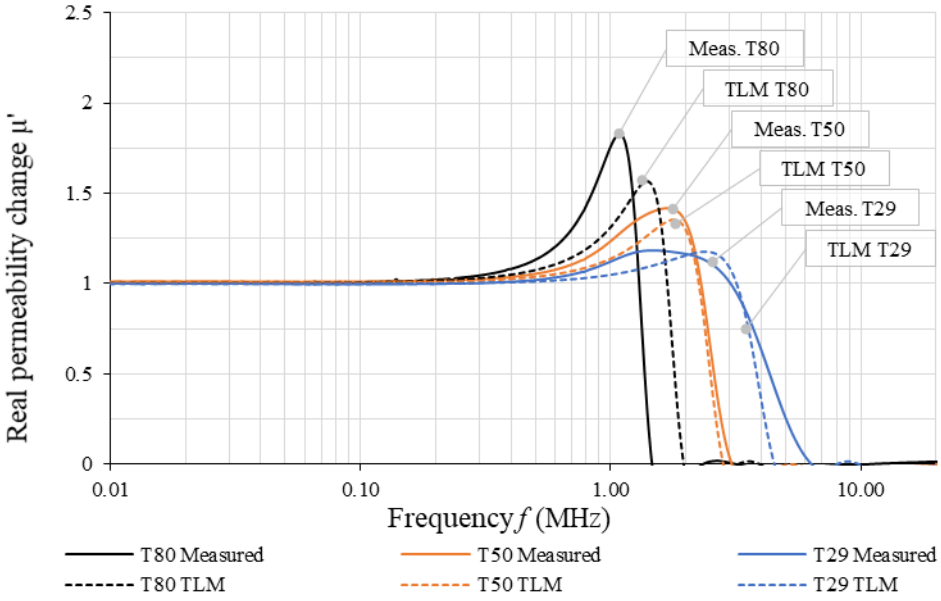


Figure 83. TLM calculated and measured normalized real permeability vs. frequency for 3F36 ferrite cores.

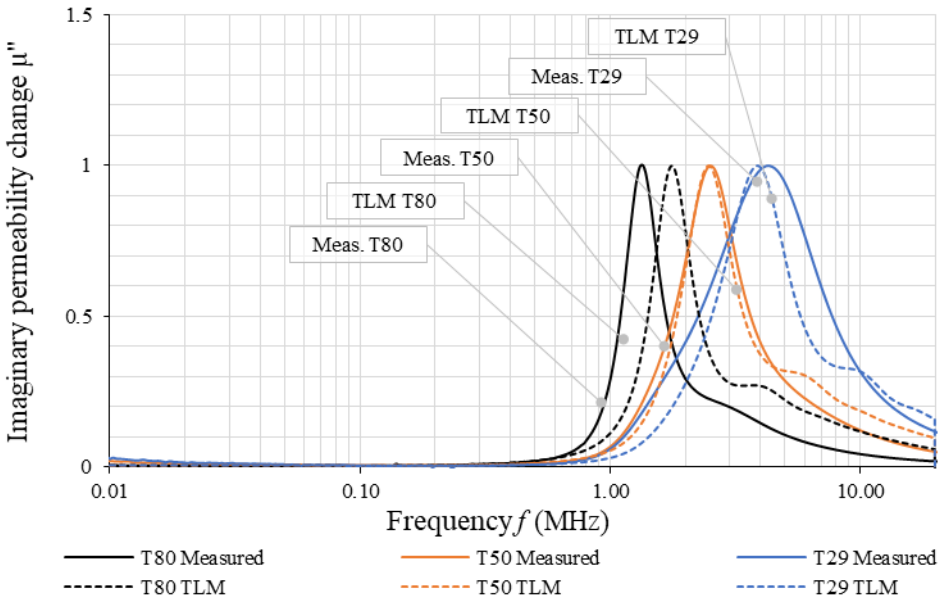


Figure 84. TLM calculated and measured normalized imaginary permeability vs. frequency for 3F36 ferrite cores.

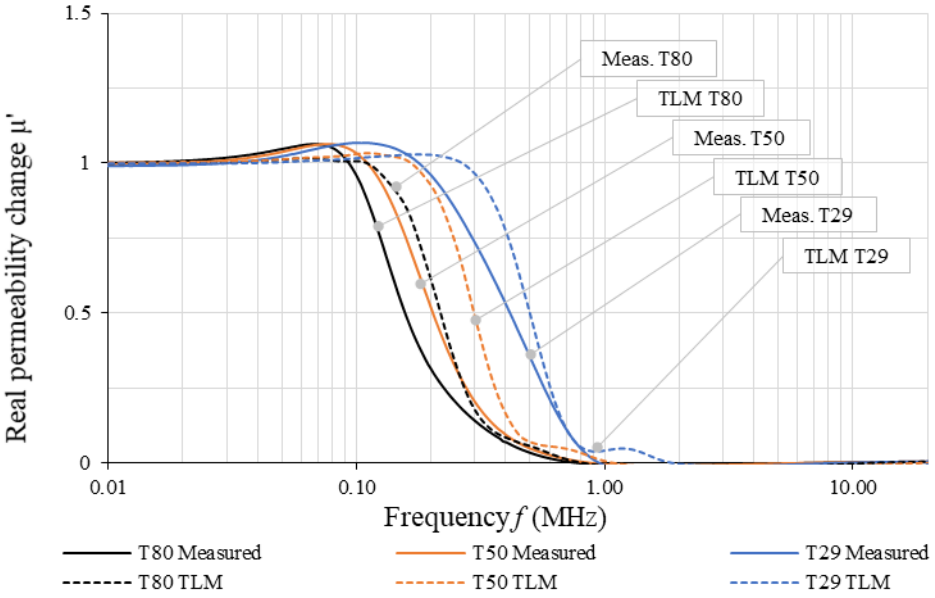


Figure 85. TLM calculated and measured normalized real permeability vs. frequency for 3E10 ferrite cores.

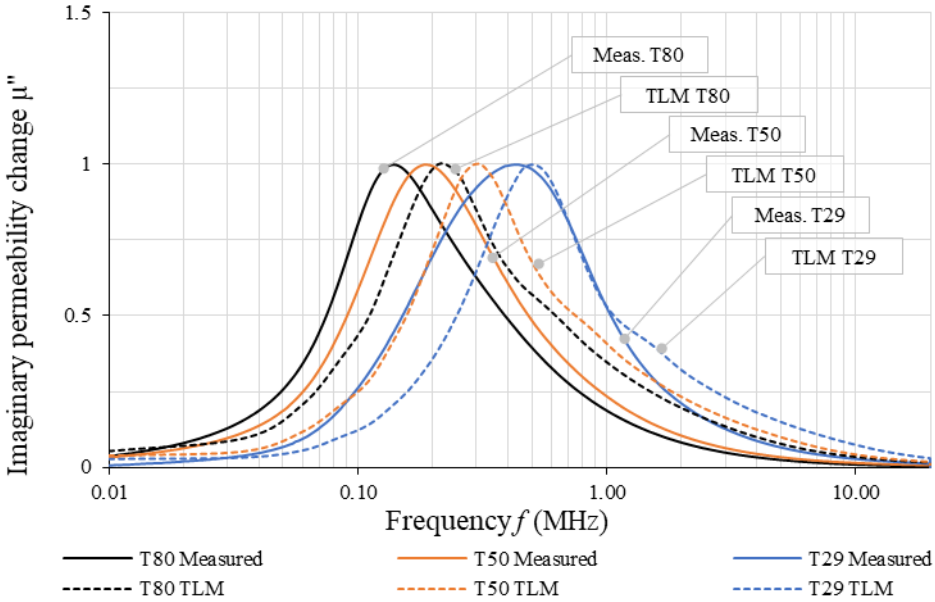


Figure 86. TLM calculated and measured normalized imaginary permeability vs. frequency for 3E10 ferrite cores.

3.3.4 Conclusions

The shell-based transmission-line model is based on a sectioned magnetic core. It was shown that concentric shells, adequately small in size, can precisely reproduce unequal magnetic flux distributions. Calculated characteristics were compared with experimentally measured core characteristics. The model shows a very good correlation with measurements. The peaks of the real and imaginary permeability characteristics are also well represented.

3.4 Magnetic core FEM modeling

The permeability vs. frequency characteristic does not provide any detailed information on the flux distribution in a ferrite core. The Finite Element Method (FEM) enables us to visualize the flux distribution in the core. An analysis is performed using the Maxwell 3D eddy-current field solver. The first simulation of the T50 core is performed for the 3F36 material at 1.7 MHz, as shown in Figure 87. A large amplitude flux is concentrated in the inner part of the core's cross section for the 3F36 material as a result of the dimensional resonance.

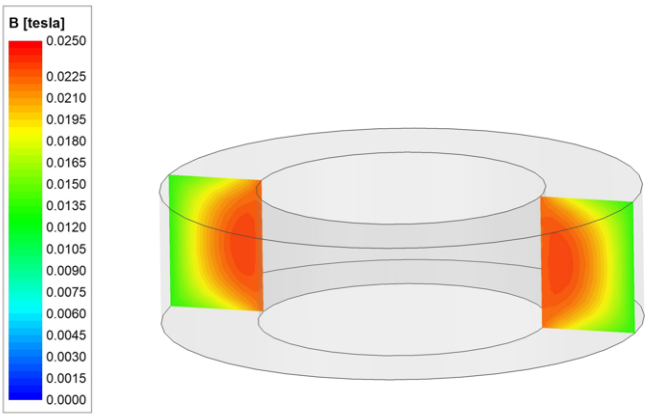


Figure 87. FEA results of RMS magnetic flux distribution in the T50, 3F36 ferrite core at 1.7 MHz.

In the second simulation, the 3E10 material is selected, and the magnetic flux distribution at 0.3 MHz is shown in Figure 88. The magnetic flux density distribution has an analogy to the current distribution in a conductor. The magnetic flux is concentrated in the outer circumference while the core center exhibits flux density weakening. In the inner part of the core, the magnetic flux flows in an opposite direction.

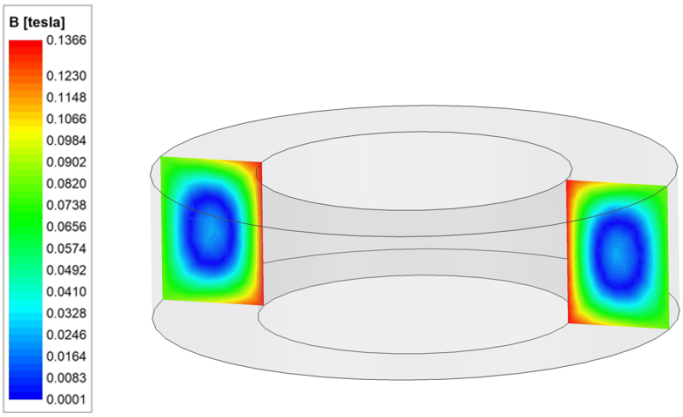


Figure 88. FEA results of RMS magnetic flux distribution in the T50, 3E10 ferrite core at 0.3 MHz.

3.4.1 Experimental validation

Maxwell 3D is used to calculate the frequency dependent permeability characteristics for the cores presented in Table 6. As discussed earlier in Section 3.2, the normalized real values of the resultant simulated magnetic permeability characteristic are compared with the normalized experimentally determined complex permeability characteristic. The generated complex permeability characteristics for 3F36 cores are shown in Figure 89 and Figure 90, while the characteristics for the 3E10 cores are shown in Figure 91 and Figure 92.

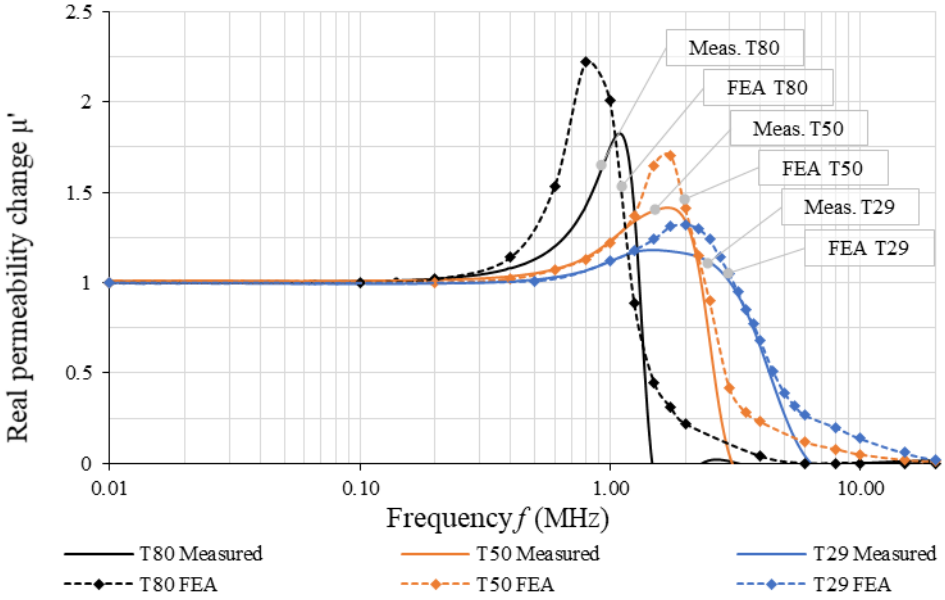


Figure 89. FEM simulated and measured normalized real permeability vs. frequency for 3F36 ferrite cores.

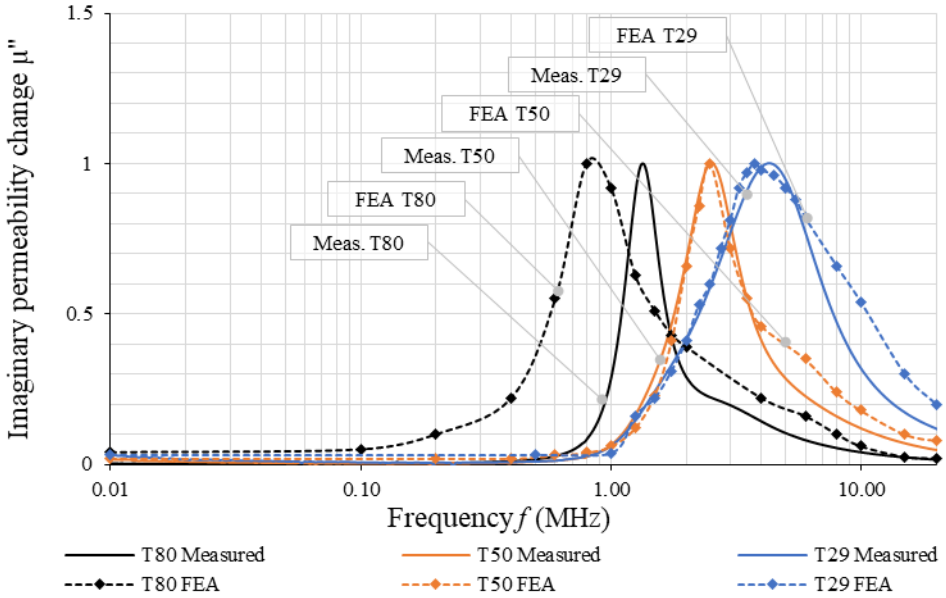


Figure 90. FEM simulated and measured normalized imaginary permeability vs. frequency for 3F36 ferrite cores.

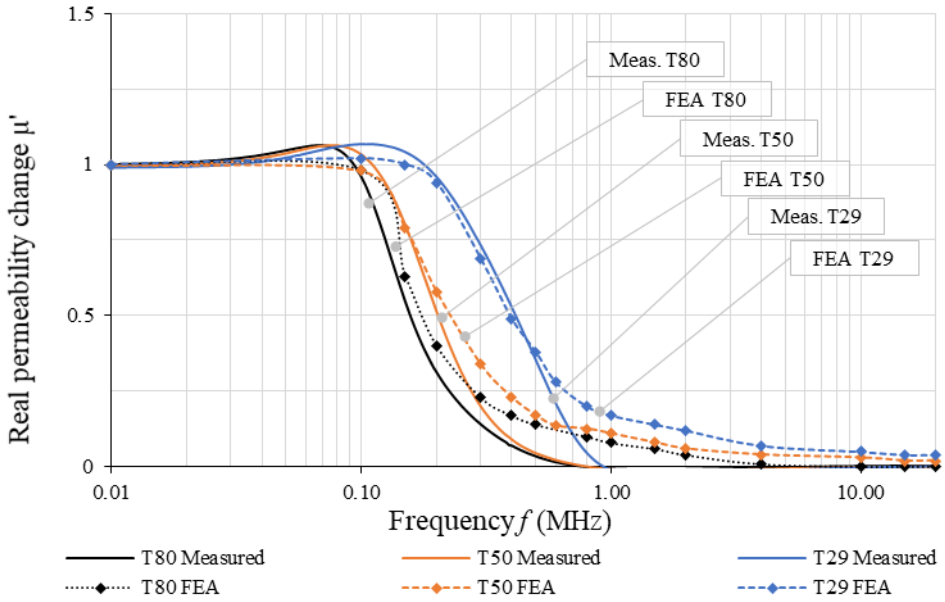


Figure 91. FEM simulated and measured normalized real permeability vs. frequency for 3E10 ferrite cores.

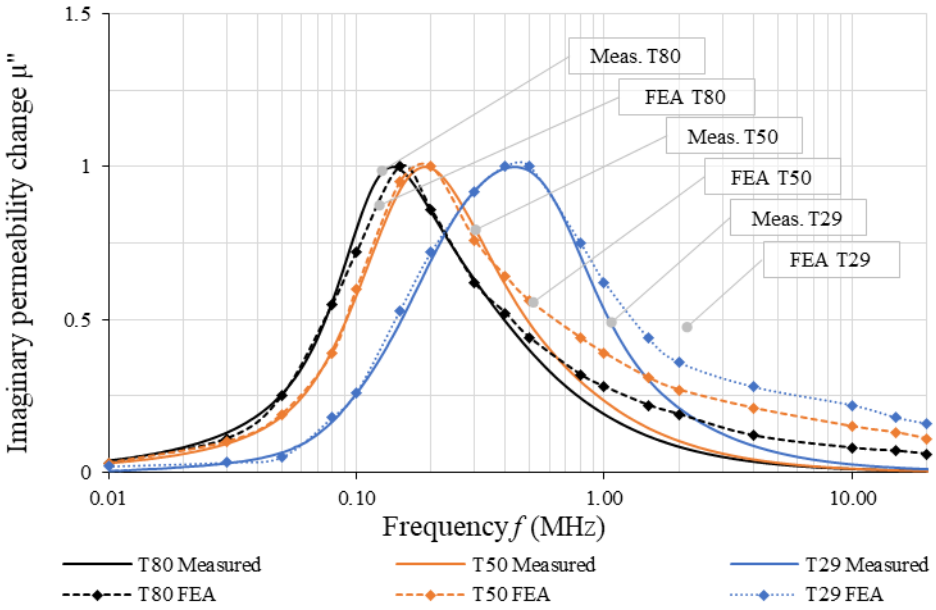


Figure 92. FEM simulated and measured normalized imaginary permeability vs. frequency for 3E10 ferrite cores.

As can be seen from the plots, the simulated complex permeability accords with the measurements. An exact match is achieved at low frequencies for all simulated cores and materials. The real permeability characteristic drop is well reproduced with a relative accuracy of +/- 2 %. The imaginary permeability characteristics are also accurately represented, except for the T80 core, made of 3F36 material, where the simulated characteristic is shifted in relation to the measurements. The core frequency characteristics are interpolated based on 18 points from the simulation. Discrepancies in the characteristics emerge at high frequencies. The simulated complex characteristic, regardless of material and core size, slowly decreases as the frequency increases. Improvement may be achieved if the software is changed from Maxwell 3D to HFSS [61], as it is the frequency range where the wave effect may dominate the flux distribution.

3.5 Practical aspects of experimental and analytical approaches

A comparison of the three methods for magnetic flux analysis, based on the 1-D analytical equation, the circuit transmission-line model, and the FEM for the 3F36 T50 core is shown in Figure 93. The analysis show a good accuracy in relation to the measurements. The calculated permeability characteristics, based on the methods presented, show permeability peaks at the same frequency as the measurements in most cases. However, the calculated permeability peak, based on the FEM model, is about 20% higher than the measured one. The calculated permeability characteristic, based on the transmission line model, is 8% lower at

the frequency range between 1 and 1.8 MHz in relation to the measurement, but shows the best overall correlation.

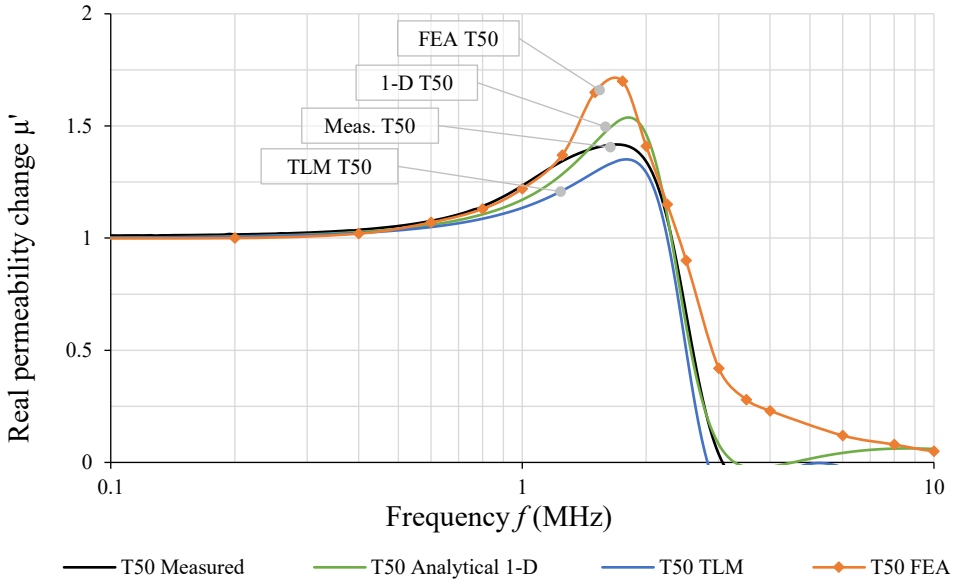


Figure 93. Calculated and measured normalized real permeability vs. frequency for 3F36 T50 ferrite core.

Selecting the right model by way of a comparison between the calculations and the measurements is challenging. Input data for each model constitutes a dataset of ferrite frequency characteristics based on the complex permeability and permittivity presented in section 2. Owing to the nature of the magnetic material, the complex permeability and permittivity parameters may vary with a tolerance of ± 20%. It was assumed during the calculations that the input material characteristics are nominal for all the tested materials. However, the material data for the reference core presented in Table 8 is unknown and cannot be extracted without a significant error. Therefore, the TLM model was used to calculate the tolerance envelope of the real permeability characteristic for the 3F36 T50 core. Results are shown in Figure 94. The envelope outlines the absolute worst case of all possible combinations of the material parameters without factoring in the probability of the occurrence. The measured and the analytical and TLM-related characteristics are within the envelope. Therefore, these models may be considered a good indicator of the high-frequency effects in the ferrite core. Four boundaries can be distinguished on the real permeability envelope in case of the T50 core. Boundaries number one and two represent the real permeability characteristic peak. The highest peak is achieved for the material with the highest real permeability and permittivity in combination with the lowest losses represented by imaginary components. The lowest peak is achieved through opposite material properties; the lowest permeability and permittivity

combined with the highest loss. Boundaries number three and four represent a characteristic shift. The lower the complex characteristic of the material, the more stable the real permeability characteristic is. If the core is made from a material in its upper limit of tolerance, the characteristic drops at lower frequencies.

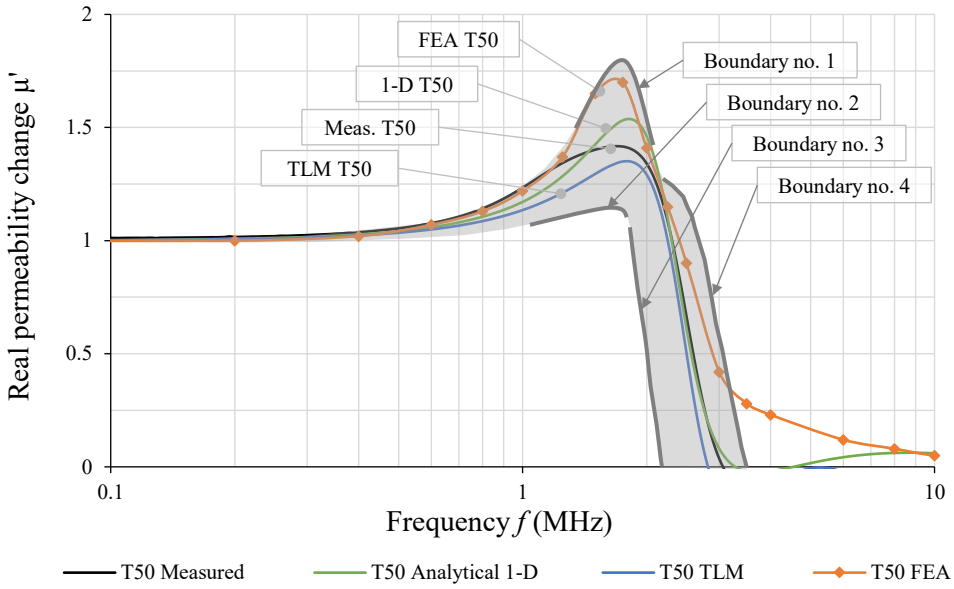


Figure 94. Calculated and measured normalized real permeability vs. frequency for 3F36 T50 ferrite core including tolerance analysis.

3.5.1 Calculation error

Four simple types of errors are now calculated to assess the quality of the each discussed model, as shown in Table 7. The first error is calculated by comparing the calculated and experimental real permeabilities at 10 kHz. The second error is calculated by comparing the modeled and experimental real permeabilities at 500 kHz for 3F36 and 50 kHz for 3E10, frequencies where we see the high-frequency effects beginning to impact. The third error compares the peak real permeability values. The fourth error is calculated by comparing the modeled and experimental frequencies at peak real permeability.

TABLE 7. MODEL ERRORS.

	Material	T80	T50	T29	T80	T50	T29	T80	T50	T29
		1-D analytic model			TLM model			FEA model		
Calculated permeability at 10 kHz	3F36	1593	1592	1587	1593	1696	1638	1603	1610	1586
Measured permeability at 10 kHz	3F36	1600	1600	1600	1600	600	600	600	600	600
Error at 10 kHz	3F36	-0.40 %	-0.50 %	-0.80 %	-0.44 %	1.97 %	2.39 %	0.20 %	0.60 %	-0.90 %
Calculated permeability at 500 kHz	3F36	1925	1701	1628	1691	1742	1650	2069	1667	1792
Measured permeability at 500 kHz	3F36	1814	1689	1632	1814	1689	1632	1814	1689	1632
Error at 500 kHz	3F36	6.14 %	0.73 %	-0.29 %	-6.74 %	3.15 %	1.09 %	14.1 %	-1.28 %	9.77 %
Calculated permeability at peak	3F36	3544	2832	2163	2813	2594	1911	3712	2736	2112
Measured permeability at peak	3F36	2918	2268	1894	2918	2268	1894	2918	2268	1894
Error at peak	3F36	21.4 %	24.8 %	14.2 %	-3.59 %	14.3 %	0.94 %	27.2 %	20.6 %	11.5 %
Calculated peak frequency (MHz)	3F36	1.114	1.767	2.821	1.562	2.113	3.214	0.900	1.600	2.000
Measured peak frequency (MHz)	3F36	1.072	1.725	2.095	1.072	1.725	2.095	1.072	1.725	2.095
Frequency error at peak	3F36	3.91 %	2.43 %	34.6 %	45.7 %	22.4 %	53.4 %	16.1 %	7.24 %	4.53 %
Calculated permeability at 10 kHz	3E10	10006	9957	9917	9990	10040	10080	10030	9950	9940
Measured permeability at 10 kHz	3E10	10000	10000	10000	10000	10000	10000	10000	10000	10000
Error at 10 kHz	3E10	0.06 %	-0.43 %	-0.83 %	-0.10 %	0.40 %	0.80 %	0.30 %	-0.50 %	-0.60 %
Calculated permeability at 50 kHz	3E10	10133	10217	10121	10080	10159	10081	10120	10010	9960
Measured permeability at 50 kHz	3E10	10478	10381	10253	10478	10381	10253	10478	10381	10253
Error at 50 kHz	3E10	-3.29 %	-1.58 %	-1.29 %	-3.79 %	-2.13 %	-1.67 %	-3.41 %	-3.57 %	-2.85 %
Calculated permeability at peak	3E10	10137	10523	10830	10080	10446	10759	10150	10090	10040
Measured permeability at peak	3E10	10633	10640	10693	10633	10640	10693	10633	10640	10693
Error at peak	3E10	-4.65 %	-1.09 %	1.28 %	-5.19 %	-1.82 %	0.61 %	-4.53 %	-5.16 %	-6.10 %
Calculated peak frequency (kHz)	3E10	52.180	99.320	183.63	54.661	111.72	235.78	60.000	70.000	125.00
Measured peak frequency (kHz)	3E10	69.218	78.760	112.34	69.218	78.760	112.34	69.218	78.760	112.34
Frequency error at peak	3E10	24.6 %	26.1 %	63.4 %	21.0 %	41.8 %	109 %	13.3 %	11.1 %	11.2 %

3.5.2 Calculation time

One additional aspect of the methods discussed is the calculation time. Table 8 shows the calculation time necessary to generate the real permeability characteristic for the T50 core, made of the 3F36 material. The calculation time is the lowest for the TLM method, while the highest for the FEM method. Almost two days are needed for a single FEM calculation. The basis of the comparison is a workstation equipped with Intel Xeon W-2133 3.6 2666 MHz 6C CPU and 64 GB DDR4.

TABLE 8. CPU TIME FOR CALCULATION T50, 3F36 FERRITE CORE REAL PERMEABILITY CHARACTERISTIC.

Analysis type	Number of points on characteristic	Calculation time
1-D analytical	800	5.1 s
TLM	800	3.8 s
FEM	18	43.5 h

3.6 Conclusions

High-frequency effects, such as the dimensional resonance and the skin effect within the core can be modelled and predicted based on the aforementioned models. These models are used to investigate the skin depth and the dimensional resonance. In addition, the clear impact of these phenomena can be observed in various materials and core sizes. Each method has its strengths and weaknesses; however, taking into account the calculation time, the TLM method should be further developed in order to reduce the calculation error, and raise the possibilities of visualising the flux distribution in the core. The TLM method is easily incorporated into a simulation of a higher-order system which can significantly improve the EMC simulation of the entire power converter.

4 NOVEL EXPERIMENTAL VALIDATION OF FLUX DISTRIBUTION IN A FERRITE CORE

Abstract - This chapter presents the novel method developed for the experimental validation of the magnetic flux distribution in ferrite cores. The complex permeability characteristic discussed in earlier chapters provides information on the core's overall performance without any details on the flux pattern. To date, only the FEM calculations have been able to visualize the flux distribution in the core. The purpose of this investigation is to verify the FEM flux pattern. Experimental data compares and contrasts various effects such as the dimensional resonance, the skin effect and the core's geometry. The experimental flux verification is based on a precisely bored ferrite core. During the experiment, sense windings are inserted into the bored holes to determine the flux and phase shift of each of the core segments.

Section 4.1 introduces two verification methods intended for a detailed analysis of the magnetic flux distribution. Section 4.2 shows the results of the magnetic flux distribution based on a simplified two-shell method. Section 4.3 discusses the magnetic flux distribution based on the more accurate four- shell method. A brief conclusion is presented in Section 4.4.

The results of this chapter have been published in the following papers and presentations:

- M. Kacki, M.S. Rylko, E. Herbert, "PSMA-SMA Special Project – Phase I, Investigation on Magnetic Flux Propagation in Ferrite Cores", *The Power Source Manufacturers Association Technical Report*, 2018.
- M. Kacki, M.S. Rylko, E. Herbert, J.G. Hayes, C.R. Sullivan, "A Study of Flux Distribution and Impedance in Solid and Laminar Ferrite Cores," *IEEE Applied Power Electronic Conference and Exposition (APEC)*, Anaheim, CA, 2019.
- M. Kacki, M.S. Rylko, E. Herbert, "PSMA-SMA Special Project – Phase II, Investigation on Magnetic Flux Propagation in Ferrite Cores", *The Power Source Manufacturers Association Technical Report*, 2020.
- M. Kacki, M.S. Rylko, J.G. Hayes, C.R. Sullivan, "Analysis and Experimental Investigation of High-frequency Magnetic Flux Distribution in Mn-Zn Ferrite Cores," *IEEE Transactions on Power Electronics* (Early Access), August, 2022.

4.1 Introduction

The 1-D analytical model together with the TLM well represent the complex permeability frequency characteristics of the tested cores. The dimensional resonance and the skin effects have a clear and visible impact on the core performance. What is more, the FEM method renders the flux distribution within the ferrite core visible, thus exposing the source of the core's low performance at high frequencies. This chapter proposes an experimental method for validating the magnetic flux distribution in ferrite cores. The experimental validation of the flux distribution is the final confirmation of the presence of high frequency core effects such as the dimensional resonance and the skin effect [19]. Input material characteristics are the key parameters for the core's high frequency modelling. Therefore, the experimental validation of the flux distribution also constitutes the validation of the input data. Two verification methods are presented for a detailed analysis of the magnetic flux distribution: the simplified one, and one based on four shells drilling the core. In addition, the results are intended for laying the foundations for further discussion to introduce a standardized testing procedures for magnetic cores [63].

4.2 Verification of T50 flux distribution – "two shells" core drilling scheme

4.2.1 Core preparation

For the sake of the first approach, two T50 ferrite cores, made of two materials: 3E10 and 3F36, are selected to validate the analytical calculations and FEM results for the flux distribution. Detailed dimensions of the cores are presented in Table 9.

TABLE 9. CORE PARAMETERS USED FOR FLUX DISTRIBUTION VERIFICATION – TWO SHELLS

Core type	Core material	Dimensions OD x ID x H	Core cross section dimension	Core cross section	Core volume
Unit	-	mm	mm	mm^2	cm^3
T50	3E10 3F36	50 x 30 x 14	10 x 14	140	17.59

In order to measure the magnetic flux, three sets of bores were made in the each selected core. One set of bores consists of two vertical bores and one horizontal bore of 0.65 mm diameter each, as shown in Figure 95.

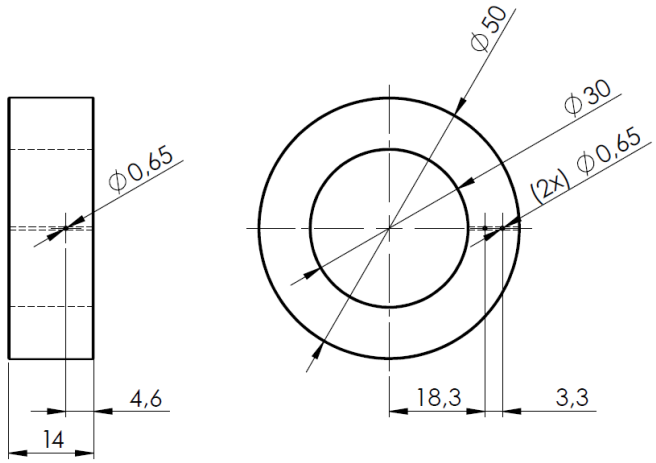


Figure 95. T50 drilled core dimensions.

Two vertical bores and one horizontal divide the magnetic core into nine sections as shown in Figure 96. During the experiment, the main source winding encloses the entire core while the sense windings are inserted into the bored holes to determine the flux and the phase shift of each of the core segments. It is assumed that the flux distribution is symmetrical within the core, therefore the flux measured in the sections S_5, S_6, and S_7 is equal to the flux described in the section S_3, S_2, as well as S_1. In order to facilitate the presentation of the results, the nine sections are grouped into two; the inner section A, which corresponds to the flux measured in section S_9, and the outer section B, which is the sum of the flux measured in sections from S_1 to S_8.



Figure 96. T50 core drilling scheme with section arrangements .

The measurement system setup and the winding arrangement are presented in Figure 97. The Agilent 33220A arbitrary waveform generator controls the amplifier AG 1017 L [64], which supplies the reference winding. The Tektronix oscilloscope DPD 3034 is used for data acquisition [48]. This test setup allows the cores to be tested at frequencies up to 1.5 MHz.

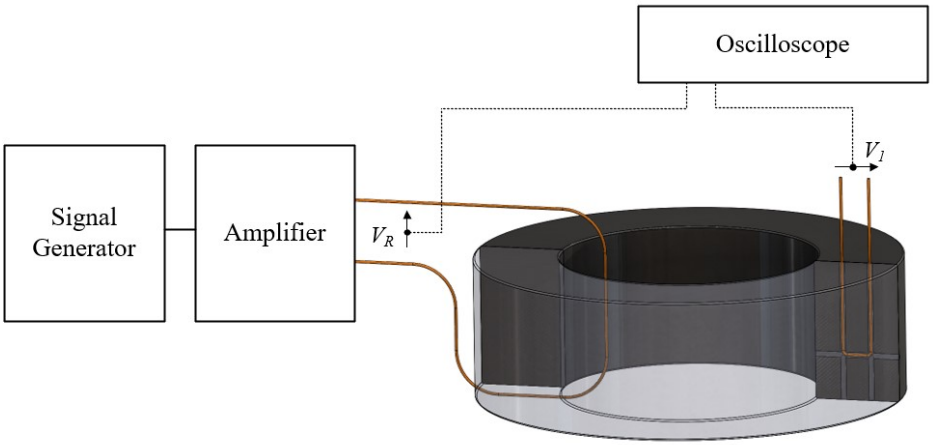


Figure 97. Measurements setup for magnetic flux distribution test.

The manner in which the flux of the section S_9 is defined is presented below. As many as four steps are needed to determine the flux density of section S_9. In the first and the second steps, voltages V_1 and V_2 are successively measured using the core configuration shown in Figure 98.

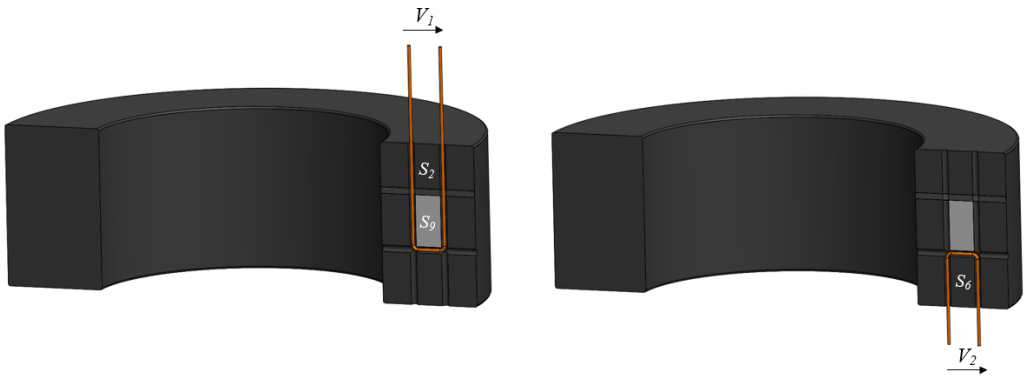


Figure 98. Winding configuration to measure voltage V_1 and V_2 .

In the third step, the voltage corresponding to section S_9 is achieved by subtracting V_2 from V_1. In the final step, the flux is calculated as a function of the sinusoidal voltage and frequency for $N = 1$ as follows:

$$V_{S9} = V_1 - V_2 = V_{1M}\, sin(\omega t + \varphi_1) - V_{2M}\, sin(\omega t + \varphi_2) \tag{4.1}$$

$$\Phi_{S9} = A_{S9} \cdot B_{S9} = A_{S9} \frac{V_{S9}}{2\pi f A_{S9}} = \frac{V_{S9}}{2\pi f} \tag{4.2}$$

where V_{S9} is the calculated voltage corresponding to section S_9, V_{1M} is the maximum value of the voltage measured for section S_1, φ_1 is the phase of the voltage measured for section S_1, V_{2M} is the maximum value of the voltage measured for section S_2, φ_2 is the phase of the voltage measured for section S_2, Φ_{S9} is the magnetic flux corresponding to section S_9, A_{S9} is the section S_9 cross-section, and B_{S9} is the magnetic flux density corresponding to section S_9.

The excitation voltage is changed for different frequencies to increase magnetic flux for higher frequencies. In order to eliminate the change in the obtained flux density, the flux density should be normalized by dividing by the main flux density at each frequency:

$$Magnetic\ flux\ density\ ratio(f) = \frac{B_A(f)}{B_{ALL}(f)} \tag{4.3}$$

where B_A is the magnetic flux density corresponding to section S_A, and B_{ALL} is the magnetic flux density corresponding to entire core.

4.2.2 Experimental validation

For the T50 core, made of 3E10 material, the magnetic flux density ratios for Sections A and B are shown in Figure 99, with the associated phase in Figure 100. As can be observed, the flux in the inner core part starts decreasing above 300 kHz, while the flux in the outer core part increases at the same time. The experimentally-obtained flux distributions confirm the analytical calculations and the FEM analysis. The magnetic flux is concentrated in the outer circumference while the core center exhibits flux density weakening. Magnetic cores made of 3E10 are dominated by the skin depth caused by the combination of high magnetic and electrical losses.

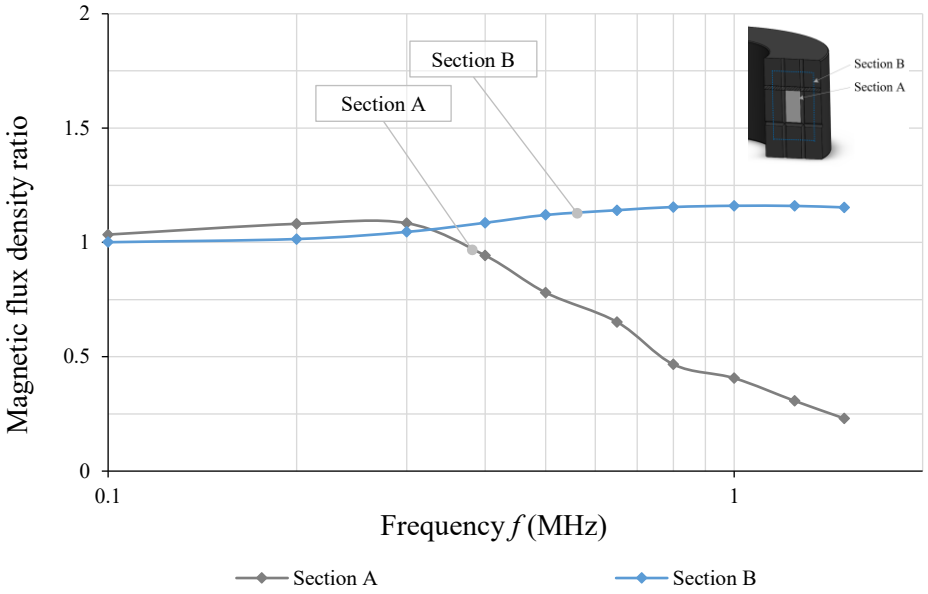


Figure 99. Magnetic flux density ratio in section A and B for 3E10 T50 core.

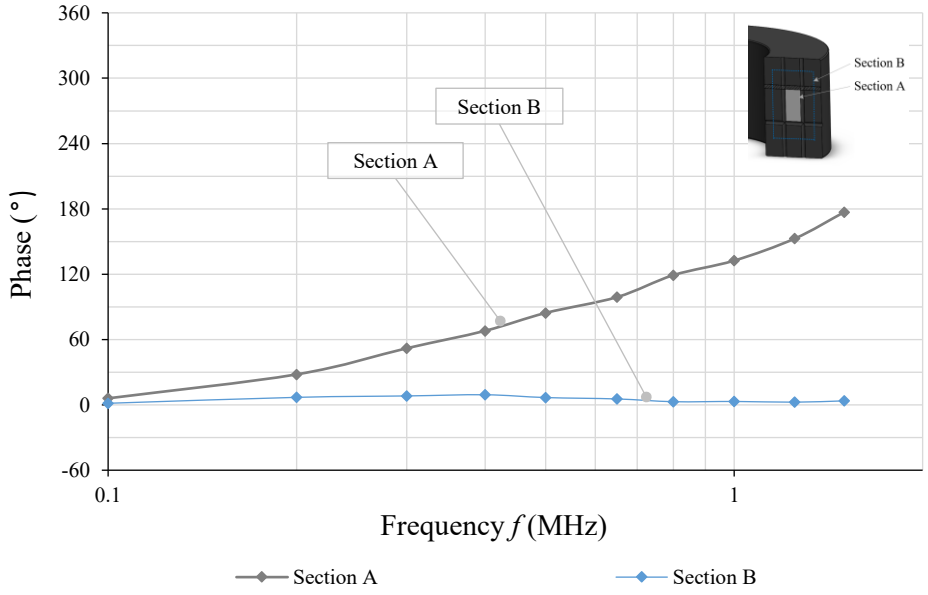
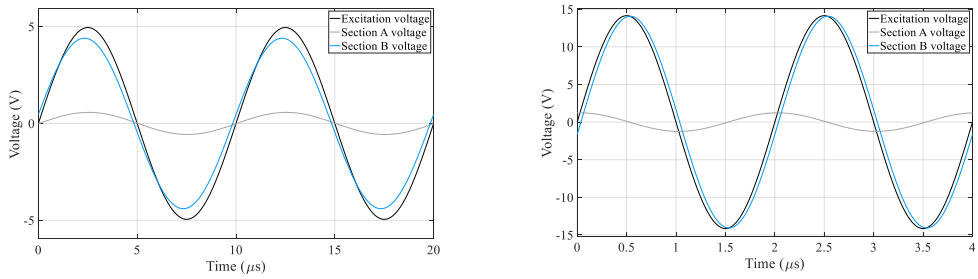


Figure 100. Phase in section A and B for 3E10 T50 core.

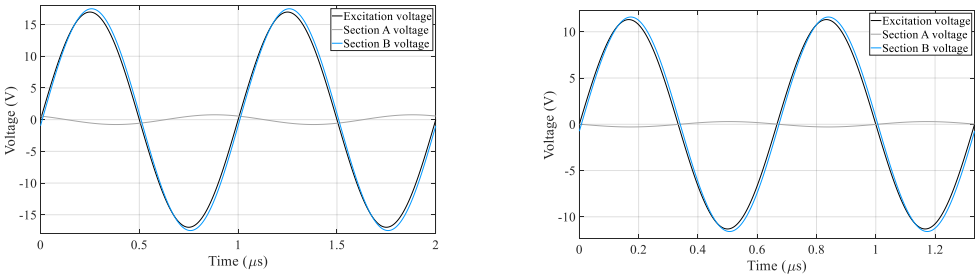
The corresponding voltage waveforms for the excitation in Section A and Section B for four selected frequencies 100 kHz, 500 kHz, 1 MHz and 1.5MHz are presented in Figure 101 and Figure 102. At 100 kHz both voltages for the section A and B, are in phase with the excitation voltage. As frequency increases, the phase shift for the inner core part also increases. At 1.5 MHz, the voltage representing the magnetic flux for inner core part is out of phase with

reference to the excitation voltage. In this core part, the magnetic flux flows in an opposite direction. As the frequency increases, the phase shift for the section B remains the same.



a) *b)*

Figure 101. Measured voltages for T50 3E10 core at (a) 100 kHz and (b) 500 kHz.



a) *b)*

Figure 102. Measured voltages for T50 3E10 core at (a) 1 MHz and (b) 1.5 MHz.

For the T50 core, made of 3F36 material, the magnetic flux density ratios for sections A and B are shown in Figure 103, with the associated phase in Figure 104. The magnetic flux in the inner core part starts increasing gradually with frequency, while the flux in the outer core part is stable at the same time. Also in this case, the experimentally obtained flux distribution confirms the analytical calculations and the FEM analysis. The flux is stronger and concentrated in the inner part of the core cross section. For the 3F36 material in the considered frequency range, the flux distribution is dominated by dimensional resonance. At higher frequencies, as the losses increase, the skin effect becomes visible in 3F36 T50 core as well.

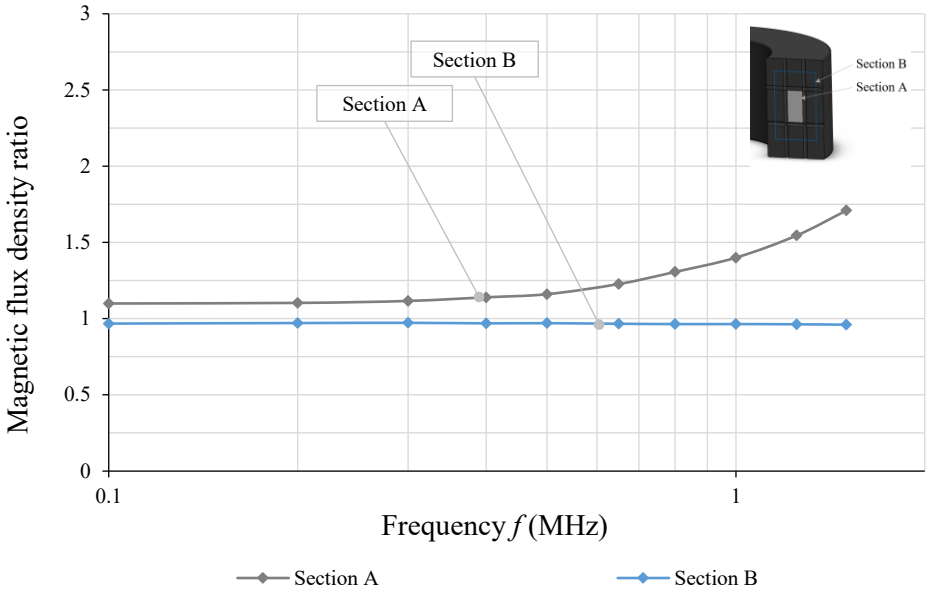


Figure 103. Magnetic flux density ratio in section A and B for 3F36 T50 core.

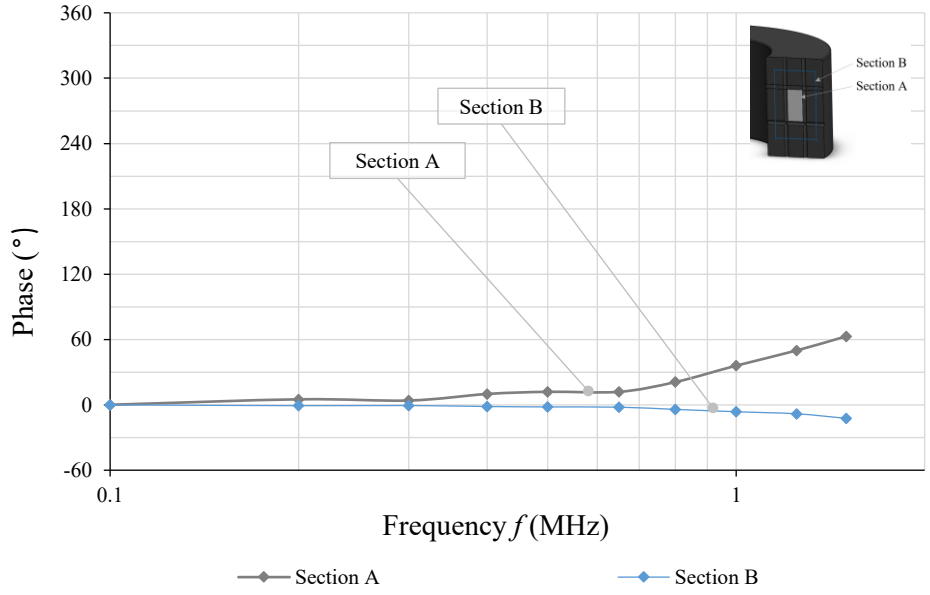
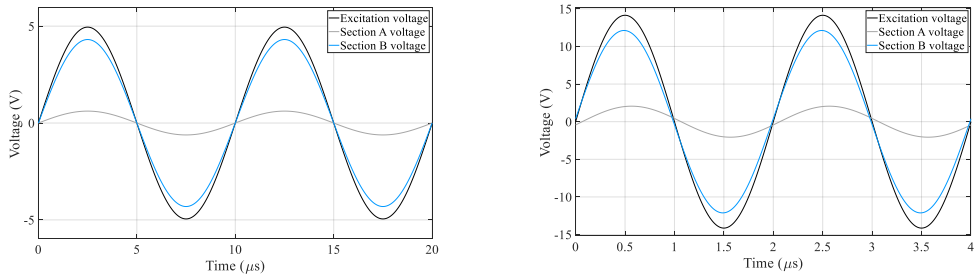


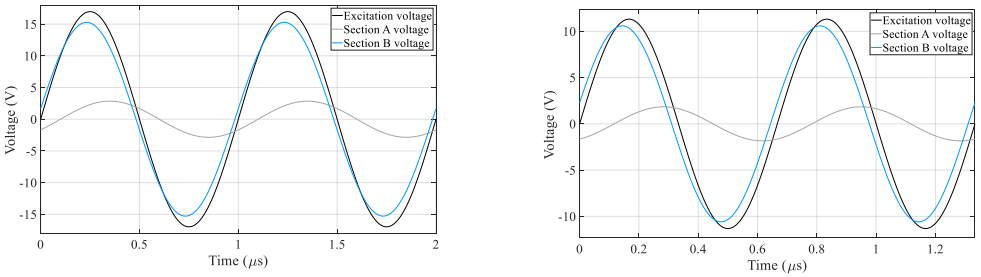
Figure 104. Phase in section A and B for 3F36 T50 core.

Corresponding voltage waveforms for the excitation in Section A and Section B for the four selected frequencies 100 kHz, 500 kHz, 1 MHz and 1.5MHz, are presented in Figure 105 and Figure 106. Voltage for Sections A and B are in phase with the excitation voltage at 100 kHz. At 500 kHz, 1 MHz and 1.5 MHz, the phase shift for Section B is constant and equal to 5°. At higher frequencies, the phase shift which refers to inner core part starts to increase.



a) *b)*

Figure 105. Measured voltages for T50 3F36 core at (a) 100 kHz and (b) 500 kHz.



a) *b)*

Figure 106. Measured voltages for T50 3F36 core at (a) 1 MHz and (b) 1.5 MHz.

4.3 Verification of the flux distribution – “four shells” core drilling scheme

4.3.1 Core preparation

The second method for flux verification is also based on bored holes. However, in order to increase measurement accuracy, the number of drilled holes is tripled. The flux distribution in the magnetic core is measured using a higher resolution. Simultaneously, besides the T50 cores, the flux distribution is measured in the T80 cores which shows skin and dimensional resonance effects at lower frequencies. Detailed core dimensions are presented in Table 10.

TABLE 10. CORE PARAMETERS USED FOR FLUX VERIFICATION

Core type	Core material	Dimensions OD x ID x H	Core cross section dimension	Core cross section	Core volume
Unit	-	mm	mm	mm^2	cm^3
T50	3E10 3F36	50 x 30 x 14	10 x 14	140	17.59
T80	3E10 3F36	80 x 45 x 17.5	17.5 x 17.5	306	60.13

Each tested core has three sets of bores, one set consists of two vertical, and one horizontal bore, each 0.65 mm at diameter. The drilled core is shown in Figure 107. Each bores set is shifted relative to each other to avoid reducing the core cross section.



Figure 107. Tested core with drilled three sets of holes.

Correct placement of sense winding is both time consuming and challenging. Therefore, the method used for the permanent sense winding placement is defined as follows. A thin auxiliary wire with a 0.05 mm diameter is inserted into each vertical bore. At the end of each auxiliary wire, a small loop is made. The wires are inserted into the bores until the loops are in line with the horizontal hole. The sense winding is threaded into the vertical bore and through all the loops from the previous step. Finally, the auxiliary wires which are inserted into the vertical holes are pulled out together with the sense winding. A tested core with a permanent sense winding is shown in Figure 108.

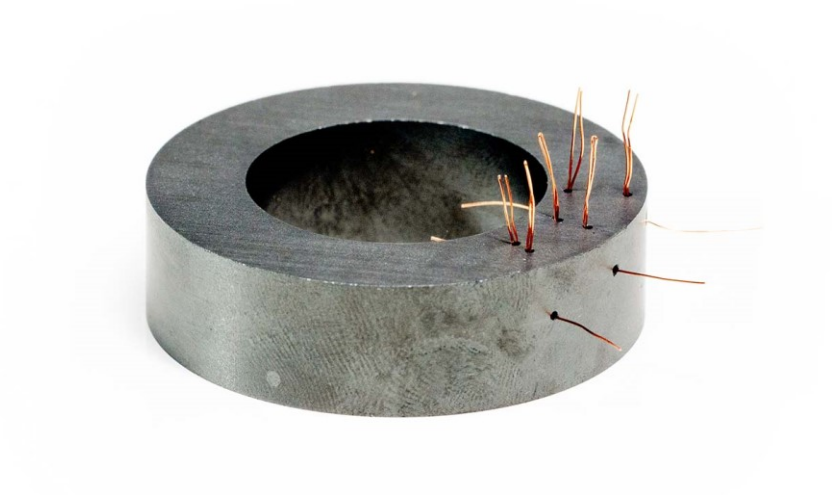


Figure 108. Tested core with sense winding.

With additional bores, the measured flux characteristic can be presented in four sections instead of two. Core sections are shown in Figure 109.

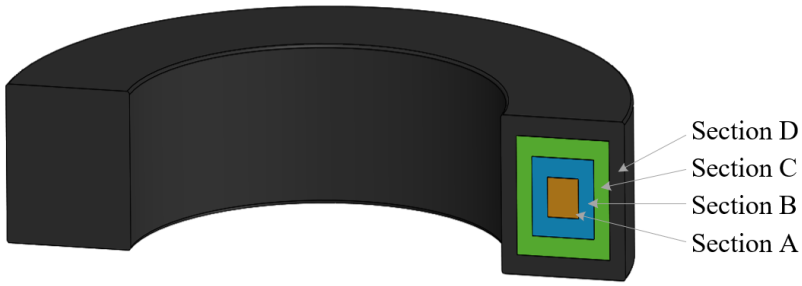


Figure 109. Section arrangement in tested cores based on the 4 shells drilling shame.

4.3.2 Experimental validation

The procedure for calculating the magnetic flux in the core is the same as for the previous tests. The normalized magnetic flux density distributions in each section of the T50 core, made of 3E10, at 1 MHz are shown in Figure 110. Similar to the previous results for the T50 core, the magnetic flux is concentrated in the outer part of the core, with the core center exhibits flux density weakening. It should be noted that the measurements show the averaged flux density for each region, and thus the effect of core reluctance cannot be shown.

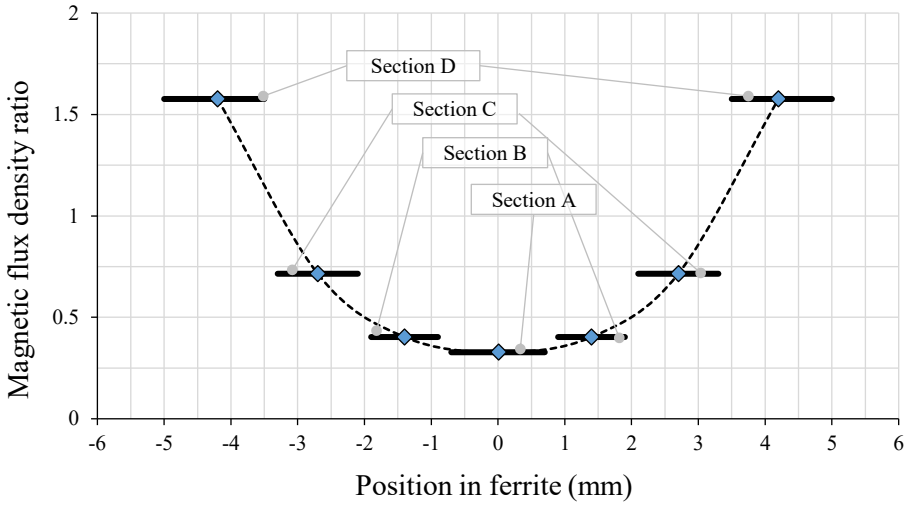


Figure 110. Magnetic flux density ratio in the each section for the 3F36 T50 core at 1 MHz.

In the next step, the magnetic flux distribution is presented for the frequency range of 50 kHz to 1.5 MHz. The four-shell core drilling scheme increases the measurement accuracy and allows for magnetic flux 3D representation. The results for the magnetic flux density change for the 3E10 cores are shown in Figure 111 and Figure 112, while the results for the 3F36 cores are shown in Figure 113 and Figure 114. The 3E10 material is more subject to the core skin effect, which results in a frequency-dependent non-uniform flux distribution. For both cores in the three internal sections, the flux decreases together with the frequency. For the outer Section A, the flux increases along with frequency. Similar to the complex permeability characteristics, the large T80 core is characterized by an early and dynamic flux density drop.

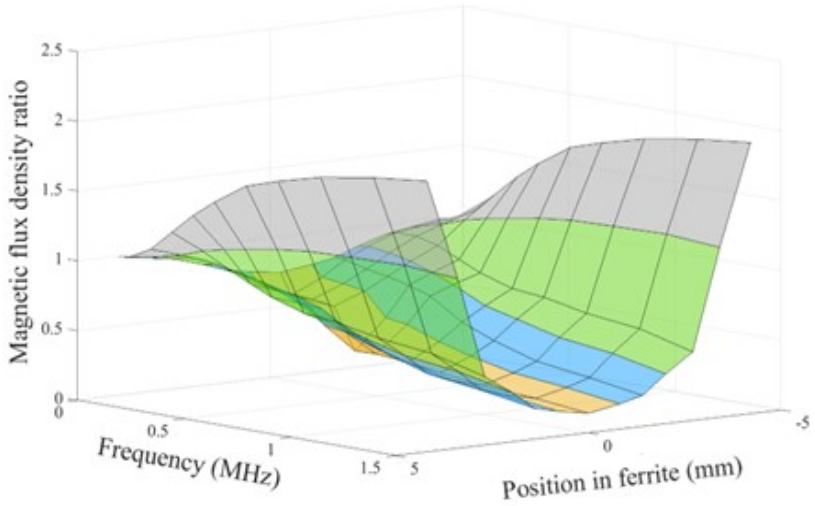


Figure 111. Magnetic flux density ratio in the each section for the 3E10 T50 core.

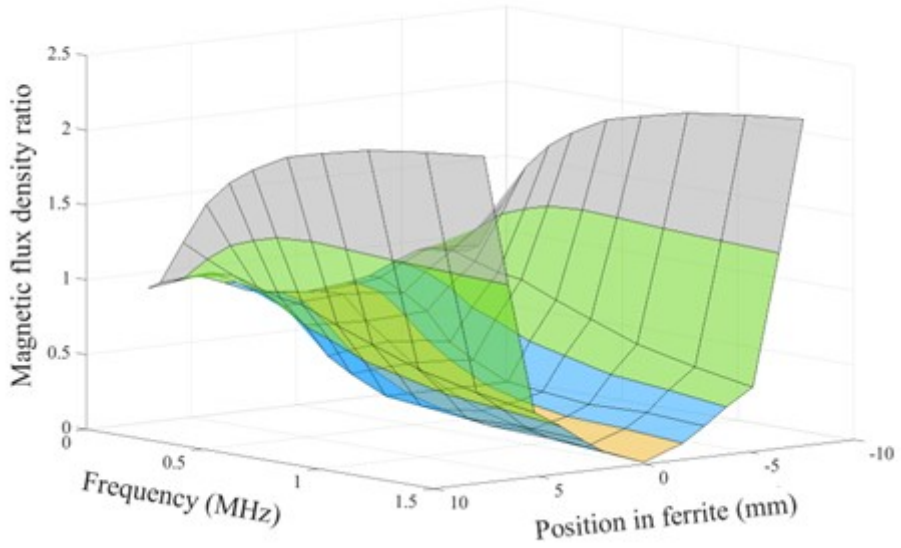


Figure 112. Magnetic flux density ratio in the each section for the 3E10 T80 core.

For the 3F36 material, the operating frequency range for which the flux distribution within the core is constant, is extended up to 900 kHz for the T50 core, and up to 500 kHz for the T80 core. At higher frequencies and in relation to the three internal sections, the flux increases together with the frequency, while for the outer section there is a decrease in both of the tested cores.

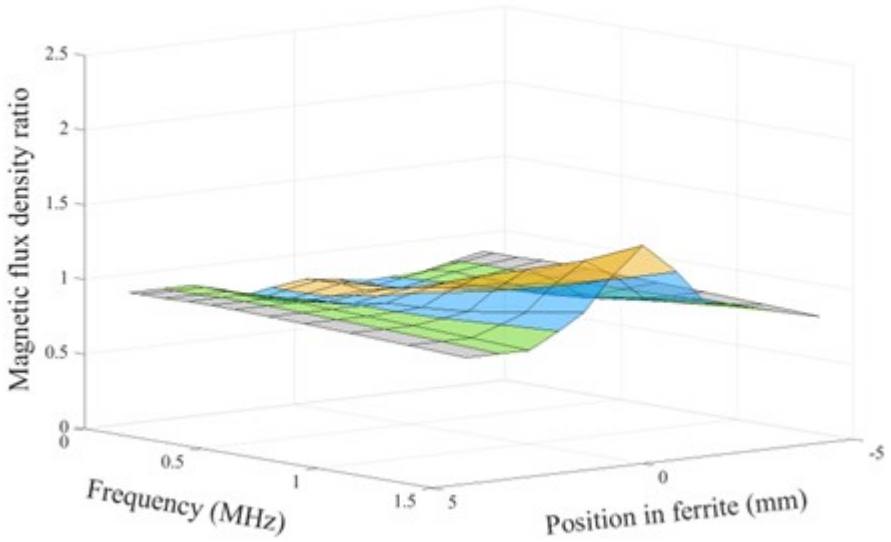


Figure 113. Magnetic flux density ratio in the each section for the 3F36 T50 core.

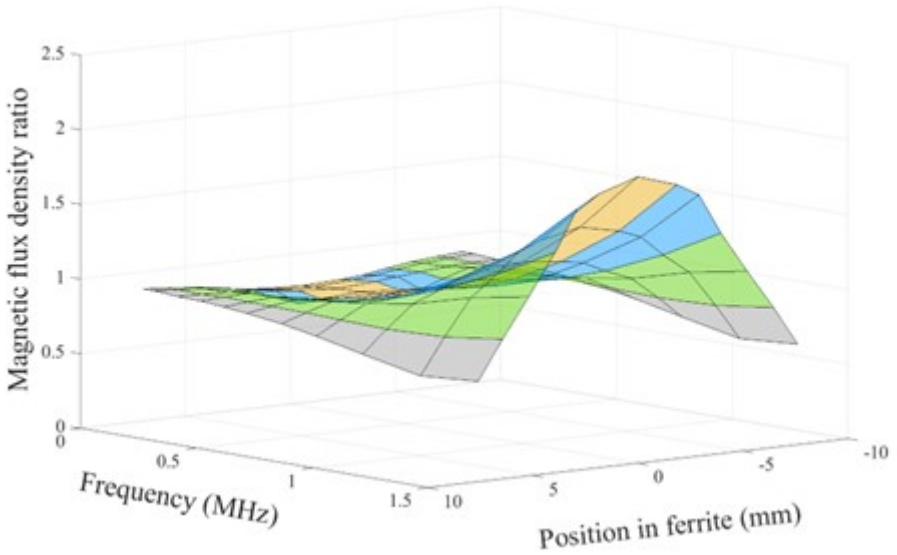


Figure 114. Magnetic flux density ratio in the each section for the 3F36 T80 core.

The mesh of the holes, applied in both methods, allows us to assess the flux distribution in the magnetic core. The results of the flux propagation, as discussed above, starting from the simple three-hole model up to the advanced four-section model confirms that magnetic flux distribution is affected by the frequency-dependent dynamic effects such as eddy currents and the wave propagation effect.

The three-hole model may be a subject for further discussion on the approach to the standardized test for magnetic material properties.

4.4 Conclusions

The non-uniform magnetic flux distribution has been experimentally validated for two Mn-Zn materials: 3F36 and 3E10. It is observed that in a high-permeability material, such as 3E10, the magnetic flux undergoes a skin effect that is analogous to that in ohmic conductors. At high frequency, the magnetic flux in the core's middle sections may flow in an opposite direction to the equivalent flux in the core. Lower permeability materials, such as 3F36, show a magnetic flux increase in the core's middle section caused by the wave propagation effects of a dimensional resonance.

5 A NOVEL LAMINATED FERRITE CORE

The objective of this section is to propose a core structure that can overcome the unequal flux distribution and the EMI filter degradation caused by the skin and dimensional resonance effects. A laminated Mn-Zn ferrite ring-core structure is proposed to improve the flux distribution as well as the core frequency characteristics. This chapter presents the results of a complex permeability characteristic comparison between laminated and solid ferrite cores. The lamination performance for various magnetic materials as well as for various core sizes is compared and contrasted. Finally, two single-phase common-mode chokes based on the solid and laminar ferrite cores are built and compared experimentally.

Section 5.1 presents the initial FEA investigation into the effects of laminations. Section 5.2 discusses the effect of lamination thickness on core performance. Section 5.3 investigates the performance effect of core stacking. Section 5.4 presents results for different material types. The impact of lamination on core size is investigated in Section 5.5. Section 5.6 presents the results from a two-stage EMI filter.

The results of this chapter have been published in the following papers and presentations:

- M. Kacki, M.S. Rylko, E. Herbert, J.G. Hayes, C.R. Sullivan, "A Study of Flux Distribution and Impedance in Solid and Laminar Ferrite Cores," *IEEE Applied Power Electronic Conference and Exposition (APEC)*, Anaheim, CA, 2019.
- M. Kacki, M.S. Rylko, E. Herbert, "PSMA-SMA Special Project – Phase II, Investigation on Magnetic Flux Propagation in Ferrite Cores," *The Power Source Manufacturers Association Technical Report*, 2020.
- M. Kacki, M.S. Rylko, "Core assembly having magnetic properties for an electrical device, and throttle comprising such a core assembly," patent application WO20200015962A1.

5.1 Finite-Element Analysis

Cores made of electrotechnical steel are often assembled to form a stack of insulated laminations, enabling the applied field to penetrate each lamination. The lamination thickness should be smaller than the skin depth for the required operating frequency. It has been known for decades that this method eliminates eddy-current losses in iron-based cores. Eddy-current losses in laminated cores are reduced by a factor $1/n^2$, where n is the number of laminations, as the path of the induced electric field is closed in each lamination [65]-[68]. Since traditional laminations are made of conducting material, the ferrite is perceived as a high-impedance bulk body. However, as is clear from earlier chapters, the ferrite bulk core also suffers from significant dimensional effects. Laminating the ferrite core can mitigate these effects and improve filter performance [19],[68]-[69].

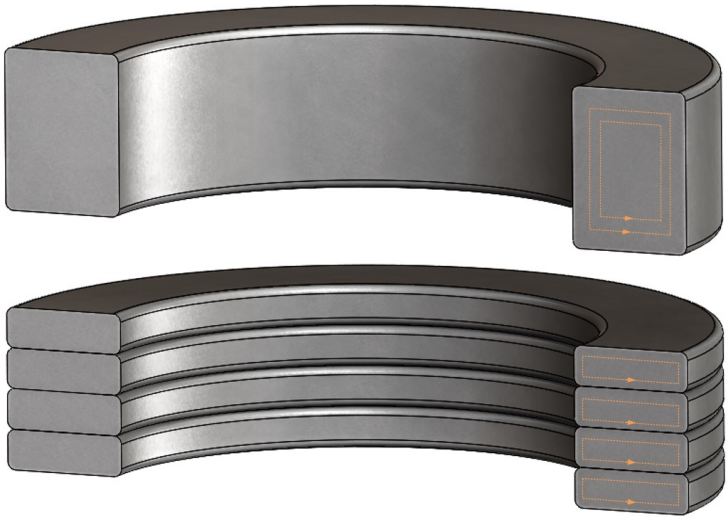


Figure 115. Ferrite eddy current reduction by lamination.

The FEA simulations are initially performed to quantify the effect of laminations on flux distribution in the ferrite ring core. The FEA calculation uses a 3-D eddy-current field solver. The analysis is performed at 500 kHz, while the simulation is based on the material characteristics developed in the second chapter of this thesis. The simulation results are shown in Figure 116. Intuitively, in the solid core, the magnetic flux is concentrated in the outer circumference while the core center exhibits flux density weakening due to the skin effect. The laminated core, on the other hand, merely shows a low magnetic field change. Since the core is a closed toroid in shape, it is also prone to reluctance effects along its radius.

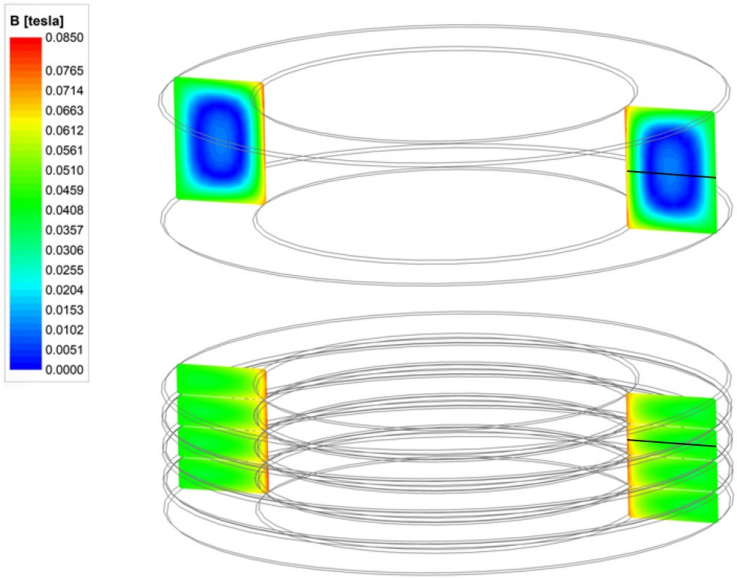


Figure 116. FEA results of the flux distribution in the solid and laminated ferrite ring core.

Detailed plots of the magnetic flux density amplitude along the core radius are presented in Figure 117.

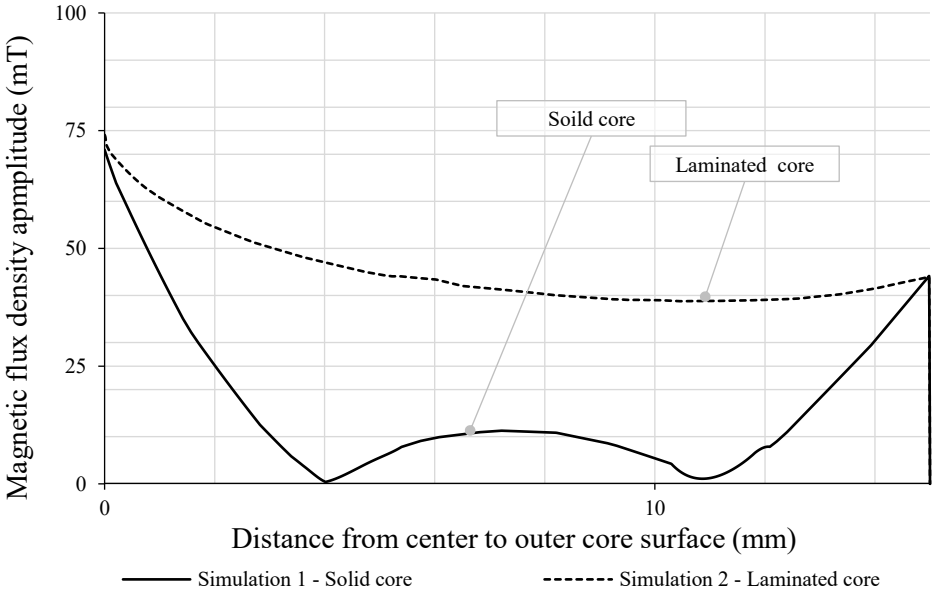


Figure 117. FEA modeling of the field distribution in solid and laminated ferrite ring cores.

At the considered frequency, high-frequency effects are developed in the solid core, while the laminated core flux distribution is simply dominated by the reluctance effect. At 500 kHz, the laminated core magnetic flux density gradually decreases along the cross section of the core, while the high-frequency effects are not visible.

5.2 New lamination thickness effect on core performance

The laminated core structure divides the conduction path into sub-regions that reduce the high-frequency effects. For such structures, the upper end of the frequency range is limited by the minimum lamination size. The lamination thickness impacts the core's complex characteristic at high frequencies. Thin laminations shift the skin and dimensional resonance effects to higher frequencies. The minimum lamination thickness is limited by the material grain size, shape and technology; the typical minimum core thickness is approximately 1.5 mm. The real permeability characteristic retains its stability at higher frequencies, while the eddy current losses are simultaneously reduced, which is visible in the reduced peak of the imaginary permeability characteristic. In order to investigate the impact of the lamination thickness on the performance of the core, the complex permeability for the T50/30/14 core, made of two materials, 3F36 and 3E10, is measured and contrasted with the core assemblies of two, four and six laminations stacked together to form a magnetic core with the same size and volume. Figure 118 shows the examined cores. Core lamination thickness varies from 2.3 mm up to 7 mm, while the overall core thickness remains intact. Ferrite laminations are not insulated from one another in contrast to the state of the art laminated electrotechnical steel which uses oxide film, or insulating varnish to insulate each lamination. The ferrite core surface layer tends to oxidize during sintering process and is considered as a nonmagnetic surface later. This oxidation layer is enough to insulate the ferrite laminations [70].



Figure 118. T50 cores to test lamination thickness impact on core performance.

The impact of the core lamination thickness on the 3F36 ferrite real and imaginary permeability components is shown in Figure 119 and Figure 120, respectively. As can be observed, the core with the smallest lamination shows the best performance. The real permeability characteristic is extended from 3 MHz to 15 MHz, while the loss peak of the imaginary permeability characteristic is reduced by half. Lamination thickness does not affect the magnetic performance of the core at low frequencies.

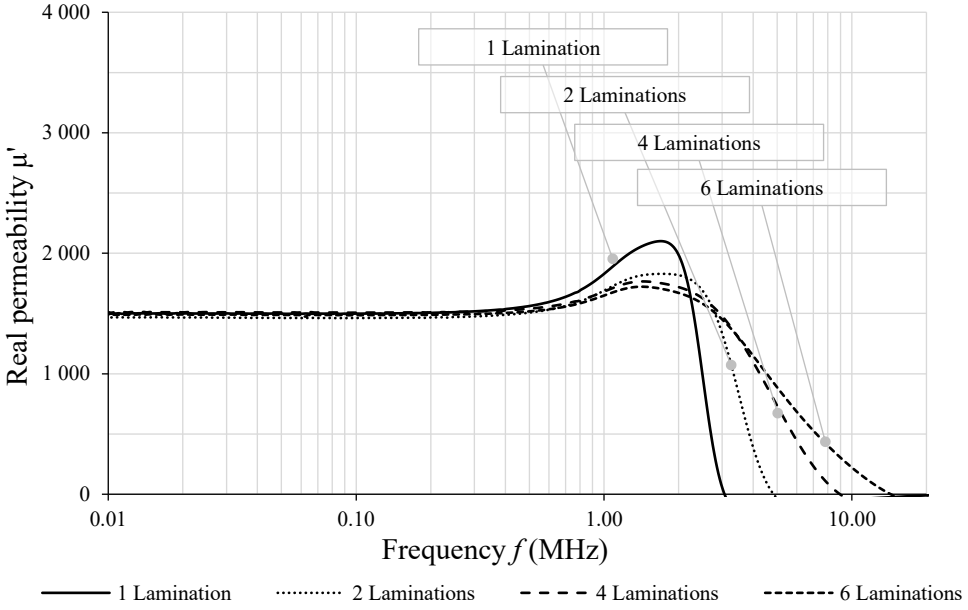


Figure 119. 3F36 ferrite real permeability vs. frequency for various lamination thicknesses.

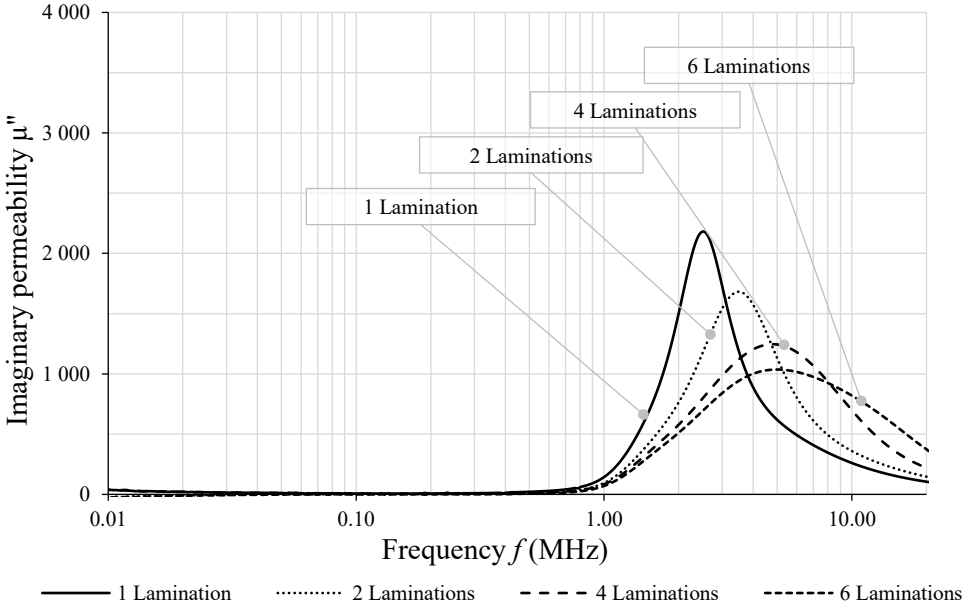


Figure 120. 3F36 ferrite imaginary permeability vs. frequency for various lamination thicknesses.

The effect of lamination thickness on the 3E10 ferrite real and imaginary permeability is shown in Figure 121 and Figure 122, respectively. Again, some improvement is visible in high permeability materials such as the 3E10. The real permeability characteristic is extended from 1 MHz to 2 MHz, while the loss peak of the imaginary permeability characteristic is reduced by 30%.

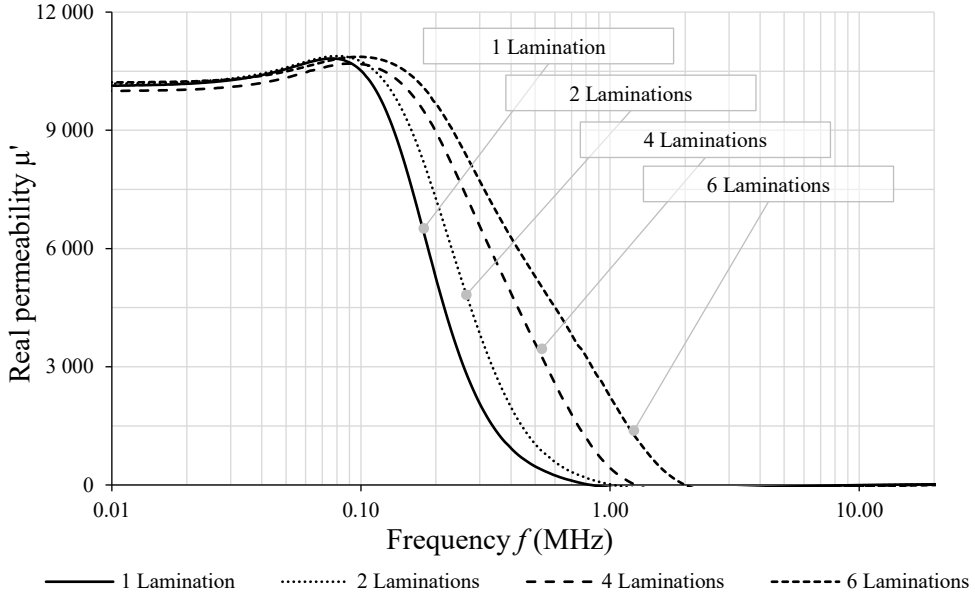


Figure 121. 3E10 ferrite real permeability vs. frequency for various lamination thicknesses.

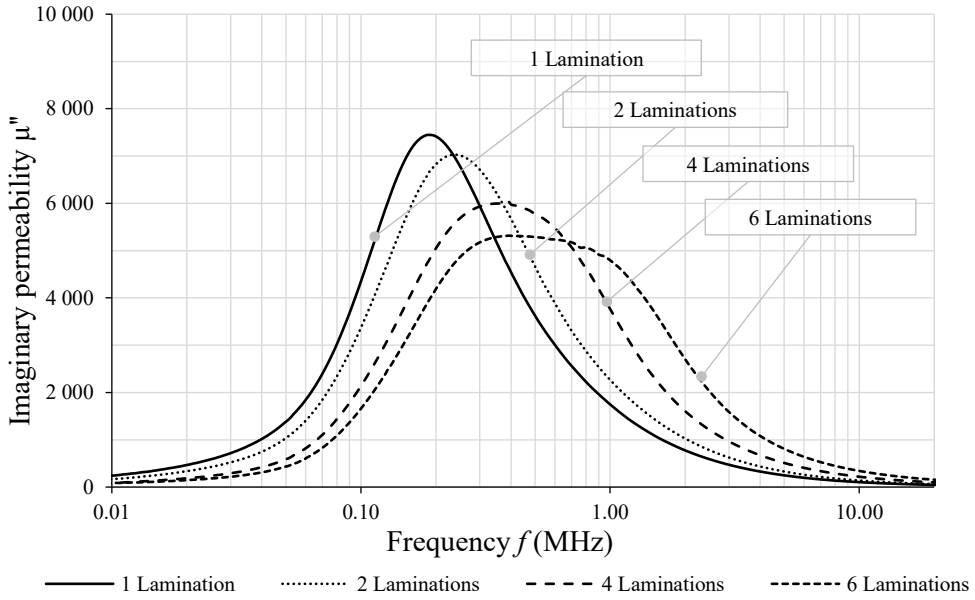


Figure 122. 3E10 ferrite imaginary permeability vs. frequency for various lamination thicknesses.

5.3 Modularity of laminated cores

Thin core laminations allow for an easy stacking up to the desired core height. In this section, the effect of lamination stacking, which increases the core cross-section, is examined. Reference inductance as well as impedance frequency characteristics are measured for a single lamination with the thickness of 2.3 mm. In the next step, the core cross section is doubled by an additional lamination, and in the final step, once again, the core cross section is doubled by adding extra laminations. Figure 123 shows cores used for this test



Figure 123. Cores used to test the effect of core modularity.

The outcome is presented in Figure 124 and Figure 125 for the 3F36 material, and in Figure 126 and Figure 127 for the 3E10 material. As the cross section of the core increases, both materials show proportional increases in inductance and impedance. Such a feature can significantly improve the magnetic component design process by the degree of design modularity. The CMC based on the laminated core can be easily scaled with frequency and power, as the dimensional resonance effect is mitigated within the considered frequency range.

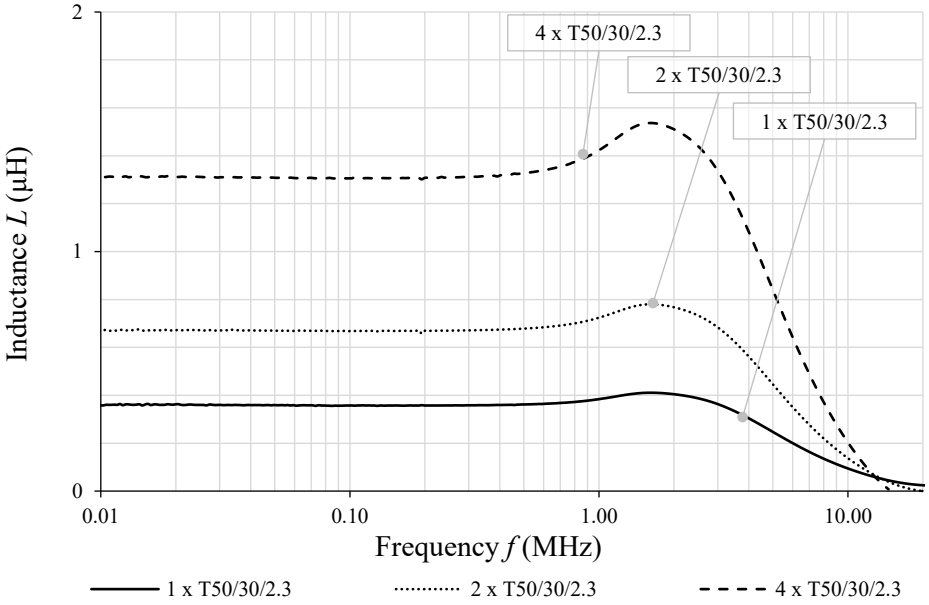


Figure 124. 3F36 ferrite inductance vs. frequency for various number of laminations.

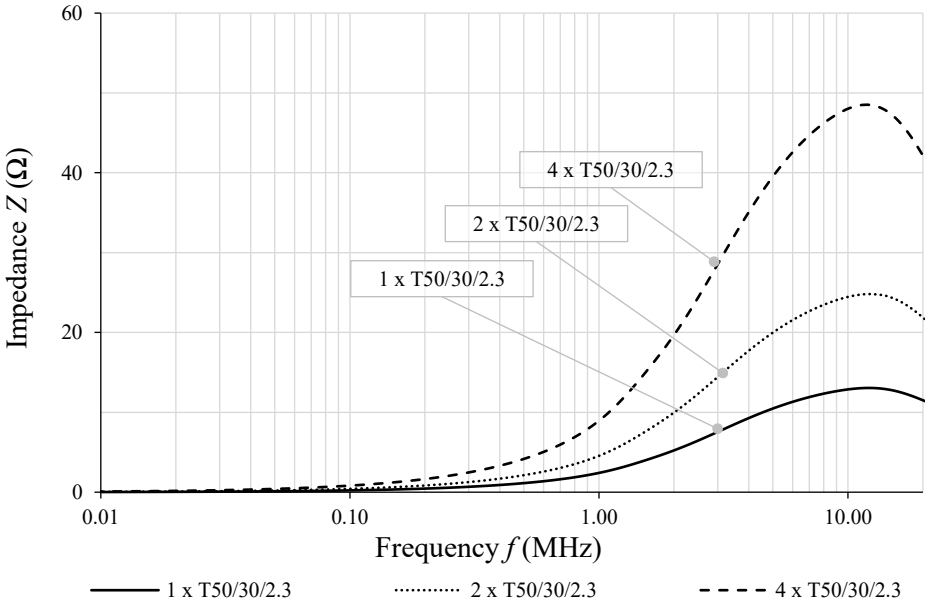


Figure 125. 3F36 ferrite impedance vs. frequency for various number of laminations.

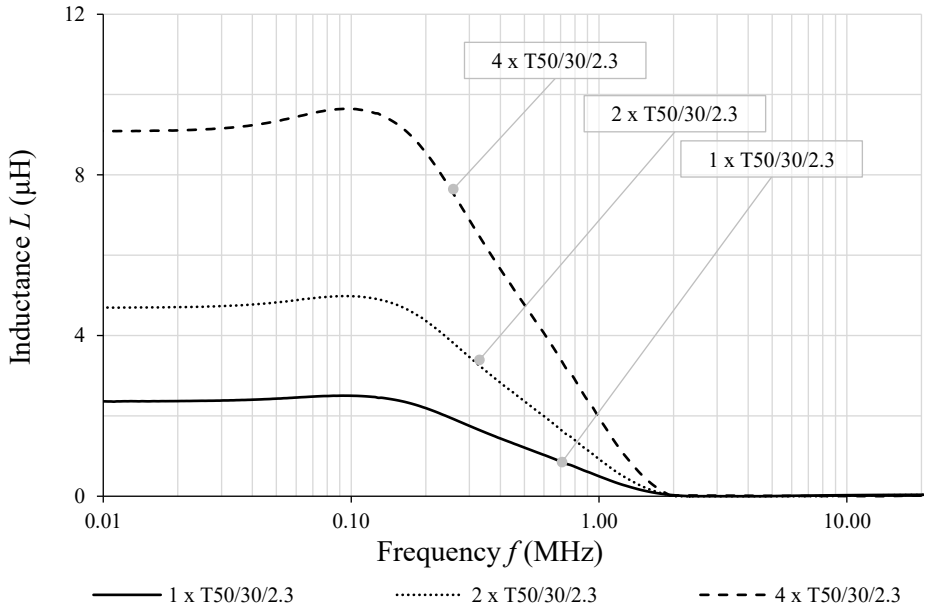


Figure 126. 3E10 ferrite inductance vs. frequency for various number of laminations.

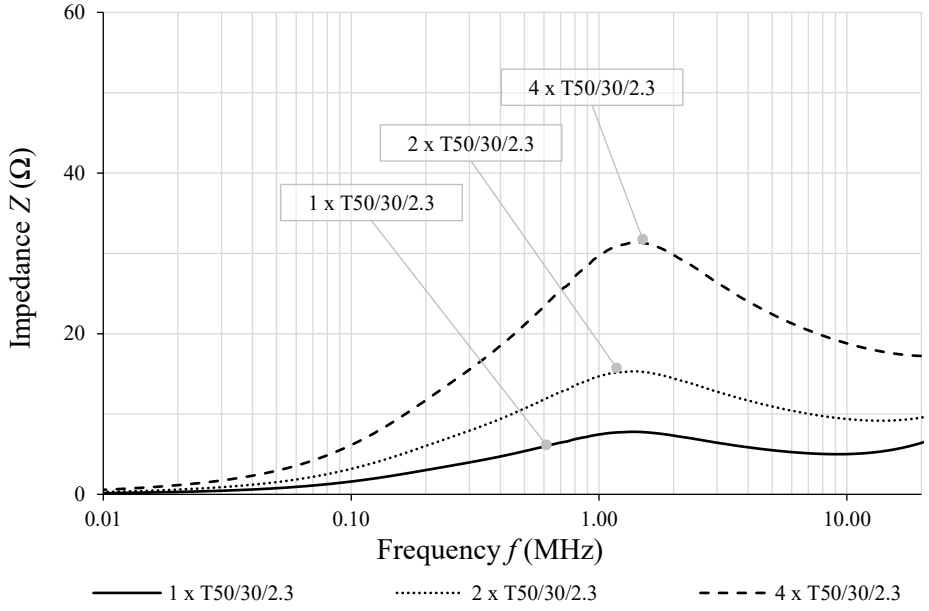


Figure 127. 3E10 ferrite impedance vs. frequency for various number of laminations.

5.4 The effect of magnetic material selection on the lamination

Ferrite properties such us permeability and permittivity have direct impacts on the frequency characteristics of the core, as both the skin effect and the dimensional resonance depend on these parameters. Therefore, laminating will also show the different impacts on the

core performance for different materials. A laminated core, made of several Mn-Zn ferrite materials, is tested in this section. The measured real and imaginary components of permeability are shown in Figure 128 and Figure 129, respectively.

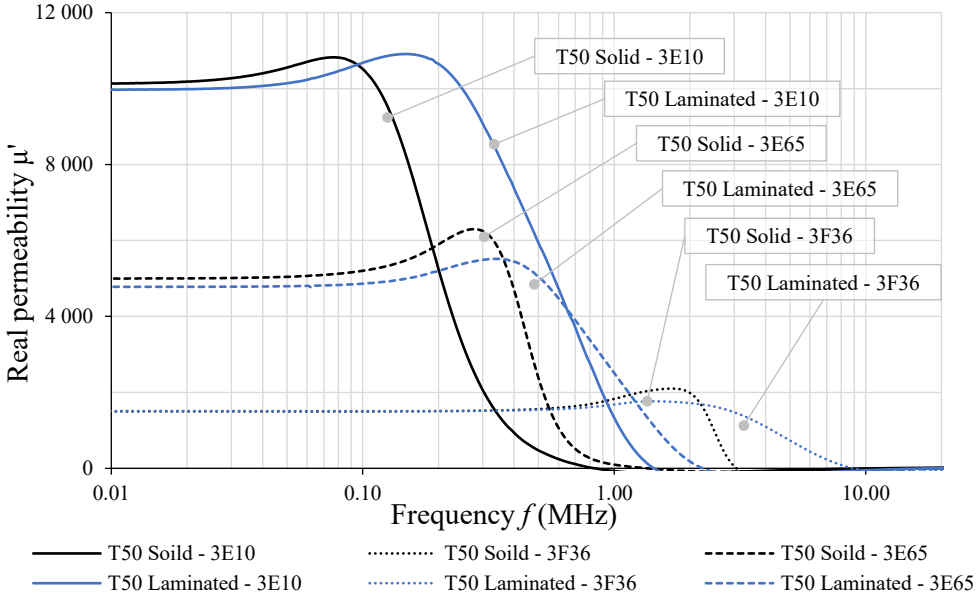


Figure 128. Real permeability vs. frequency for various Mn-Zn materials – comparison of laminated and solid cores

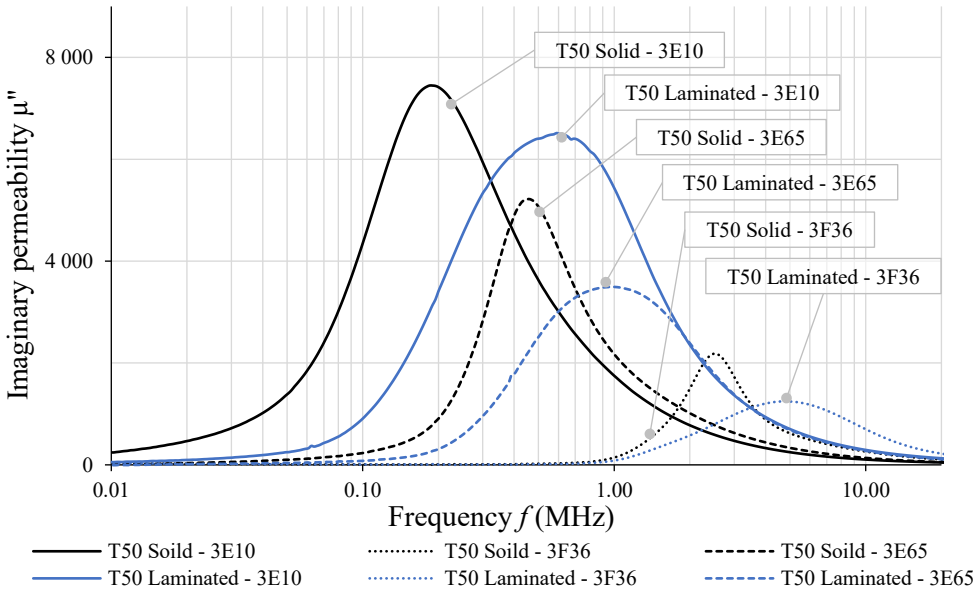


Figure 129. Imaginary permeability vs. frequency for various Mn-Zn materials – comparison of laminated and solid cores.

The complex permeability characteristic for each material is measured based on the T50/30/14 core, and its counterpart assembled with six laminations. Laminating significantly improves the frequency characteristic and reduces the power losses for all selected materials.

5.5 Core size effect on the lamination

The effect of core size on the lamination was identified as the last, but not the least point, to be validated. Previous chapters show that the core's size has a strong impact on the solid core's high-frequency performance. In order to investigate this effect, the complex permeability characteristic for three bulk core sizes: T29, T50, and T80, made of two materials, 3F36 and 3E10, are compared with their laminated counterparts. The laminated cores are stacked together from smaller cores with a thickness of 3.5 mm. The T29 laminated core is stacked out of 3 laminations, while the T50 uses 4, and the T80 uses 5 laminations. Figure 130 shows the cores used for this test.



Figure 130. Cores used to test the core size effect on lamination performance.

The complex frequency characteristics are presented in Figure 131 and Figure 132 for the 3F36 material, and in Figure 133 and Figure 134 for 3E10 material. As can be observed, the laminated cores, regardless of their size and material, show significant improvement in the frequency characteristic. The laminated T80 core maintains its performance up to 6 MHz for the 3F36 material, exactly the same as the T29 solid core. The measured real permeability characteristic for the T29 bulk core, made of the 3F36 material, drops to zero at 6 MHz, while the laminated core keeps its characteristic up to 11 MHz. The biggest improvement in the

imaginary permeability characteristic is visible in the T80 core. A significant loss increase, visible in the 3F36 material and caused by dimensional resonance, is reduced by half, and shifted to higher frequencies.

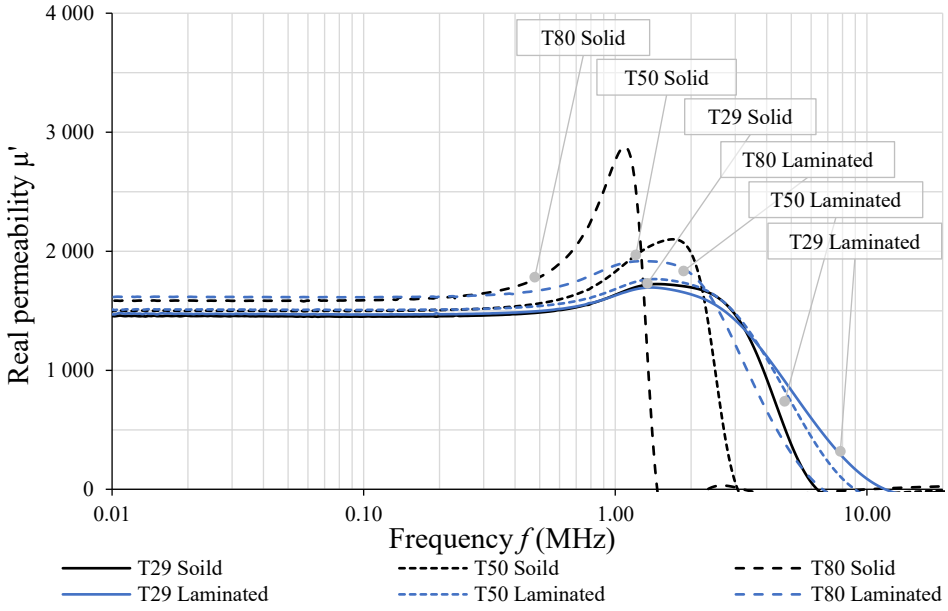


Figure 131. 3F36 ferrite real permeability vs. frequency for various core sizes.

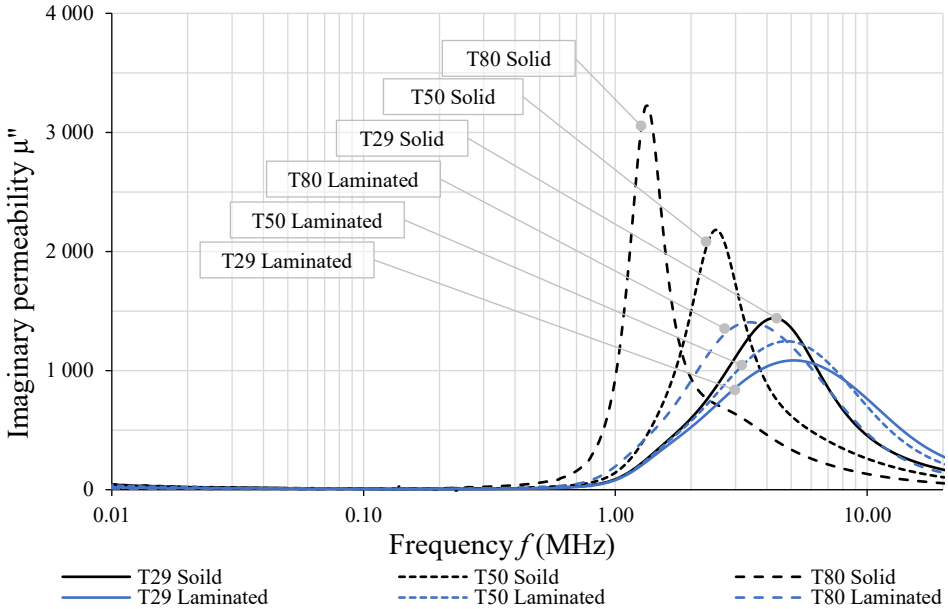


Figure 132. 3F36 ferrite imaginary permeability vs. frequency for various core sizes.

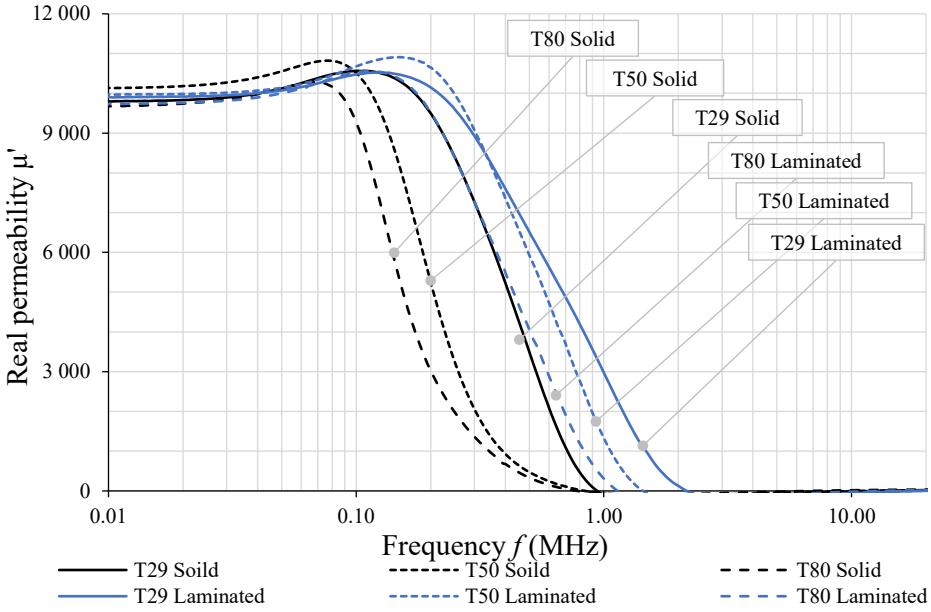


Figure 133. 3E10 ferrite real permeability vs. frequency for various core sizes.

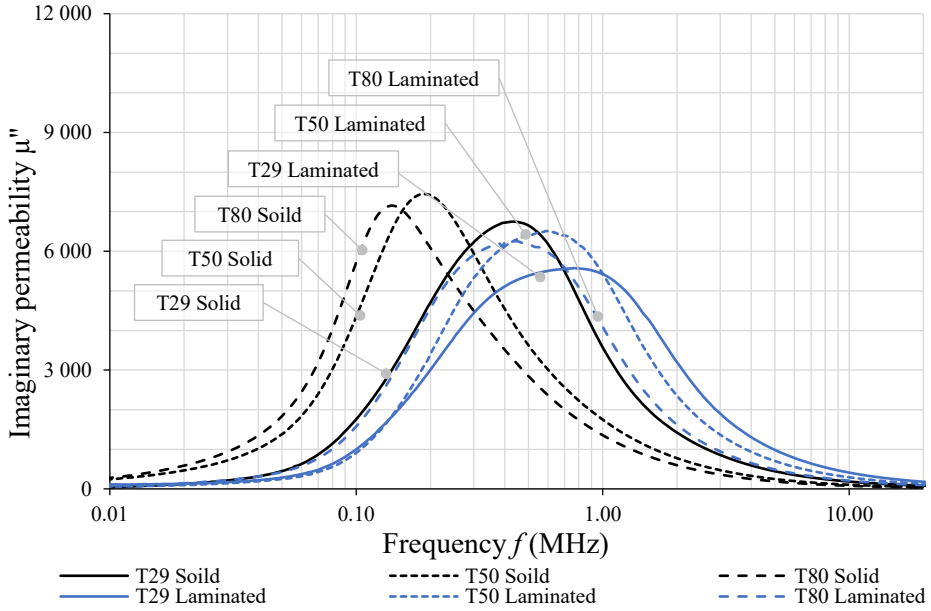


Figure 134. 3E10 ferrite imaginary permeability vs. frequency for various core sizes.

5.6 Verification of the flux distribution in laminated ferrite core

In order to investigate the flux distribution in the laminated ferrite cores, two bulk and two laminated T50 cores, made of two materials, 3F36 and 3E10, are selected to measure flux distribution. The laminated cores are stacked together from laminations of a thickness of

3.5 mm. Each tested core has three sets of bores. One set consists of two vertical, and one horizontal bore, each 0.65 mm at diameter. The four-shell core drilling scheme, and the procedure for calculation of the magnetic flux in the core is discussed in detail in Section 4.3. The results of the magnetic flux density for the 3E10 material is shown in Figure 135 and in Figure 136 for solid and laminated cores, respectively.

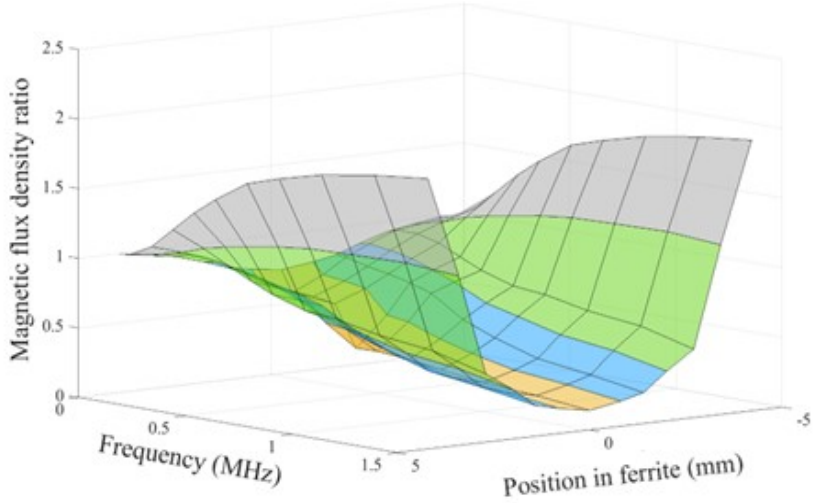


Figure 135. Magnetic flux density ratio in the each section for 3E10 T50 solid core.

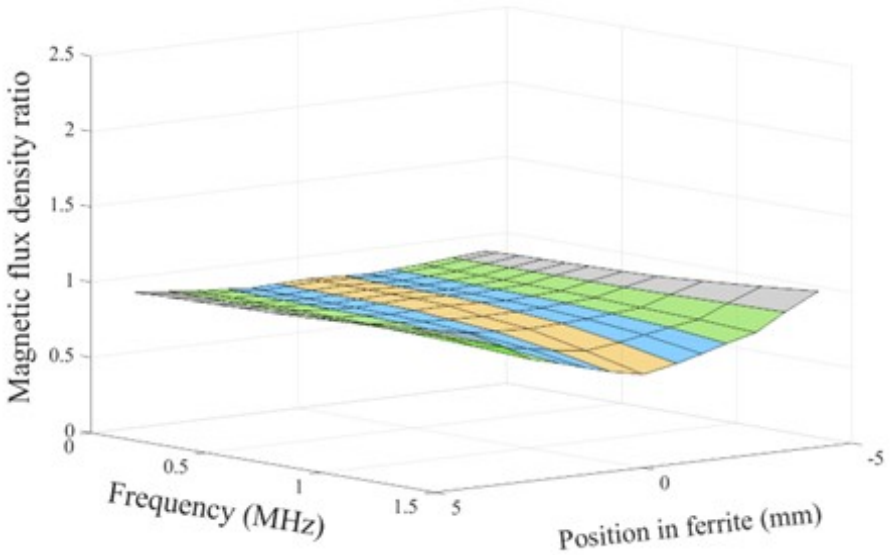


Figure 136. Magnetic flux density ratio in the each section for 3E10 T50 laminated core.

As can be seen, the solid T50 core mode of 3E10 material, shows frequency-dependent non-uniform flux distribution due to the skin effect. The flux strongly decreases together with the frequency in the three internal sections, while flux increase is visible in the outer core section. Magnetic flux in the laminated ferrite core is relatively stable up to 1.2 MHz in all

sections. For the outer section, the flux starts to slowly increase with frequency above 1.2 MHz, while for the three internal core sections minor flux weakening is visible. The frequency, in which the flux distribution within the core is constant, is extended from 200 kHz up to 1.2 MHz by core laminations. The validated magnetic flux distribution for 3F36 material is shown in Figure 137 and in Figure 138, for solid and laminated cores, respectively.

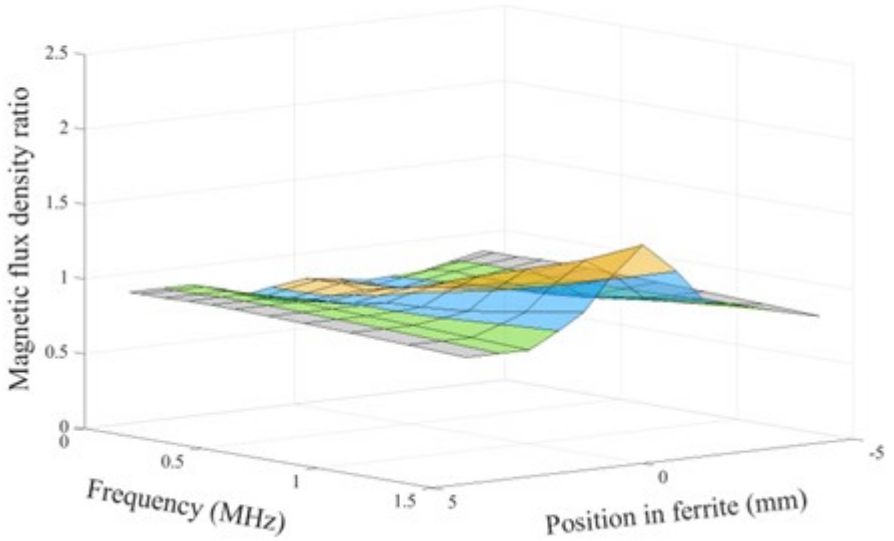


Figure 137. Magnetic flux density ratio in the each section for 3F36 T50 solid core.

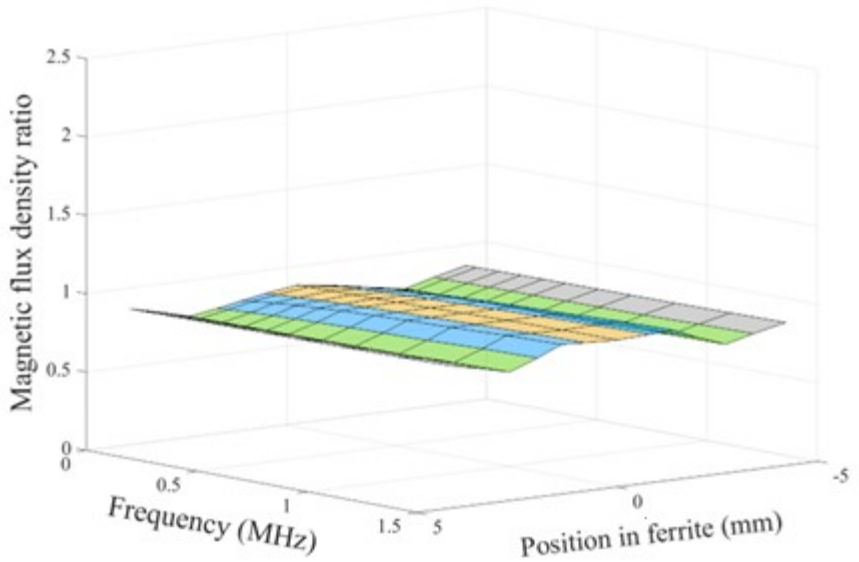


Figure 138. Magnetic flux density ratio in the each section for 3F36 T50 laminated core.

Substantial improvement is visible in the magnetic flux distribution for the laminated core. The ferrite laminations overcome the dimensional resonance effect visible in the solid core. Magnetic flux in the laminated core is stable up to 1.5 MHz. while in the solid core strong flux increase is visible in the inner core sections. In the solid core the magnetic flux is stable up to 0.4 MHz.

5.7 Single phase EMC filter based on the laminated ferrite core

In order to show the differences between the solid and laminated cores in a potential application, four single phase common-mode chokes are built. The designed choke is shown in Figure 139, while the basic construction parameters are presented in Table 11. The construction details are identical for all the chokes, except for the core. The turns are wound in single layers to reduce the winding effects on the impedance characteristic.

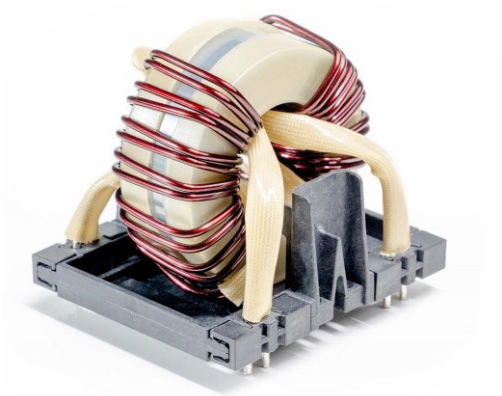


Figure 139. Common-mode choke built to test laminated ferrite cores.

TABLE 11. COMMON MODE CHOKE PARAMETERS.

Parameter	Unit	Design 1.1	Design 1.2	Design 1.3	Design 1.4
Core material	-	Mn-Zn ferrite 3E10	Mn-Zn ferrite 3E10	Mn-Zn ferrite 3E10	Mn-Zn ferrite 3E10
Core dimension OD x ID x H	mm	50 x 30 x 14	50 x 30 x 14	50 x 30 x 2.8 x 5 5 laminations	50 x 30 x 2.8 x 5 5 laminations
Material permeability	-	10 000	10 000	10 000	10 000
Core cross section	mm^2	140	140	140	140
Core volume	cm^3	17.6	17.6	17.6	17.6
Core mass	g	88	88	88	88
Number of turns	-	8/phase	8/phase	8/phase	8/phase
Wire type	-	1.8 mm Cu wire	1.8 mm Cu wire	1.8 mm Cu wire	1.8 mm Cu wire
Wire mass	g	60	60	60	60
CM Inductance	mH	1.19	1.15	1.05	1.11
DM Inductance	μH	4.1	4.2	4.1	4.3
Rated DM current	A	20	20	20	20
DC resistance	mΩ	2.12/phase	2.23/phase	2.14/phase	2.15/phase

The measured choke inductance and impedance frequency characteristics are shown in Figure 140 and Figure 141 , respectively. The laminated CM choke, in comparison to the solid core, has improved its performance in the frequency range between 200 kHz and 20 MHz. Compared to the CMC based on solid cores, the laminated choke impedance is doubled in the frequency range between 1 MHz and 20 MHz, while both chokes have the same size.

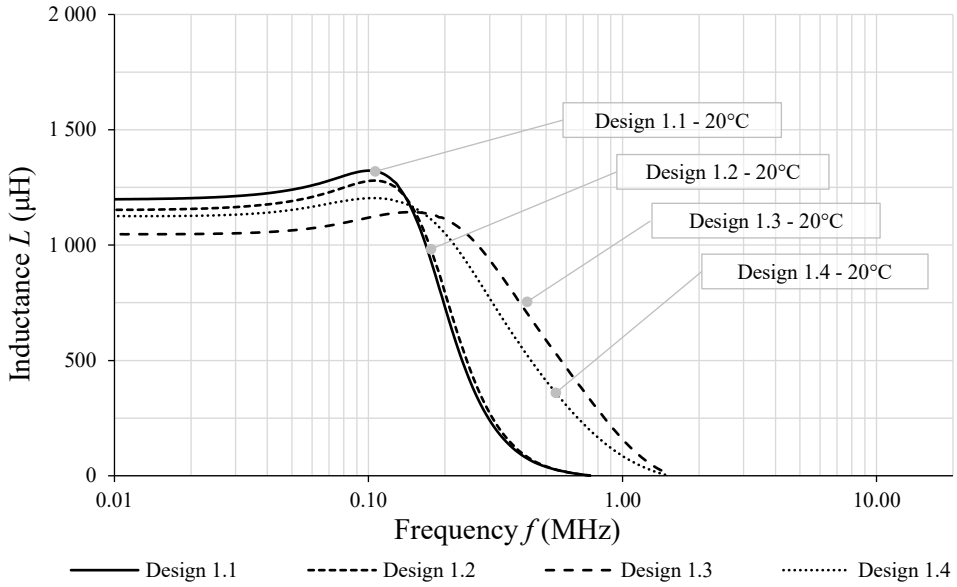


Figure 140. Tested common-mode chokes inductance vs. frequency.

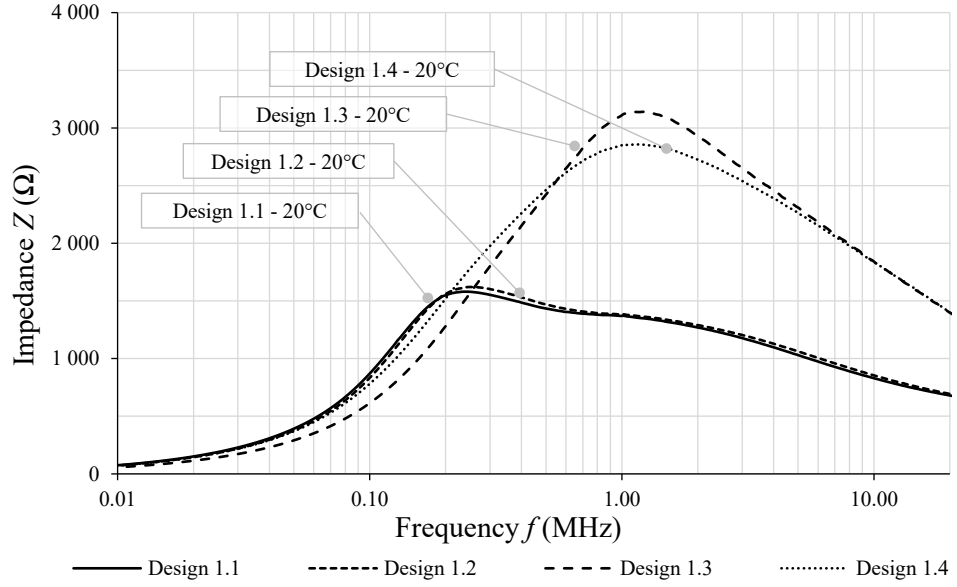


Figure 141. Tested common-mode chokes impedance vs. frequency.

As a final step, the designed common mode chokes are integrated into a two-stage EMI filter to demonstrate the laminated core advantages in the filter structure. The EMI filter schematic is shown in Figure 142, while the component specifications are presented in Table 12.

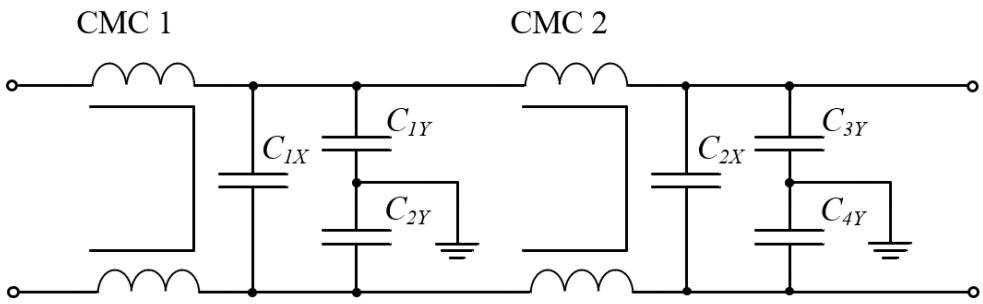


Figure 142. Schematic of the two stage EMI filter.

TABLE 12. EMI FILTER COMPONENT SPECIFICATION.

Component	Description
Common mode choke – solid core	Design 1.1 and Design 1.2
Common mode choke – laminated core	Design 1.3 and Design 1.4
Capacitor C_{1X}	4.7 µF - Kemet F863RL475M310ALW0L [71]
Capacitor C_{2X}	2.2 µF - Kemet F863FL225MK310ALW0L
Capacitor C_{1Y}, C_{2Y}, C_{3Y}, C_{4Y}	22 nF - Epcos B32022A3223M [72]

A photo of the EMI filters is shown in Figure 143. Both PCBs used for the comparison are identical. The detailed schematic diagram and PCB layout are shown in Appendix E.

The measured common-mode insertion loss characteristic for the two EMI filters is shown in Figure 144. The evaluation shows that the proposed laminated ferrite structure indicates significant attenuation improvement in the frequency range between 200 kHz and 20 MHz. Above 1 MHz, the difference is about 10 dB, while both filters maintain the same size.

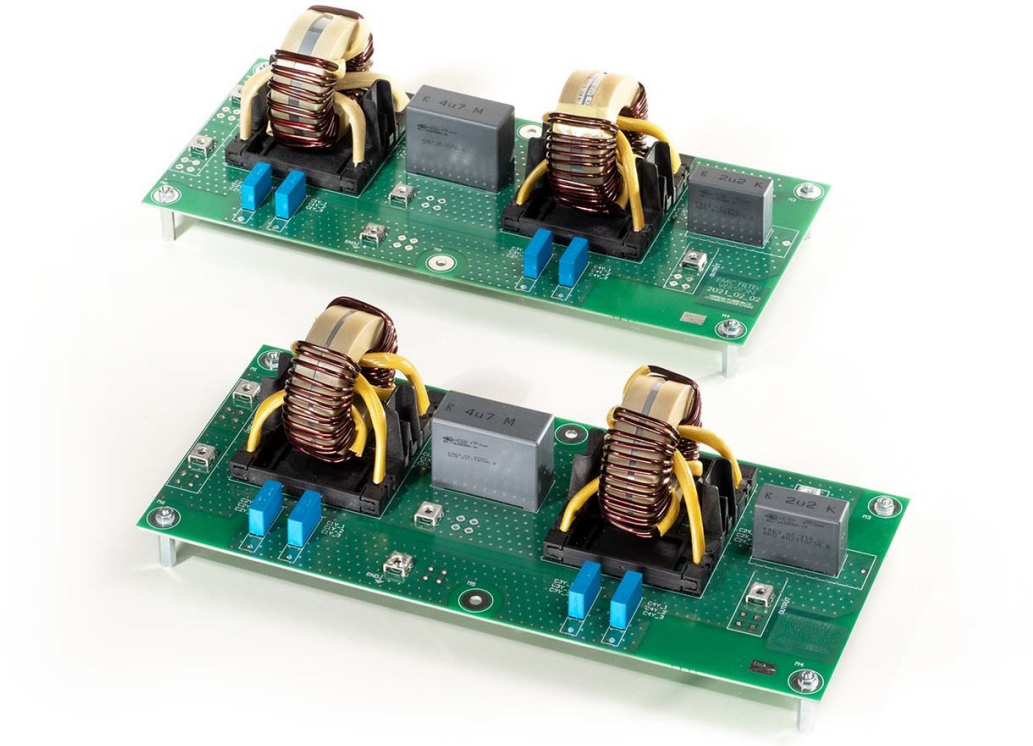


Figure 143. Complete EMI filters for common-mode choke test.

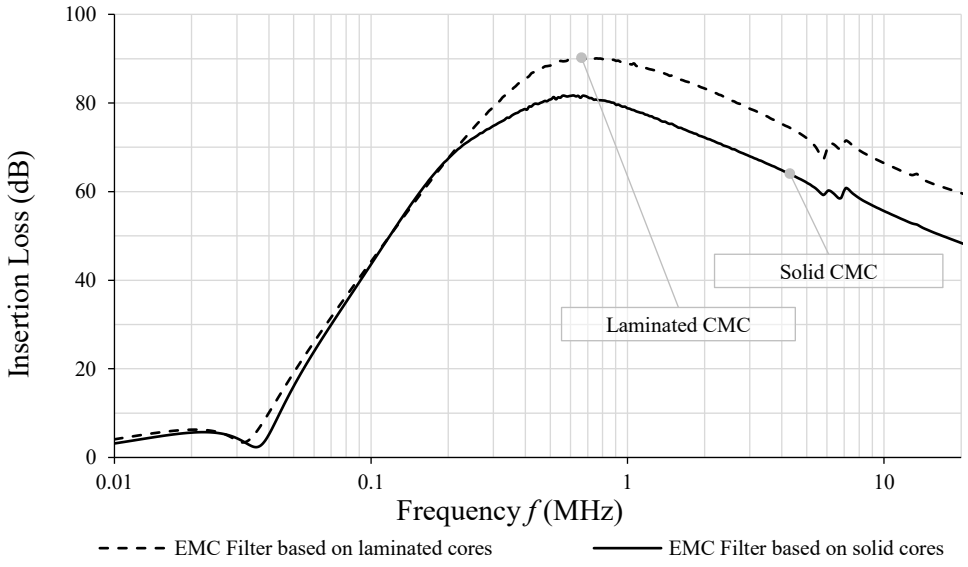


Figure 144. EMI filters common-mode insertion loss vs. frequency.

5.8 Conclusions

Laminated cores, made of selected Mn-Zn ferrite materials, were tested and compared with their solid counterparts. The effect of magnetic material and core size on laminations was investigated by comparison of complex permeability. In all cases, the laminated ferrite core improves the frequency characteristic and reduces power losses. The laminated Mn-Zn ferrite ring core shows a significant improvement in the flux distribution, as well as in the core frequency characteristics. The proposed core structure can overcome the unequal flux distribution caused by skin and dimensional resonance effects. The proposed laminated ferrite structure shows significant improvement of the impedance characteristic while maintaining the same core size, and so allows for a smaller component with the same properties as the bulk one. The availability of laminated cores opens up broad horizons for EMI filter design.

6 CONCLUSIONS AND FUTURE WORK

This chapter presents a summary of the findings of each chapter presented in this thesis. The work presented in this thesis is focused on the analysis, the identification, and the experimental verification of the high-frequency effects within the magnetic core used in high-frequency, high-power electromagnetic interference filters. A significant part of this work is devoted to defining the electrical properties of magnetic materials, magnetic flux modeling, and the experimental validation of the novel core structure that can overcome the unequal flux distribution observed in EMI filters.

6.1 Chapter Summaries

6.1.1 Chapter 1

Chapter 1 presents the motivation for the work described in this thesis. The continuous drive for energy conversion improvement focuses on the introduction of the new wide-bandgap semiconductors. The benefits of the new semiconductors include higher switching frequencies, higher rate of voltage (*dv/dt*) and current transients (*di/dt*), as well as higher power density. However, all the advantages arising from using the new semiconductors create a challenging for EMI filtering and the design of magnetic components. High frequency effects, such as the skin effect and dimensional resonance start to dominate the ferrite cores used in the EMI filters. The aforementioned high-frequency effects very often render the design processes inefficient, make the EMI filter oversized, and ultimately overpriced. As a result, this thesis focuses on the analysis, the identification, and the experimental verification of the high-frequency effects within the magnetic core. The identification of these effects is not possible without detailed magnetic material characteristics. Therefore, this dissertation also introduces methods to determine the Mn-Zn ferrite properties at high frequencies.

Four main objectives of this thesis were presented. They were (i) to propose a method to determine the high frequency properties of Mn-Zn ferrites, (ii) to present a comprehensive investigation of magnetic flux distributions in Mn-Zn ferrite cores based on the analytical 1-D and TLM models, as well as FEM simulations, (iii) to develop a method for experimental validation of the magnetic flux distribution in the ferrite cores, and (iv) to propose a core structure that can overcome unequal flux distribution and improve the overall EMI filter performance.

The advantages arising from the use of the WBG semiconductors are contrasted with associated challenges. These include high switching frequencies, and higher rates of voltage transients (*dv/dt*). An analysis concerning the impact of those challenges on the EMI harmonic spectrum was briefly described. The most important finding coming from this analysis is that the high-frequency content of the signals examined is significantly affected by the changing rise/fall times, as well as the switching frequency. The high-frequency signal spectra are significantly more determined by the rise/fall times than by the fundamental frequency of the waveforms. The WBG semiconductors cause a shift of the EMI envelope to higher frequencies and create a challenge for the magnetic component design.

The selection of the magnetic material is key for successful magnetic component design. Limitations of the magnetic material specifications, available in the datasheets provided by the manufacturers, were discussed in detail. Furthermore, it was shown how critical the magnetic material definition is for an efficient design process. It was shown that both the conductivity

and permittivity of magnetic material must be taken into account during the component design processes due to the direct impact of these parameters on the core's effective permeability, impedance and inductance. Only the identification of all magnetic material properties can allow for a precise estimation of the flux distribution in the ferrite core.

A brief discussion was presented on the fundamentals of skin depth and dimensional resonance in ferrite cores. It was shown that the dimensional resonance as well as the skin effect are dependent on the size and shape of the core and the wave frequency. Dimensional resonance and skin depth in magnetic materials are defined by the electromagnetic wave and the properties of the core. Electromagnetic wave parameters, the attenuation constant, and the wave number all define the high frequency effects within the core. In reality, ferrite skin depth and dimensional resonance occur together and interact to produce an effective resultant flux distribution in the magnetic core.

6.1.2 Chapter 2

Chapter 2 discusses new methods for determining the high-frequency properties of Mn-Zn ferrites, as the ferrite manufacturer's specifications provide average material characteristics and are of limited use as far as detailed analyses are concerned. The magnetic materials are characterized by their complex permeability, permittivity, and power losses. The dimensions of the tested Mn-Zn ferrites affect the measured core characteristics; therefore, special attention must be paid during the selection of the core size for measuring the properties of Mn-Zn ferrites at high frequencies.

The complex permeability characteristic was examined for various core sizes and materials. A significant outcome of the testing is that the complex permeability characteristics vary with physical size, temperature, and compression force. The toroidal core T6/4/2.8 was selected as the core which provides the complex permeability characteristic with the highest possible accuracy as it stems from a natural manufacturing process, followed by a press and sintering process without any additional machining that might affect material performance. A dedicated test fixture was developed to measure the complex permeability of the T6 core. The test fixture provides one turn, equally distributed around the tested core, without any mechanical stress, and a reliable connection to the measurement device via a concentric cable. The test fixture may be easily duplicated as it has been built with off-the-shelf parts. The impact of temperature and mechanical stress on the complex permeability characteristics has been experimentally validated for selected Mn-Zn materials. In general, the performance deteriorates as temperature and mechanical stress increase; therefore, both effects must be included in the magnetic component design process because such highly adverse conditions are common in applications.

Ferrite complex permittivity measurements were taken up to 20 MHz. It was shown that these measurements may be dominated by the dimensional resonance developed as a result of the sample size. In order to define ferrite electrical characteristics, the available methods were compared and contrasted. The parallel-plate method was selected for the ferrite permittivity validation, and a dedicated test fixture was developed. The test fixture has exchangeable, shielded electrodes and strain gauges to control the ferrite stress during measurements, and reliable connections to the measurement device via a concentric cable. It has been experimentally proven that the sample with the smallest available cross-sectional dimensions should be selected to accurately measure the ferrite complex permittivity. However, there are technical limitations to producing core samples of extreme small dimensions. For this reason, a measurement extrapolation, based on Constant Phase Elements, was introduced to enable accurate modelling of the core permittivity vs. frequency. Complex permittivity is somewhat complementary to permeability; therefore, the influence of temperature and mechanical stress was also verified. A permittivity increase was observed as the temperature and mechanical stress increased.

Accurate core loss prediction, besides the complex permeability and permittivity, is also an essential part of the process of magnetic component design. State of the art methods are based on sinusoidal-excitation loss-measurement for small cores; therefore, neither the core shape nor size effects are included. As a consequence, the core size effect on power losses at high field amplitude and rectangular wave excitations was validated. In order to measure the core losses, a dedicated test setup was designed and built. The developed test setup is capable of operating with a maximum input voltage of 60 V, an output current of 10 A, and a switching frequency of up to 500 kHz. It also allows for operation with rectangular voltage waves with a variable duty cycle, as well as an asymmetric rectangular wave with constant volt-seconds in each half of the waveform. Core losses under rectangular excitation were investigated for three core samples, of size T29, T50, and T87, made of 3C95 ferrite material up to 250 kHz. It was shown that as the switching frequency increases the power losses in the larger cores much faster compared to small cores. Therefore, the magnetic losses in the ferrite core cannot be accurately calculated from the widely available power loss curves, as they not account for performance deterioration with size.

Appendix A and B present the experimental complex permeability and permittivity characteristics for the various materials.

6.1.3 Chapter 3

Three calculation methods for a detailed analysis of the magnetic flux distribution were introduced and compared in this chapter. The three methods were; the 1-D analytical model

based on Maxwell`s equations, the novel shell-based transmission-line model, and the model based on the FEM and Maxwell 3D eddy-current field solver.

The 1-D analytical model, based on Maxwell`s equations, enables the modeling of the electromagnetic wave propagation in lossy materials, such as ferrites. The 1-D model was used for the modeling of the magnetic field within an infinite ferrite plate, wherein the plate thickness corresponds to the lowest cross-sectional dimension of the tested cores. The 1-D model was used to calculate the complex permeability characteristics for various core sizes made of two materials: 3E10 and 3F36. Calculated characteristics were compared with experimentally-measured core characteristics. The 1-D analytical equation correlate well to the experimental results for the samples with the core cross sectional area shape ratio of 1:1. As the core shape ratio changes, the model shows lower accuracy. Therefore, the core shape ratio constrains the 1-D model to limited core shapes.

The shell-based transmission-line model is based on a sectioned magnetic core. It was shown that concentric shells, adequately small in size, can precisely reproduce unequal magnetic flux distributions. The model is very intuitive and may be applied in any circuit simulator. What is more, it can also be easily incorporated into a simulation of a higher-order system. The core is modeled by a network of series inductances and resistances per shell with shunt capacitances and resistances. The novel transmission-line model was used to calculate the frequency-dependent permeability characteristics for the various core sizes made of two materials: 3E10 and 3F36. Calculated characteristics were compared with experimentally measured core characteristics. The model shows a very good correlation with measurements. The peak of the real and imaginary permeability characteristics is also well represented. The shape of the cross-sectional area of the cores does not have a negative impact on the core's transmission line model accuracy, unlike the 1-D model.

The FEM model was used to visualize the flux distribution in the T50 magnetic core. The core made of 3F36 material shows a large amplitude flux concentrated in the inner part of the core's cross section, which is as a result of the dimensional resonance. In the core made of 3E10 material, the flux is concentrated along the outer circumference while the core center exhibits flux density weakening. The flux distribution is dominated by the skin effect. The Maxwell 3D simulation was used to calculate the frequency dependent permeability characteristics for the various core sizes made of two materials, 3E10 and 3F36. The calculated characteristics were compared with experimentally measured core characteristics. An exact match was achieved at low frequencies for all the simulated cores and materials. Discrepancies in the characteristics emerge at high frequencies. Improvement may be achieved if the software is changed from Maxwell 3D to HFSS [58], as it is the frequency range where the wave effect may dominate the flux distribution.

High-frequency effects, such as the dimensional resonance and the skin effect within the core can be modelled and predicted based on the aforementioned models. These models were used to investigate skin depth and dimensional resonance. In addition, the clear impact of these phenomena was shown in various materials and core sizes. Each method has its strengths and weaknesses. However, taking into account the calculation time, the TLM method should be further developed in order to reduce the calculation error, and raise the possibilities of visualizing the flux distribution in the core

6.1.4 Chapter 4

Chapter 4 introduced two verification methods for a detailed analysis of the magnetic flux distribution: two shell, and one based on the four shells. The experimental validation of the flux distribution was an experimental validation of the high frequency core effects, such as the dimensional resonance and the skin effect.

The simplified approach shows the magnetic flux distribution in two sections. Three bores were made in each tested core: two vertical, and one horizontal, each 0.65 mm in diameter. During the experiment, sense windings were inserted into the bored holes to determine the flux and the phase shift of each of the core segments. The core flux pattern for the T50 core, made of 3E10 material, shows that the flux is concentrated in the outer circumference while the core center exhibits flux density weakening. However, for the T50 core, made of 3F36 material, the magnetic flux is stronger and concentrated in the inner part of the core cross section.

The second method represents the magnetic flux distribution in four sections. The number of drilled holes was tripled and bores sets were distributed around the core in order to minimize reduction of the core cross section. The four-section core drilling scheme increases the measurement accuracy and allows for a 3D representation of the magnetic flux. Simultaneously, besides the T50 cores, the flux distribution was measured in T80 cores, in which skin and dimensional resonance effects develop at lower frequencies. The results of the magnetic flux show a non-uniform flux distribution that accounted for skin effect for 3E10 material and dimensional resonance for 3F36 material.

The mesh of the holes, applied in both methods, allows us to assess the flux distribution in the magnetic core. The results of the flux propagation, starting from the simple three-hole model up to the advanced four-section model, confirms that the magnetic flux distribution is affected by the frequency-dependent dynamic effects. Discussed results are shown to be consistent with the analytical calculations and the FEA simulations.

6.1.5 Chapter 5

Chapter 5 introduces a novel, laminated core structure to mitigate unequal flux distribution and improve the overall EMI filter performance. Traditional electrotechnical steel laminations are made of conducting material and the ferrite is traditionally perceived as a high-impedance bulk body. However, the ferrite structure also contains conductive paths that may develop adverse effects in certain conditions. Ferrite laminations, similarly to electrotechnical steel, reduce eddy-current losses and shift the dimensional resonance to higher frequencies.

The performance of ferrite lamination thickness was analysed by comparison of complex permeability for the T50/30/14 core, made of two materials; 3F36 and 3E10. The cores are assemblies of two, four and six laminations stacked together to form a magnetic core that retains the same size and volume of the T50/30/14 core. It was shown that the core with the smallest laminations shows the best performance. The real permeability characteristic was extended from 3 MHz to 15 MHz, while the loss peak of the imaginary permeability characteristic was reduced by half. The laminations did not affect the magnetic performance of the core at low frequencies.

In the next step, the effects of magnetic material and core size on laminations was investigated. Laminated cores, made of several Mn-Zn ferrite materials, were tested. In all cases, the laminated ferrite core improves the frequency characteristic and reduces the power losses. In order to investigate this effect, the complex permeability characteristic for three bulk core sizes, T29, T50, and T80, made of two materials, 3F36 and 3E10, were compared with their laminated counterparts. The laminated cores, regardless of their size and material, show significant improvement over the frequency range.

Finally, the differences between the solid and laminated cores were tested in a potential application of an EMI filter. The laminated CM choke, in comparison to the solid core, has improved performance over the frequency range between 200 kHz and 20 MHz. Compared to the CMC based on solid cores, the laminated choke impedance was doubled in the frequency range between 1 MHz and 20 MHz, with both chokes having the same size. The measured common-mode insertion loss characteristic for the two EMI filters shows that the laminated ferrite structure gives a significant attenuation improvement in the frequency range between 200 kHz and 20 MHz. Above 1 MHz, the observed difference is about 10 dB.

Laminated cores enables a new area for EMI filter design. The proposed core structure can mitigate the unequal flux distribution caused by skin and dimensional resonance effects.

6.2 Future work

Possible future work on this project may be divided into the following areas.

6.2.1 Complex permeability and permittivity modelling

The developed models and magnetic material characteristics allows the modelling of the core size effect on complex permeability. Is was also experimentally confirmed that the core performance deteriorates as temperature and mechanical stress increases. Therefore, both effects must be included in the magnetic component design process as such highly adverse conditions are common in applications. The model must provide a superior prediction for these effects of temperature and mechanical stresses.

6.2.2 Magnetic core power loss analysis

Magnetic loss tangent frequency characteristics show a constant core loss increase up to the frequency where dimensional resonance becomes apparent. Measurement with a higher field amplitude shows a local loss minimum at low frequency which is not apparent in the low field amplitude characteristic. Therefore, further in-depth analysis is required to quantify this effect, as the increase in eddy current losses could dominate the measurements at a high field amplitude and suppress the dimensional resonance. It may lead to the conclusion that dimensional resonance has a significant effect on EMI filters that by nature operate at much lower signal power levels.

6.2.3 TLM model validation and improvement

The TLM model shows good accuracy for modelling of the high-frequency effects of dimensional resonance and skin effect within the core which can be predicted with a good accuracy. In addition, the clear impact of these phenomena can be observed in various materials and core sizes. The calculation time is the lowest for the TLM method. The TLM method should be further developed in order to reduce the calculation error, and raise the possibilities of visualising the flux distribution in the core. Nonlinear elements, such as CPE, may help with more accurate core modelling. The magnetic core could also be bored in such a way that TLM shells will match the bored sections. The flux distribution can then be precisely assessed and compared between the TLM and the experiments.

6.2.4 Study on flux propagation under rectangular waveform

The developed core loss tester could be used for flux propagation investigation for rectangular excitations. Higher rates of voltage transients (*dv/dt*), in combination with high core permittivity, may lead to different flux pattern than those observed with sinusoidal excitation.

REFERENCES

[1] https://www.iea.org/reports/key-world-energy-statistics-2020/final-consumption. Accessed on 10.12.2021.

[2] B. Singh Pali, S. Vadhera, "Renewable energy systems for generating electric power: A review," *IEEE International Conference on Power Electronics, Intelligent Control and Energy Systems (ICPEICES)*, July 2016.

[3] E. Hoene, G. Deboy, C.R. Sullivan, G. Hurley, "Outlook on developments in power devices and integration: recent investigations and future requirements," *IEEE Power Electronics Magazine,* vol. 5, issue 1, pp. 28-36, March 2018.

[4] J. Millan, P. Godignon, X. Perpina, A. Perez-Tomas, J. Rebollo, "A survey of wide bandgap power semiconductors devices," *IEEE Trans. Power Electron.,* vol. 29, pp. 2155-2163, 2014.

[5] J. Biela, M. Schweizer, S. Waffler, B. Wrzecionko, J.W. Kolar, "SiC vs. Si evaluation of potentials for performance improvement of power electronics converter system by SiC power semiconductors," *Industrial Electronics, IEEE Transactions,* vol. 58, issue 7, pp. 2872–2882, July 2011.

[6] Di Han, J. Noppakunkajorn, B. Sarlioglu, "Comprehensive Efficiency, Weight, and Volume Comparison of SiC- and Si-Based Bidirectional DC–DC Converters for Hybrid Electric Vehicles," *IEEE Transactions on Vehicular Technology*, vol. 63, issue: 7, pp. 3001-3010, September 2014.

[7] J.W. Kolar, J.E. Huber, "Future Power Electronics 4.0 3-Phase SiC/GaN Converter Systems," *Tutorial at the 36th Applied Power Electronics Conference and Exposition (APEC2021),* June 2021

[8] H. Chung, S. Hui, K. Tse, "Reduction of power converter EMI emission using soft-switching technique," *IEEE Trans. Electromagn. Compat.,* vol. 40, pp. 282–287, August 1998.

[9] X. Wu, J. Yang, H. Chen, Z. Qian, "Analysis and design considerations for EMI and losses of RCD snubber in flyback converter," in Proceeding of *Twenty-Fifth Annual IEEE Applied Power Electronics Conference and Exposition*, Palm Springs, CA, Murch 2010.

[10] A. Bhargava, D. Pommerenke, K.W. Kam, "DC-DC buck converter EMI reduction using PCB layout modification" *IEEE Trans. Electromagn. Compat.,* vol. 53, pp. 806–813, August 2011.

[11] H.W. Ott, *Noise Reduction Techniques in Electronic Systems,* John Wiley and Sons, 1988.

[12] H.W. Ott, *Electromagnetic Compatibility Engineering, John* Wiley and Sons, 2009.

[13] P. Bardos, "Predicting the EMC performance of high-frequency inverters," *IEEE Applied Power Electronics Conference*, pp. 213-219, May 2001.

[14] https://www.sma.de/en/products/solarinverters/sunny-tripower-core1.html. Accessed on 10.12.2021.

[15] C. Deng et al., "Integration of both EMI filter and Boost inductor for 1 kW PFC converter," *IEEE Transactions on Power Electronics* , vol. 29, no. 11, pp. 5823–5834, November 2014.

[16] G.R. Skutt, *High-frequency dimensional effects in ferrite-core magnetic devices*, Ph.D. dissertation, Virginia Polytechnic Institute, Blacksburg, Virginia, 1996.

[17] G.R. Skutt, F.C. Lee, "Characterization of dimensional effects in ferrite-core magnetic devices," *IEEE Power Electronics Specialist Conference,* June 1996.

[18] M. Kącki, M.S. Ryłko, J.G Hayes, C.R. Sullivan, "Magnetic material selection for EMI filter," *IEEE Energy Conversion Congress and Exposition (ECCE)*, October 2017.

[19] M. Kącki, M.S. Ryłko, J.G Hayes, C.R. Sullivan, "A study of flux distribution and impedance in solid and laminar ferrite cores*," IEEE Applied Power Electronics Conference and Exposition (APEC)*, March 2019.

[20] https://www.ferroxcube.com/en-global. Accessed on 18.02.2022.

[21] https://product.tdk.com/en/search/ferrite/ferrite/ferrite-core/catalog. Accessed on 18.02.2022.

[22] http://www.chinadmegc.com/en/products_list.php?2. Accessed on 18.02.2022.

[23] N. Oswald, B.H. Stark, D. Holliday, C. Hargis, "Analysis of shaped pulse transitions in power electronics switching waveforms for reduced EMI*," IEEE Transactions on Industry Application,* vol. 47, issue: 5, pp. 2154-2165, October 2011.

[24] Alex van den Bossche, Vencislav Cekov Valchev, "*Inductors and Transformers for Power Electronics,*" CRC Press, 2005.

[25] M. K. Kazimierczuk, "*High-Frequency Magnetic Components,*" John Wiley and Sons, 2009.

[26] H. Schwenk, J. Beichler, W. Loges, Ch. Scharwitz, "Actual and future Developments of Nanocrystalline magnetic materials for Common Mode Chokes and Transformers," *Proceedings of PCIM Europe 2015; International Exhibition*

and Conference for Power Electronics, Intelligent Motion, Renewable Energy and Energy Management, May *2015.*

[27] Georgi T. Nikolov, Vencislav C. Valchev, "Nanocrystalline magnetic materials versus ferrites in power electronics," *The 6th International Conference on Mining Science & Technology*.

[28] Z. Hamouda, S. Saib, S. Berghuel, "Dielectric properties of fe-co ferrite nanocrystalline material characterization in microwave region," *2017 5th International Conference on Electrical Engineering - Boumerdes (ICEE-B),* December 2017.

[29] Marek S. Rylko *Magnetic materials and soft-switched topologies for high-current DC-DC converters*, Ph.D. dissertation, University Collage Cork , Cork, Ireland, 2011

[30] Robert W. Erickson, *Fundamentals of Power Electronics*, Kluwer Academic Publischers, 2000.

[31] Colonel Wm. T. McLyman, *Transformer and Inductor Design Handbook,* 2nd ed., Marcel Dekker, Inc. 1988.

[32] M. Kacki, M.S. Rylko, J.G. Hayes, C.R. Sullivan, "Magnetic Material Selection for EMI Filters," *IEEE Energy Conversion Congress and Exposition (ECCE),* Cincinnati, OH, October 2017.

[33] D.J. Griffiths, *Instruction to Electrodynamics*, Prince Hall, 1999.

[34] E.C. Snelling, *Soft ferrites: properties and applications*, Newnes-Butterworth; 1st Edition, 1969.

[35] J. Xu, M.Y. Koledintseva, Y. Zhang, Y. He, B. Matlin, R.E. DuBroff, "Complex permittivity and permeability measurements and finite-difference time-domain simulation of ferrite materials," *IEEE Transactions on Electromagnetic Compatibility*, vol. 52, pp. 878-887, no.4, November 2010.

[36] V. Radonic, N. Blaz, L.J. Živanov, "Measurements of complex permeability using short coaxial line reflection method," Acta Physica Polonica Series A 117(5):820-824, 2010.

[37] www.waynekerrtest.com. Accessed on 15.01.2022.

[38] H. Jalili, B. Aslibeiki, A. Verzanech, V. Chernenko, "The effect of magneto-crystalline anisotropy on the properties of hard and soft magnetic ferrite nanoparticles, " *BEILSTEIN Journal of Nanotechnology*, 1348-1359, February 2019.

[39] O.V. Tereshchenko, F.J.K. Buesink, F.B.J. Leferink, “An overview of the techniques for measuring the dielectric properties of materials.” *XXXth URSI General Assembly and Scientific Symposium*, Istanbul, Turkey, August 2011.

[40] L. Brunetti, L. Oberto, M. Sellone, “Material Measurements with Vector Network Analysers” *Conference on Precision Electromagnetic Measurements (CPEM 2016)*, Ottawa, Canada, July 2016.

[41] M. Kącki, M.S. Ryłko, J.G Hayes, C.R. Sullivan, “A practical method to define high frequency electrical properties of MnZn ferrites,” *IEEE Applied Power Electronics Conference and Exposition (APEC)*, New Orleans, USA, March. 2020.

[42] M. Kacki, M. Rylko, E. Herbert, “PSMA-SMA Special Project – Phase II, Investigation on Magnetic Flux Propagation in Ferrite Cores“, *The Power Source Manufacturers Association Technical Report*, 2020.

[43] T. Todorova, V. Valchev, A. Van den Brosche, “Modelling of electrical properties of Mn-Zn ferrites taking into account the frequency of the occurrence of the dimensional resonance,” *Journal of Electrical Engineering*, vol. 52, pp. 219-225, July 2019.

[44] William H. Hayat, Jr, *Engineering electromagnetics*, New York: McGraw-Hill Book Co. 1981.

[45] www.abc.chemistry.bsu.by/vi/analyser. Accessed on 15.01.2022.

[46] T. Kauder, K. Hameyer, “Performance factor comparison of nanocrystalline, amorphous, and crystalline soft magnetic materials for medium-frequency applications,” *IEEE Transaction on Magnetics*, vol. 53, issue 11, Nov. 2017.

[47] M. Mu, *High Frequency Magnetic Core Loss Study*, Ph.D. dissertation, Virginia Polytechnic Institute, Blacksburg, Virginia, 2013.

[48] www.tek.com. Accessed on 15.01.2022.

[49] J. Muhlethaler, J. Biela, J. W. Kolar, A. Ecklebe, “Improved core loss calculation for Magnetic Components Employed in Power Electronics System,*” IEEE Transactions on Power Electronics*, vol. 27, issue 2, Feb. 2012.

[50] B. Carsten, “Why the magnetics designer should measure core loss, with a survey of loss measurements techniques and low cost, high accuracy alternative,” *Proceedings of PCIM Europe 1995; International Exhibition and Conference for Power Electronics, Intelligent Motion, Renewable Energy and Energy Management*, May *1995.*

[51] www.mathowrks.com. Accessed on 15.01.2022.

[52] www.epc-co.com/epc. Accessed on 02.06.2021.

[53] C. R. Sullivan, J. H. Harris, “Testing core loss for rectangular waveforms phase II final report,“ *The Power Source Manufacturers Association Technical Report*, September 2011.

[54] E. Herbert, “Generic specification for ferrite cores,” *The Power Source Manufacturers Association Technical Report*, March 2018.

[55] F. G. Brokaman, P. H. Dowling, W. G. Steneck, “Dimensional Effects Resulting from a High Dielectric Constant Found in a Ferromagnetic Ferrite,” *Physic Review*, vol. 77, January 1950.

[56] F. de Leon, A. Semlyen, “Time domain modelling of eddy current effects for transformer transients,” *IEEE Transactions on Power Delivery*, vol. 8, issue 1, pp. 271–280, Jul. 1993.

[57] Ch. Zhao, J. Ruan, Z. Du, S. Liu, Y. Yu, Y. Zhang, “Calculation of parameters in transformer winding based on the model of multi-conductor transmission line,” *International Conference on Electrical Machines and System*, Wuhan, Oct. 2008.

[58] S.M.H. Hosseini, P.R. Baravati, “New high frequency multi-conductor transmission line detailed model of transformer winding for PD study,” *IEEE Transactions on Dielectrics and Electrical Insulation*, vol. 24, issue 1, pp. 316–323, Feb. 2017.

[59] H.D. Gersem, A. Muetze, “Finite-element supported transmission-line models for calculating high-frequency effects in machine windings,” *IEEE Transactions on Magnetics*, vol. 48, issue 2, pp. 787–790, Feb. 2012.

[60] O. Magdun, A. Binder, A. Rocks, O. Henze, “Prediction of common mode ground current in motors of inverter-based drive systems,” *International Aegean Conference on Electrical Machines and Power Electronics*, Bodrum, Turkey, May 2007.

[61] C.R. Sullivan, “Lumped model to explain and approximate dimensional effects in ferrite cores,” *PSMA Workshop during IEEE Applied Power Electronics Conference*, Anaheim, USA, March 2019.

[62] www.ansys.com. Accessed on 02.06.2021.

[63] M. Kacki, M. Rylko, E. Herbert, “PSMA-SMA Special Project – Phase I, Investigation on Magnetic Flux Propagation in Ferrite Cores“, *The Power Source Manufacturers Association Technical Report*, 2018.

[64] www.agilent.com. Accessed on 06.02.2021.

[65] A. Bermudez, D. Gomez, P. Salgado “ Eddy-current losses study in laminated cores and computation of an equivalent conductivity,” *IEEE Transactions on Magnetics*, vol. 44, no. 12, pp. 4730–4738, December 2008.

[66] K. Howard, M.K. Kazimierczuk " Eddy-current power loss in laminated cores," *IEEE International Symposium an Circuits and Systems*, vol. 2, pp. 668–671, May 2001.

[67] Colonel Wm. T. McLyman, "*Magnetic Core Selection for Transformers and Inductors: A User's Guide to Practice and Specifications, Second Edition," CRC Press*, 2019.

[68] J. Zhu, K.J. Tseng, C.F. Foo " Effects on multi-segment structure on core losses in MnZn ferrites at high frequencies," *IEEE Transactions on Magnetics*, vol. 36, no. 8, pp. 3408–3410, September 2000.

[69] M. Kacki, M. Rylko, "Core assembly having magnetic properties for an electrical device, and throttle comprising such a core assembly," patent application WO20200015962A1.

[70] Y. Sakaki, T. Matsuoka " Effect of surface layer on the magnetic characteristics of Mn-Zn ferrite," *IEEE Translation Journal on Magnetics in Japan*, vol. 1, no. 6, pp. 772–774, September 1985.

[71] www.kemet.com. Accessed on 10.03.2022.

[72] www.tdk-electronics.tdk.com. Accessed on 10.03.2022.

APPENDIX A – COMPLEX PERMEABILITY CHARACTERISTIC

Measured ferrite complex permeability data for tested materials are presented in Table A.1

TABLE A.1. REAL AND IMAGINARY PERMEABILITY CHARACTERISTIC.

	Ferroxcube 3E10		Ferroxcube 3F36	
Frequency (MHz)	μ'	μ''	μ'	μ''
0.01	9812	228	1482	8
0.1	10215	621	1479	11.2
0.2	10150	2020	1478	9.8
0.3	9542	3230	1480	10.3
0.4	8529	4032	1483	10.5
0.5	7475	4375	1488	13.1
0.6	6659	4418	1499	13.7
0.7	6024	4349	1509	16.7
0.8	5549	4251	1522	20.4
0.9	5207	4156	1537	25.6
1.0	4806	4025	1561	38.2
2.5	2532	3264	1561	503
5.0	1060	2400	1078	763
7.5	524	1776	785	728
10.0	297	1315	606	650
12.5	222	1052	513	593
15.0	173	831	445	545
17.5	161	716	392	508
20.0	155	596	342	471
	Ferroxcube 3E65		Ferroxcube 3C95	
Frequency (MHz)	μ'	μ''	μ'	μ''
0.01	5100	10.7	3085	2.3
0.1	5156	57.8	3095	4.5
0.2	5253	290	3124	15.1
0.3	5444	789	3181	32.6
0.4	5425	1339	3265	79.8
0.5	5166	1994	3355	179
0.6	4797	2420	3418	314
0.7	4392	2712	3452	469
0.8	4022	2897	3464	626
0.9	3638	3036	3449	816
1.0	3320	3121	3403	996
2.5	264	2449	1855	1630
5.0	153	932	1078	1388
7.5	141	546	677	1249
10.0	131	371	375	1069
12.5	127	270	215	911
15.0	120	213	102	742
17.5	115	180	57.3	620
20.0	109	147	24.5	528

APPENDIX B – COMPLEX PERMITTIVITY CHARACTERISTIC

Measured ferrite complex permittivity data for tested materials are presented in Table B.1.

TABLE B.1. REAL AND IMAGINARY PERMITTIVITY CHARACTERISTIC.

	Ferroxcube 3E10		Ferroxcube 3F36	
Frequency (MHz)	ε'	ε''	ε'	ε''
0.01	218962	3292135	61262	76243
0.1	85011	814288	36788	18587
0.2	81232	413498	32208	13651
0.3	77352	289593	29893	11600
0.4	74238	220139	28382	10426
0.5	71206	180479	27275	9645
0.6	68758	156171	26410	9080
0.7	66158	135719	25703	8646
0.8	64065	122039	25109	8299
0.9	62211	111676	24598	8013
1.0	60678	103988	24151	7773
2.5	44943	56722	20622	6134
5.0	33149	39108	18321	5250
7.5	27023	32489	17081	4842
10.0	22925	28670	16284	4576
12.5	19845	26035	15679	4384
15.0	17632	24247	15202	4236
17.5	15747	22909	15810	4116
20.0	14282	21537	14484	4018
	Ferroxcube 3E65		Ferroxcube 3C95	
Frequency (MHz)	ε'	ε''	ε'	ε''
0.01	90788	8162193	213662	373678
0.1	85011	829638	123674	64461
0.2	81232	413498	111522	45085
0.3	77555	284607	105046	37712
0.4	74238	220139	100663	33702
0.5	71206	180479	97373	31130
0.6	68758	156171	94753	29312
0.7	66158	135719	92583	27943
0.8	64364	123885	90738	26867
0.9	62211	111676	89135	25991
1.0	60678	103988	87722	25261
2.5	44934	56722	76209	20441
5.0	33149	39108	68389	17928
7.5	27023	32489	64083	16694
10.0	22925	28670	61228	15931
12.5	20097	26247	59147	15362
15.0	17632	24237	57448	14918
17.5	15747	22909	56021	14556
20.0	14201	21253	54880	14257

APPENDIX C – CORE LOSS TESTER BOARD

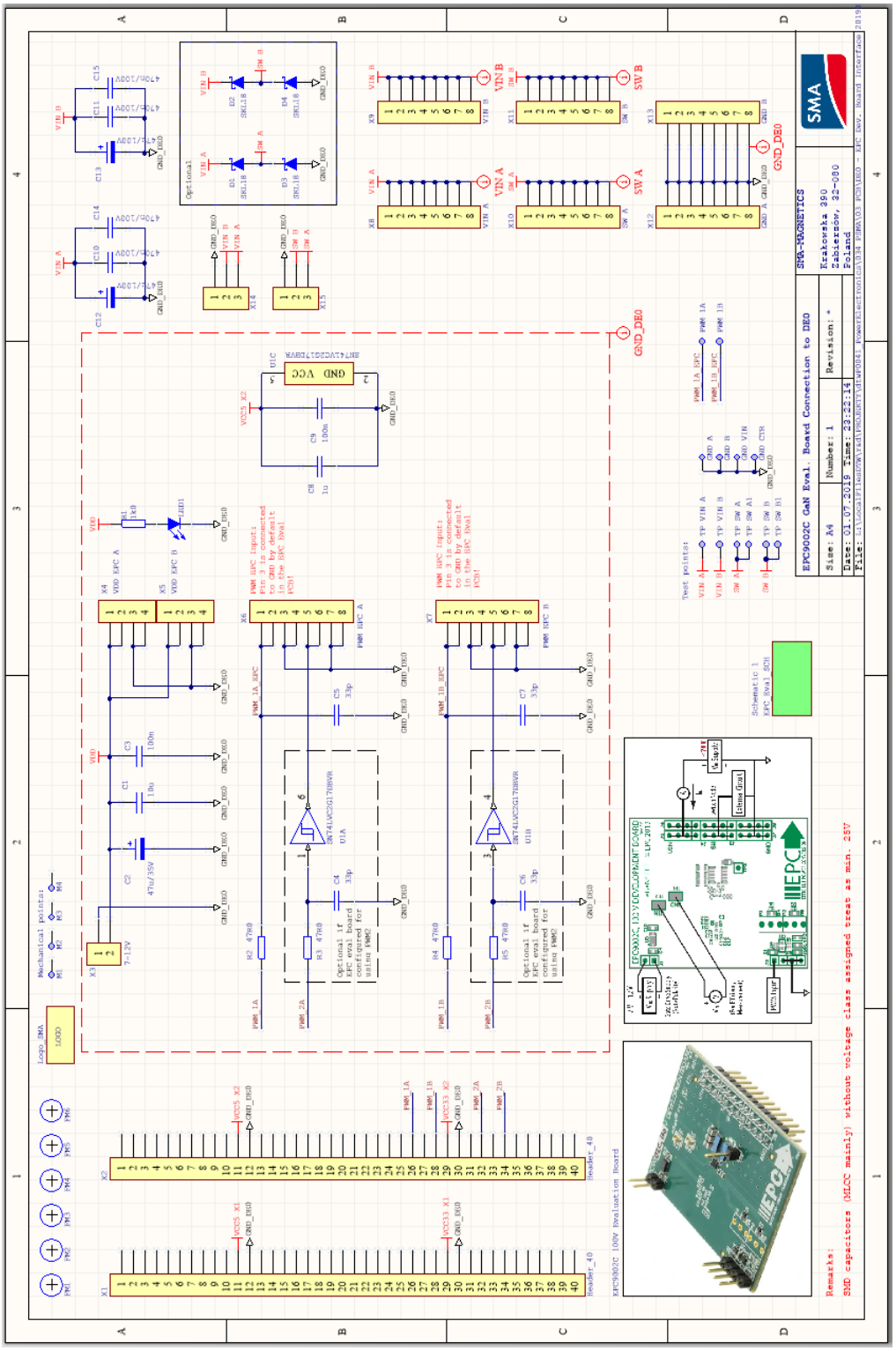
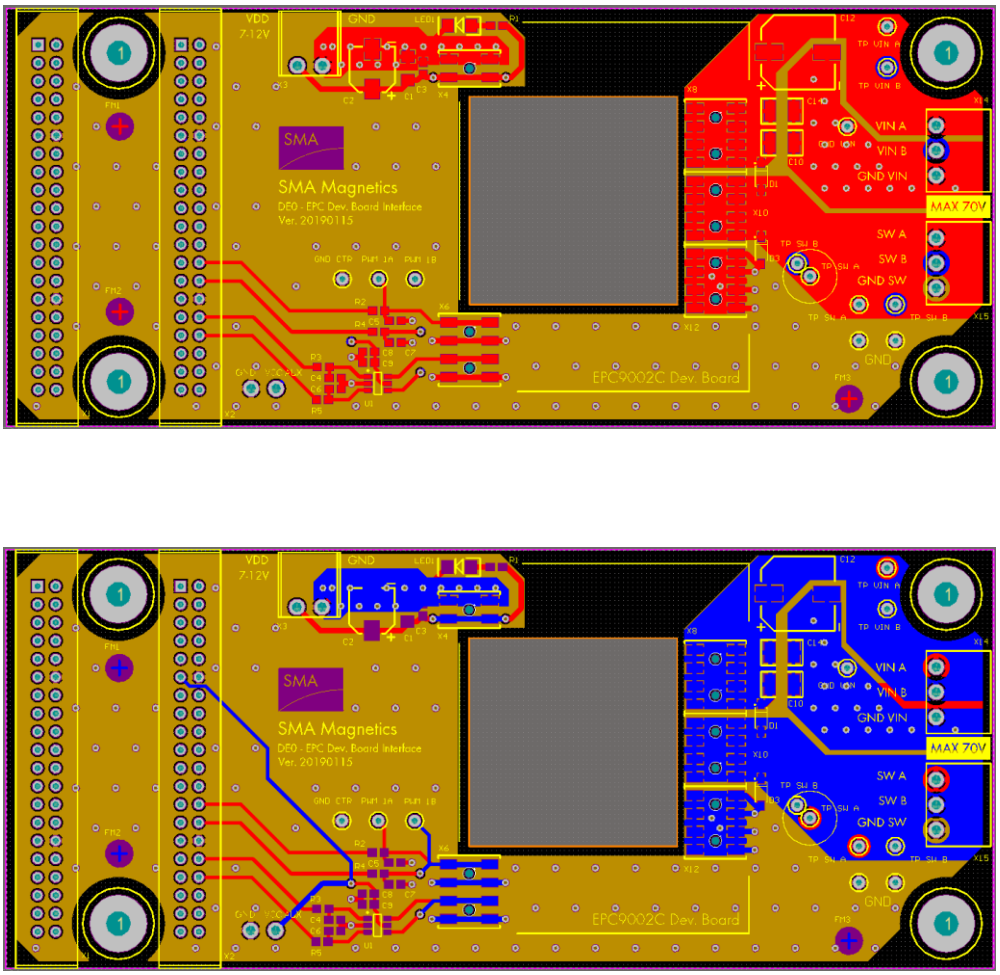


Figure C1. Main board connection schematic.



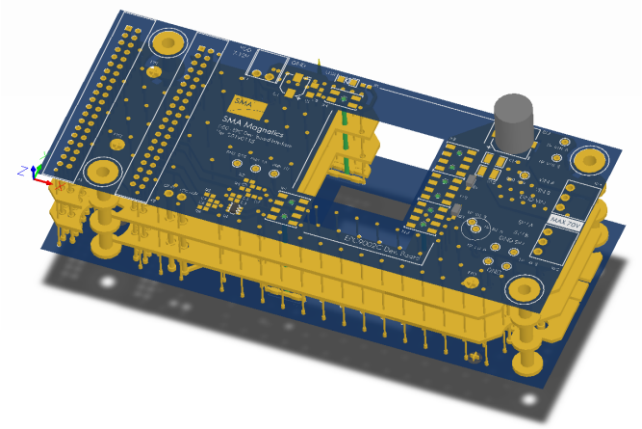


Figure C2. Main board PCB layout.

APPENDIX D – EMI FILTER PCB BOARD

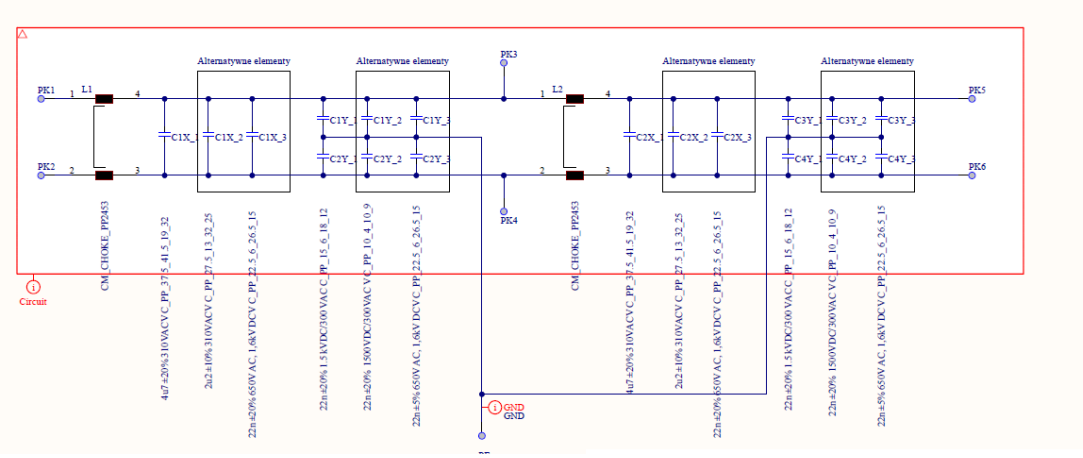


Figure D1. EMC filter test board connection schematic.

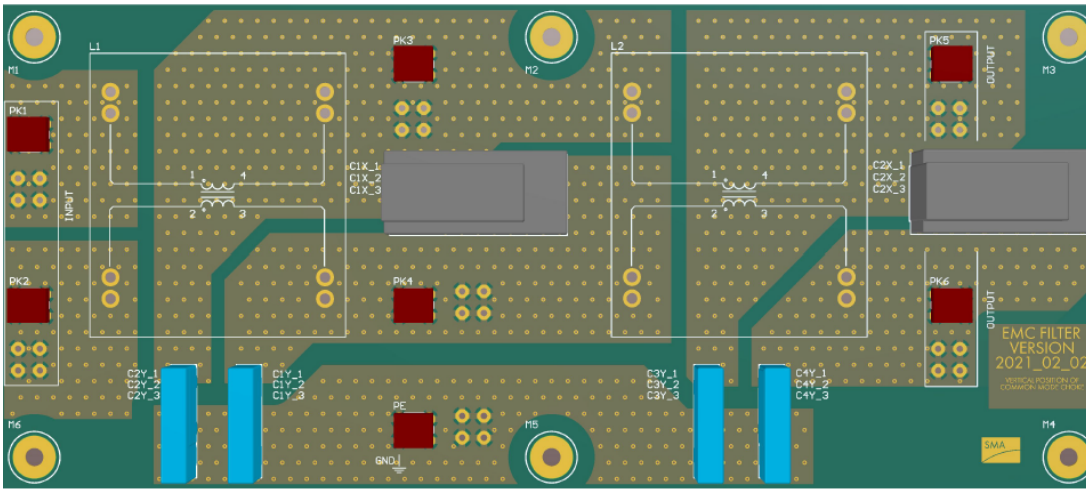


Figure D2. EMC filter test board PCB layout.